arXiv:astro-ph/0207371v3 4 Mar 2003

On The Determination of MDI High-Degree Mode Frequencies

S. G. Korzennik
Harvard-Smithsonian Center for Astrophysics, Cambridge, MA 02138, USA

M. C. Rabello-Soares
Hansen Experimental Physics Laboratory, Stanford University, Stanford, CA 94305, USA
and

J. Schou
Hansen Experimental Physics Laboratory, Stanford University, Stanford, CA 94305, USA

ABSTRACT

The characteristic of the solar acoustic spectrum is such that mode lifetimes get shorter and spatial leaks get closer in frequency as the degree of a mode increases for a given order. A direct consequence of this property is that individual p-modes are only resolved at low and intermediate degrees, and that at high degrees, individual modes blend into ridges. Once modes have blended into ridges, the power distribution of the ridge defines the ridge central frequency and it will mask the true underlying mode frequency. An accurate model of the amplitude of the peaks that contribute to the ridge power distribution is needed to recover the underlying mode frequency from fitting the ridge.

We present the results of fitting high degree power ridges (up to $\ell = 900$) computed from several two to three-month-long time-series of full-disk observations taken with the Michelson Doppler Imager (MDI) on-board the Solar and Heliospheric Observatory between 1996 and 1999.

We also present a detailed discussion of the modeling of the ridge power distribution, and the contribution of the various observational and instrumental effects on the spatial leakage, in the context of the MDI instrument. We have constructed a physically motivated model (rather than some *ad hoc* correction scheme) resulting in a methodology that can produce an unbiased determination of high-degree modes, once the instrumental characteristics are well understood.

Finally, we present changes in high degree mode parameters with epoch and thus solar activity level and discuss their significance.

Subject headings: Sun: oscillations

1. Introduction

Since from a single vantage point we can only observe a bit less than half of the solar surface, helioseismic power spectra computed for a specific target mode with degree ℓ and azimuthal order m also contains power from modes with different – and usually nearby – ℓ and m values. The presence of these unwanted modes, or spatial leaks, complicates the fitting of the resulting observed spectra and degrade the mode parameter estimates, especially when the leaks have frequencies similar to that of the target mode. As mode lifetimes get shorter and spatial leaks get closer in frequency (*i.e.*, $d\nu/d\ell$ becomes small), individual p-modes can no longer be resolved. This mode blending occurs around $\ell = 150$ for p-modes with frequency near 3.3 mHz and around $\ell = 250$ for the f-modes. Once individual modes blend into ridges, as illustrated in Figure 1, the power distribution of the

ridge masks the true underlying mode frequency and the ridge central frequency is not a good estimate of the target mode frequency. Moreover the amplitudes of the spatial leaks have been shown to be asymmetric (see for example Korzennik 1999). A direct consequence of this leakage asymmetry is to offset the power distribution of the ridges. Such offset results in a significant difference between the central frequency of the ridge and the frequency of the targeted individual mode. To recover the underlying mode frequency from fitting the ridge, an accurate model of the amplitude of the peaks that contribute to the ridge power distribution (*i.e.*, the leakage matrix) is needed.

The lack of unbiased determinations of mode frequencies and frequency splittings at high degrees has so far limited the use of such high-degree data in helioseismic inversions for constraining the near-surface structure and dynamics of the sun. Since experiments like the Michelson Doppler Imager (MDI) on board the Solar and Heliospheric Observatory (SOHO), with a two-arcsec-per-pixel spatial resolution in full-disk mode, allows us to detect oscillation modes up to $\ell \approx 1500$ (Scherrer et al. 1995), only a small fraction of the observed modes are currently used.

High-degree modes are trapped near the solar surface: for example, the lower turning point of a mode of degree $\ell = 500$ and frequency around 3 mHz is at 0.99 of the solar radius. This makes them exceptional diagnostic tools to probe the near-surface region of the Sun, a region of great interest. Indeed, it is there that the effects of the equation of state are felt most strongly, and that dynamical effects of convection and processes that excite and damp the solar oscillations are predominantly concentrated. Rabello-Soares et al. (2000) have shown that the inclusion of high-degree modes (*i.e.*, ℓ up to 1000) has the potential to improve dramatically the inference of the sound speed in the outermost 2 to 3% of the solar radius. Furthermore, inversion of artificial mode frequency differences resulting from models computed with two different equations of state (*i.e.*, MHD and OPAL) recovered the intrinsic difference in Γ_1, the adiabatic exponent, throughout the second helium ionization zone and well into the first helium and hydrogen ionization zones, with error bars far smaller than the differences resulting from using two different equations of state. These tests were carried out using the relatively large observational uncertainties resulting from ridge fitting, but with the implicit assumption that systematic errors were not present. These tests show that we can probe subtle effects in the thermodynamic properties of this region, but only when including such high-degree modes.

The first estimates of high-degree mode frequencies used m-averaged Big Bear Solar Observatory data (Libbrecht & Kaufman 1988). To recover the underlying mode frequency from fitting a given (n, ℓ) ridge, they used a simple Gaussian profile as an approximation for the m-averaged leakage matrix. Namely:

$$C_r^2(\ell, \ell') = \exp(-(\frac{\Delta\ell - \epsilon\,\ell}{2s})^2) \qquad (1)$$

where $\Delta\ell = \ell' - \ell$ while the $\epsilon\,\ell$ term represents the leakage asymmetry introduced by an image scale error of a fraction ϵ of the image size. The ridge centroid frequency was estimated using a simple weighted average:

$$\tilde{\nu}_{n,\ell} = \frac{\sum_{\ell'} C_r^2(\ell, \ell')\, A_{n,\ell'}\, \nu_{n,\ell'}}{\sum_{\ell'} C_r^2(\ell, \ell')\, A_{n,\ell'}} \qquad (2)$$

where $A_{n,\ell'}$ is the individual mode power amplitude and $\nu_{n,\ell'}$ is the mode frequency. The frequency difference between the ridge and the mode frequency, $\Delta\nu_{n,\ell} = \tilde{\nu}_{n,\ell}(\text{ridge}) - \nu_{n,\ell}(\text{mode})$, can thus be estimated using a parametric representation of the leakage coefficients.

For intermediate degree modes ($50 < \ell < 150$) this frequency difference can be directly measured by reducing the frequency resolution of the observed power spectra as to force individual modes to blend into ridges. Using observed $\Delta\nu$, the parameters s and ϵ can be calibrated at these intermediate degrees and the correction extrapolated to high-degree modes.

As Libbrecht & Kaufman (1988) state in their paper, this is only a first step and there is substantial room for improvement particularly at high ℓ. Following the same idea, but improving on the method, Korzennik (1990) and Rhodes et al. (1999) estimated high-degree mode frequencies using Mount Wilson and MDI data respectively. In contrast, Bachmann et al. (1995), using data from the High-L Helioseismometer at Kitt Peak, calculated the m-averaged leakage matrix, but neglect-

ing the horizontal components, in order to estimate high-degree mode frequencies.

In this paper, we present the results of an extensive study of the various elements that contribute to the precise value of the effective leakage matrix, that in turn is key to the precise determination of high degree modes. We have attempted to construct a physically motivated model — rather than an *ad hoc* correction scheme — in order to produce an unbiased determination of the high-degree modes. Since Korzennik (1999) has shown that the inclusion of the horizontal component of the leakage matrix calculation partially explains its observed asymmetry, we have included the horizontal component in all our leakage matrix calculations.

In Section 2, we describe the data we used and how we computed and fitted the power spectra used in this work. In Section 3 we present and discuss ridge modeling for high degree modes while in Section 4 we address the issue of estimating the ratio between the radial and horizontal components. In Section 5 we discuss the instrumental effects specific to MDI that must be included to properly model the ridge power distribution. Finally, in Section 6, we present the results of our analysis followed by our conclusions.

2. Data Used and Fitting Methodologies

The data used in this work consists of four separate time series of full-disk Dopplergrams. These Dopplergrams were obtained by the MDI instrument while operating in its full disk $2''$ per pixel resolution mode and during the *Dynamics Program*. The instrument is operated in this mode some 3 months every year, when the available telemetry bandwidth is large enough to bring down full-disk images. Table 1 lists the starting time and duration of each of the four *Dynamics* data time series.

The spherical harmonics decomposition up to $\ell = 1000$ was carried out by the MDI Science Team (Schou 1999). For the same periods, mode frequencies and rotational splitting coefficients of individual p-modes were computed for low and intermediate degrees as part of the *Structure Program* (Schou 1999).

For each *Dynamics Program* period we computed and fitted power spectra using two distinct approaches. The purpose of the first one was to get some observational estimate of the leakage matrix asymmetry, using an optimum estimate of the sectoral limit spectra computed with a high frequency resolution where individual p-modes can be clearly resolved.

We used only sectoral spectra because the leakage matrix for the sectoral modes is diagonal at a fixed radial order, n (namely non-zero only when $\delta m = \delta\ell$), resulting in a simple leakage pattern, with modes separated by at least the quantity $\partial\nu/\partial\ell$. For zonal and tesseral modes the leakage pattern is more complex resulting in leaks very close to each other, some separated only by even multiples of $\partial\nu/\partial m$. For these modes, only for very low frequencies (where the lifetime is long enough), and if the time series is long enough, can the main peak be resolved from its closest spatial leaks.

The second approach is aimed at computing optimum power spectra for high-degree modes ridge fitting. Namely spectra with a lower frequency resolution — since individual modes are not resolved – while in the process averaging out the realization noise that a high frequency resolution spectrum would reveal. Moreover, at low and intermediate degrees individual modes blend into ridges as a result of the low frequency resolution. This approach creates an overlap between mode fitting and ridge fitting where the frequency offset introduced by ridge fitting can be directly measured. By using this overlap, we can check the model we have developed to infer mode parameters from the fitted ridge parameters.

2.1. Limit Spectra for Resolved Modes at Intermediate Degrees

Estimates of limit spectra were computed for intermediate degree sectoral modes, when individual modes could be resolved, using the following procedure. First, each time series of spherical harmonic coefficients was detrended using a 21-minute-long running mean. Then, the 9th order sine multi-tapered power spectrum was computed, using the two- to three-month-long time series and thus corresponding to a frequency resolution between 0.18 μHz and 0.24 μHz. Finally, for a range of degrees (15 consecutive ℓ) at a fixed order, n, small fractions of power spectra (about 300 μHz), centered around each mode frequency, were aver-

TABLE 1
Dynamics Program EPOCHS

Data Set [year]	Starting Date month/day	Duration [days]
1996	05/23	63
1997	04/14	93
1998	01/09	92
1999	03/13	77

aged. The sectoral mode frequencies were computed using a table of frequencies and frequency splittings resulting from mode fitting of MDI data.

A seven-component profile was fitted in the least-squares sense to these limit spectra using the following parameterization:

$$P_{n,\ell}(\nu) = \sum_{\ell'=\ell-3}^{\ell+3} \left(A_{n,\ell'} \, \frac{1+\alpha_{n,\ell}(x-\alpha_{n,\ell}/2)}{1+x^2} \right) + b_{n,\ell} + s_{n,\ell}\,(\nu-\nu_{n,\ell}) \quad (3)$$

where

$$x = x_{n,\ell,\ell'}(\nu) = \frac{\nu-\nu_{n,\ell'}}{\gamma_{n,\ell}} \quad (4)$$

and where $A_{n,\ell'}$ and $\nu_{n,\ell'}$ are the individual mode amplitude and frequency respectively; $\gamma_{n,\ell}$ and $\alpha_{n,\ell}$ are the mode width and asymmetry parameter respectively – assumed constant for all seven components; and $b_{n,\ell}$ and $s_{n,\ell}$ represent the background power.

Note that the shape of the profiles used in this formulation is equivalent to the one defined by Equation 4 of Nigam & Kosovichev (1998). After some rudimentary algebra, one can identify their asymmetry coefficient, B, to the one we use, α, namely $\frac{\alpha}{2} = B\,(1-\frac{\alpha^2}{2})$.

2.2. Power Spectra at High Degrees and Ridge Fitting

For each period listed in Table 1, the time series of spherical harmonic coefficients were subdivided in 4096-minute-long intervals. For each spherical harmonic degree, ℓ, and each azimuthal order, m, each interval was first detrended using a 17-minute-long running mean, and then Fourier transformed with an oversampling of 2 to estimate the power spectrum. The power spectra corresponding to each 4096-minute-long interval in a given period were then averaged together to produce high signal-to-noise ratio spectra with a frequency resolution of 4.1 μHz. As a result of this low frequency resolution, the individual modes down to $\ell \approx 100$ blended into ridges, while the ridge width itself is still very much oversampled.

The following asymmetric profile plus a background term was fitted in the least squares sense to each low frequency resolution spectrum, for $100 \le \ell \le 900$:

$$P_{\ell,m}(\nu) = \sum_{n} \left(\tilde{A}_{n,\ell,m} \, \frac{1+\tilde{\alpha}_{n,\ell,m}(\tilde{x}_{n,\ell,m}-\tilde{\alpha}_{n,\ell,m}/2)}{1+\tilde{x}^2_{n,\ell,m}} \right) + B_{\ell,m}(\nu) \quad (5)$$

where

$$\tilde{x}_{n,\ell,m} = \frac{\nu-\tilde{\nu}_{n,\ell,m}}{\tilde{\gamma}_{n,\ell,m}} \quad (6)$$

and

$$\log\, B_{\ell,m}(\nu) = \sum_{j=0}^{2} b_j(\ell,m)\,\nu^j \quad (7)$$

such parameterization of the background power is better suited for the fit performed here, namely over a broad frequency range.

In this case, $\tilde{A}_{n,\ell,m}$, $\tilde{\gamma}_{n,\ell,m}$, $\tilde{\nu}_{n,\ell,m}$ and $\tilde{\alpha}_{n,\ell,m}$ are the *ridge* amplitude, width, frequency and asymmetry parameters for a given (n,ℓ,m) ridge fitting. For practical reasons, this fitting was carried out only every 5th ℓ for $100 \le \ell \le 250$ and every 10th ℓ for $250 < \ell \le 900$, and only for some 50 equally spaced m values at each ℓ. From the resulting *ridge* frequencies, the *ridge* frequency

splittings were parameterized in terms of Clebsh-Gordon coefficients ($\tilde{a}_i$, for $i = 1, 6$, see Ritzwoller & Lavely 1991).

A single asymmetric function was used to to fit each ridge power density profile (Eq. 5). Since the ridge power density profile results from the overlap of the target mode and the spatial leaks, it is mathematically not a similar single asymmetric function. In the specific case of high degree modes and at the frequency resolution we have used we believe that our approach is both justified and practical, based on the following considerations. First, the profile resulting from the overlap of nearby profiles is reasonably well modeled by a single profile when the ratio of the width of the individual profiles ($\Gamma_{\rm eff}$) to the separation ($\partial\nu/\partial\ell$) become large. Indeed, for a ratio of 2 – a ratio that roughly corresponds to the mean ratio around $\ell = 300$ – the root-mean-squares (RMS) of the difference between a superposition of profiles and a single profile is only 4% (when normalizing the resulting fitted profile maximum to unity). For a ratio of 4 ($\ell \approx 500$) the RMS of this difference drop to 2%, while for a ratio of 10 ($\ell \approx 700$) this RMS drop to 0.6%. These numbers are to be compared to the RMS of the residuals to the fit that are around 5 to 7% (when using the same normalization) at all degrees and are dominated by the realization noise. The second reason to use a single profile is practical: fitting to the resulting power density profile the sum of individual overlapping profiles is underconstrained, unless some assumptions on the separations and/or the relative amplitudes are made. Since neither of these quantities are known *a priory* with enough precision such approach is impractical.

3. Ridge Modeling

We describe here our physically motived ridge model, from which corrections to the ridge parameters are estimated. Once the offsets between ridge and mode parameters are determined, the observed ridge parameters can be corrected and the mode parameters for high-ℓ obtained, making it possible to study the near-surface region of the Sun.

3.1. Leakage Matrix: Radial and Horizontal Components

Since the spatial dependence of solar oscillations can be described in terms of spherical harmonics $Y_\ell^m(\theta, \phi)$ of co-latitude θ and longitude ϕ, the velocity signal resulting from these oscillations can be written as:

$$\vec{v}_{n,\ell,m} = (V_r\, Y_\ell^m,\ V_h\, \partial_\theta Y_\ell^m,\ V_h\, \frac{1}{\sin\theta}\, \partial_\phi Y_\ell^m). \quad (8)$$

and the leakage matrix components, resulting from the spherical harmonic decomposition of the observed line-of-sight velocity, are given by:

$$C^r_{\ell,m;\ell',m'} = \oint W Y_\ell^{m*} Y_{\ell'}^{m'} \sin\theta\cos\phi\, d\Omega \quad (9)$$

$$C^\theta_{\ell,m;\ell',m'} = -\frac{1}{L}\oint W Y_\ell^{m*} \partial_\theta Y_{\ell'}^{m'} \cos\theta\cos\phi\, d\Omega \quad (10)$$

$$C^\phi_{\ell,m;\ell',m'} = \frac{1}{L}\oint W Y_\ell^{m*} \partial_\phi Y_{\ell'}^{m'} \sin\phi\, d\Omega \quad (11)$$

where * represents the complex conjugate operator and $W(\theta, \phi)$ is the spatial window function of the observations – *i.e.*, a function that delimits the angular span of the observations and that includes additional spatial attenuations like spatial apodization.

The complete leakage matrix is the sum of the radial component C^r and the horizontal components $C^\theta + C^\phi$. Thus a mode with a given (ℓ', m') will leak in the (ℓ, m) power spectrum with an amplitude attenuated by a factor $C^2_{\ell,m;\ell',m'}$ where:

$$C_{\ell,m;\ell',m'} = C^r_{\ell,m;\ell',m'} + \beta_{n,\ell}\,(C^\theta_{\ell,m;\ell',m'} + C^\phi_{\ell,m;\ell',m'}), \quad (12)$$

and where $\beta_{n,\ell}$ is the horizontal-to-vertical displacement ratio. Using a simple outer boundary condition, *i.e.* that the Lagrangian pressure perturbation vanish ($\delta p = 0$), the small amplitude oscillations equations for the adiabatic and non-magnetic case lead to an estimate of the ratio β, given by (Christensen-Dalsgaard 1997):

$$\beta_{n,\ell} = \frac{G\, M_\odot\, L}{R_\odot^3\, \omega_{n,\ell}^2} = \frac{\nu_{0,\ell}^2}{\nu_{n,\ell}^2} \quad (13)$$

where G is the gravitational constant, $M_\odot$ is the solar mass, $R_\odot$ is the solar radius, ω is the cyclic frequency ($\omega = 2\pi\nu$) and $L^2 = \ell(\ell+1)$. It can be

reduced to the square of the ratio of the frequency of the fundamental ($n = 0$) for the given degree to the mode frequency, since the frequency of the fundamental is given by (Gough et al. 1980)

$$\nu_{0,\ell}^2 = \frac{G\, M_\odot\, L}{4\pi^2 R_\odot^3} \tag{14}$$

Since for a given ℓ, the f-mode frequency is smaller than any p-mode frequency, Equation 13 implies that $0 < \beta \leq 1$.

Estimates of β resulting from computing the adiabatic and non-magnetic eigenfunctions using a standard solar model (Christensen-Dalsgaard et al. 1996) at the appropriate atmospheric height for the MDI instrument and using a different upper boundary condition than the one leading to Equation 13 gives a very similar result. These calculations produce values that, above 2 mHz, decrease with frequency slightly faster than predicted by Equation 13 (*i.e.*, 15% smaller at 3 mHz). However, the non-adiabatic nature of the oscillations in the solar atmosphere are not taken into account in these calculations nor is it taken into account in the derivation of Equation 13. Since the solar interior is non-adiabatic near the surface and since the effect of the magnetic field, if any, is likely to be mostly near the surface, the *real* value of β might be somewhat different.

The estimate of the coefficients of the leakage matrix given by equations 9 to 11 is a useful guide but remains oversimplified. Indeed, these equations do not take into account the pixel size of the detector or the instrumental modulation transfer function (MTF), effects that are substantial at high degrees. Therefore, rather than integrating these equations, we opted to compute the leakage matrix coefficients by constructing simulated images corresponding to the line-of-sight contribution of each component of a single spherical harmonic mode and decompose that image into spherical harmonic coefficients using the numerical decomposition used to process the observations. Such an approach allows us to easily include effects like the finite pixel size of the detector as well as other instrumental effects like the instrumental MTF, a plate scale error or some image distortion.

Since this calculation is computationally expensive and since the leakage coefficients vary smoothly with ℓ and m, it was carried out only for a subset of modes, from which all the required values were interpolated.

Figure 2 shows some typical examples of observed and synthetic spectra where the amplitude of the leaks corresponds to leakage matrices calculated with and without including the horizontal component (right and left panels respectively). This figure clearly shows not only that the observed amplitudes of the spatial leaks are asymmetric, but the importance of the contribution of the horizontal component in the leakage matrix calculation, since the radial component of the leakage matrix is nearly symmetric. It should also be noticed that, although the complete leakage matrix agrees in broad terms with the observed spectra, it does not agree in detail, as already pointed out by Korzennik (1999). This was the motivation for the work we present here, where we discuss in details how to best compute the correct *effective* leakage matrix, *i.e.* the one resulting from the *actual* data analysis.

3.2. Perturbation of the Leakage Matrix by the Solar Differential Rotation

Woodard (1989) has computed the distortion of the eigenfunctions by a slow, axisymmetric differential rotation. He showed that the distorted eigenfunctions can be expressed as a superposition of the undistorted ones. Under the assumption of axial symmetry, each of the superposed functions has the same azimuthal order m, while symmetry with respect to the solar equatorial plane implies that the values of the spherical harmonic degree included in the superposition be either all odd or even. The Coriolis acceleration is also assumed to be small which is valid for high-degree p-modes ($\ell > 100$). This additional simplification reduces the perturbed eigenfunctions to be approximately a superposition of unperturbed eigenfunctions of the same radial order n.

Also, the rotation rate Ω for high degree modes ($\ell > 100$ corresponds roughly to the radius range $0.9R_\odot < r < R_\odot$) is primarily a function of latitude, and can be parameterized as:

$$\Omega(\theta) = 2\pi(B_0 + B_2 \cos^2\theta + B_4 \cos^4\theta) \tag{15}$$

where $B_0 = 473$ nHz, $B_2 = -77$ nHz and $B_4 = -57$ nHz (Snodgrass & Ulrich 1990), and θ represents the co-latitude.

The perturbed leakage matrix can be expanded in terms of the unperturbed one as:

$$\tilde{C}_{\ell,m;\ell',m'} = \sum_{\ell''} G_{\ell',\ell''}\, C_{\ell,m;\ell'',m'} \qquad (16)$$

where:

$$G_{\ell',\ell''} = \frac{(-1)^p}{2\pi} \int_{-\pi}^{\pi} \cos\left[p\theta + \delta\Phi(\theta)\right]\, d\theta \qquad (17)$$

$$\begin{aligned} \delta\Phi(\theta) &= \frac{1}{2}\frac{m}{\partial\nu/\partial\ell}\left[\frac{1}{2}(B_2\, y_{\ell'}^2 + B_4\, y_{\ell'}^4)\sin\theta\right. \\ &\quad \left. -\frac{1}{16}B_4\, y_{\ell'}^4 \sin(2\theta)\right] \end{aligned} \qquad (18)$$

and where $G_{\ell',\ell''}$ is zero unless $\ell' - \ell''$ is even, $2p = \ell' - \ell''$, $y_\ell^2 = 1 - (m/L)^2$.

This distortion is illustrated in Figures 3 and 4, where we show the variation of $G_{\ell',\ell''}$ with respect to m and $\ell - \ell'$ for selected values of ℓ, and a synthetic spectrum with and without distortion by differential rotation for $\ell = 500$. We should also add that Woodard (2000) has shown that including meridional circulation affects these calculations at the 10% level.

3.3. Theoretical Ridge Parameters

Synthetic power spectra were computed by overlapping individual modes as they leak in the simulated spectrum according to:

$$\begin{aligned} \hat{P}_{n,\ell,m}(\nu) &= \sum_{\ell'=\ell-3}^{\ell+3} \sum_{m'=m-3}^{m+3} \tilde{C}^2_{\ell,m;\ell',m'}(\beta_{n,\ell}) \times \\ &\quad \frac{1 + \hat{\alpha}_{n,\ell}(\hat{x}_{n,\ell',m'} - \hat{\alpha}_{n,\ell}/2)}{1 + \hat{x}^2_{n,\ell',m'}} \end{aligned} \qquad (19)$$

$$\hat{x}_{n,\ell',m'} = \frac{\nu - \hat{\nu}_{n,\ell',m'}}{\hat{\gamma}_{n,\ell}} \qquad (20)$$

where $\hat{\nu}$, $\hat{\gamma}$ and $\hat{\alpha}$ are the mode frequency, width and asymmetry parameter used to generate the model. We used for ($\hat{\nu}$, $\hat{\gamma}$, $\hat{\alpha}$) values based on observed parameters and used Equation 13 for the values of β. We generated these synthetic spectra for values of ℓ between 100 and 900 – but only every 5th ℓ up to 250 and every 10th ℓ above 250, replicating the sampling we used in the fitting of the observed MDI spectra as described in Section 2.2.

We generated two sets of synthetic power spectra, one where we did not include the effect of the distortion of the eigenfunction due the differential rotation (*i.e.*, $G_{\ell',\ell''} = \delta_{\ell',\ell''}$), while the other did include this effect. We then used on these two sets of simulated ridges the same fitting procedure we used on the actual observations, as described in Section 2.2 and Equation 5, to compute *ridge* frequencies and frequency splitting coefficients. If our model is correct and complete, our simulations should produce frequency and splitting coefficient offsets smilar to the one resulting from MDI observations.

Figure 5 illustrates, in an ℓ–ν diagram format, the region of overlap between mode fitting and ridge fitting. This range of frequencies and degrees is useful to valide our methodology but too restrictive to dare to carry out any extrapolation. In figures 6 to 8 we show frequency and splitting coefficient offsets from our two sets of simulations and the offsets from actual observations for intermediate-degree modes where there is an overlap between ridge and mode fitting. The theoretical differences agree overall with the observations (*i.e.*, magnitude and general trend), but not in detail. The effect of the distortion by the differential rotation is significant, and affects the most the odd splitting coefficients. It explains very well the discontinuity in the splittings coefficients seen as far back as in Korzennik (1990), and more recently in Rhodes et al. (1999).

3.4. Influence of the Rotation Profile on the Splitting Corrections

The latitudinal dependence of the solar rotation rate, $\Omega(\theta)$, must in principle be known to compute the perturbation of the leakage matrix by the differential rotation (see Section 3.2). Equations 17 and 18 result from an explicit parameterization of the near surface rotation with latitude given by Equation 15, and thus depend on the precise values adopted for B_2 and B_4. Therefore the correction for the ridge rotational splittings depends on a model of rotation, while the corrected splittings are meant to allow us to derive that rotation profile.

In order to estimate the effect of the rotation profile on the correction of the splittings, we have synthesized theoretical ridges using three different rotation profiles. Each set of ridges was then fit-

ted and ridge frequency splittings were computed, from which three sets of splitting coefficient corrections were computed.

The first model, hereafter model A, used a somewhat arbitrary rotation profile defined by $B_2 = -75$ and $B_4 = -50$ nHz, model B used a profile inferred by Schou et al. (1998) using the MDI medium-ℓ splitting coefficients, while model C used the profile given by Snodgrass & Ulrich (1990) based on the cross-correlation of Mt. Wilson magnetograms. The three profiles are compared in Figure 9. Relative variations with respect to model A are show in Table 2 and illustrated in Figure 10. The first column of Table 2 indicates the average relative change in the rotation profile, while the other columns show the average and RMS of the respective parameter relative corrections.

This table shows that the frequency correction is affected by the choice of the rotation profile, but at a relative level substantially smaller than the relative change in the rotation profile. We should also note that the relative change in the frequency correction is a function of degree, as it grows larger at larger degrees. Table 2 also shows that the correction in the a_i coefficients is affected by the choice of $\Omega(\theta)$ by a relative amount comparable to the relative change in the rotation profile. Again we should point out that the change shows a variation with degree and frequency. It is most pronounced for a_1 for the f-mode, but is also substantial for $n = 1$, while for a_3 only the f-modes show a substantial effect. Of course some of this is the direct result of the variation of $\Delta\Omega$ with latitude between the different models used. Finally we should point out that the solar rotational profile is known with a better precision than the numbers listed in Table 2 suggest, resulting in smaller effects.

4. Estimate of β from Intermediate Degree Observations

Korzennik (1999) presented a methodology to estimate β from intermediate degree observations and speculated, on the basis of a single season of *Dynamics* observations, that Equation 13 might not be satisfied. This methodology proceeds as follow: First, the leakage asymmetry is quantified using a single factor, S_x, defined by:

$$S_x(n,\ell) = \frac{\sum_{\ell'=\ell-3}^{\ell+3} (\ell'-\ell)\ A_{n,\ell'}}{\sum_{\ell'=\ell-3}^{\ell+3}\ A_{n,\ell'}} \qquad (21)$$

using the values of $A_{n,\ell'}$ fitted to the sectoral limit spectra as described in Section 2.1 and Equation 3. Next, a correspondence between S_x and β is established using the complete leakage matrix, namely:

$$S_x(\beta,\ell) = \frac{\sum_{\ell'=\ell-3}^{\ell+3} (\ell'-\ell)\ C^2_{\ell,\ell;\ell',\ell'}(\beta)}{\sum_{\ell'=\ell-3}^{\ell+3}\ C^2_{\ell,\ell;\ell',\ell'}(\beta)} \qquad (22)$$

Finally, using this correspondence (shown to be nearly independent of ℓ in Figure 4 of Korzennik 1999) the values of S_x are converted to observational estimates of β, hereafter refered as $\tilde{\beta}$.

Alternatively, one can estimate $\tilde{\beta}$ using a forward approach, where $\tilde{\beta}$ is adjusted as to produce theoretical ridge frequencies — by fitting synthetic spectra — that matches the observed ridge frequencies. Both methodologies agree, as shown in Figure 11, for a single year of *Dynamics* data.

When this method was applied to successive years, using the same leakage matrix, we found that $\tilde{\beta}$, while agreeing for 1996 and 1997, changed noticeably in 1998 and substantially in 1999. Since it is highly unlikely that β, the horizontal-to-vertical displacement ratio, would actually change over the years, we came to the obvious conclusion that observed discrepencies — whether expressed in term of leakage asymmetry or frequency or splittings differences — resulted from some missing component in our modeling.

Thus instead of trying to adjust the leakage matrix with some *ad hoc* estimate of $\tilde{\beta}$, one must improve the leakage matrix estimate using physically motivated contributions, as to produce an unbiased determination of the high-degree mode frequencies. In fact, we show in the next sections that the differences of $\tilde{\beta}$ between 1998 and 1999 results from a time variation of the plate scale error in the decomposition of the MDI images.

We should also point out that Schou & Bogart (1998) while investigating flow and horizontal displacements from ring diagrams, using MDI *Dynamics* observations, found the ratio β to be in good agreement with the theory (see Figure 7 of Schou & Bogart 1998). Schmidt, Stix, & Wöhl (1999) have argued that the observed velocity vectors in the photosphere appeared to be

Table 2: Relative variation of ridge to mode corrections with respect to the rotation profile.

	$\Delta\Omega$ [%]	$\Delta\nu$ [%]	Δa_1 [%]	Δa_3 [%]	Δa_5 [%]
Model B − A	-4.4	$+0.22 \pm 0.05$	-2.52 ± 0.10 [a]	$+1.28 \pm 0.09$ [b]	$+10.55 \pm 0.08$
Model C − A	$+6.2$	-1.65 ± 0.52	$+6.47 \pm 0.06$	$+7.16 \pm 0.06$	$+8.28 \pm 0.05$

[a] computed for $n > 1$ only
[b] computed for $n > 0$ only

more vertical than predicted, using MDI velocity power spectra to study the centre-to-limb variation. But Rhodes et al. (2001) concluded that the ratio β is very close to the theoretical value, by studying m-averaged intermediate degree GONG power spectra.

5. Instrumental Effects

The MDI instrument has been very stable over the years. Nonetheless, continuous exposure to solar radiation has increased the instrument front window absorption resulting in a long term increase in its temperature (Bush, Chu, & Kuhn 2001). Moreover, there is indirect evidence for a temperature gradient from the center to the edge of the front window, associated with that temperature increase. This gradient is believed to cause a small curvature that converts the front window into a weak lens.

Evidence of this is a drift in the instrument focus (see top panel of Figure 12). The short term small variation in the focus is correlated with the annual temperature change of the front window due to the satellite orbit around the Sun (see Bush, Chu, & Kuhn 2001, for further details).

Image focusing on the MDI instrument is controled by inserting (or not) blocks of glass of varying thickness into the light path (see Scherrer et al. 1995). There are 9 possible focus positions, with one focus step corresponding to approximately a third of a wave. Most of the time, the image was slightly defocused on purpose to match the detector resolution. The actual configuration in which the instrument was operating is shown in the top panel of Figure 12, with the corresponding amount of defocus.

A direct consequence of a change in focus is a variation of the image scale at the detector. The bottom panel of Figure 12 shows the variation of the ratio of the radius calculated using the initial plate scale relative to the mean image radius. The mean image radius is the instantaneous average of the image semi-major and semi-minor axis (see below), while the initial plate scale refers to a fixed estimate of the image radius computed in early 1996. The discontinuities are due to changes in the instrument focus position and are indicated by vertical dashed lines. The observed annual variations as well as the small but systematic increase with time are correlated with the aforementioned changes in the front window temperature.

Besides the image scale, another relevant aspect of the optical characteristics of the instrument is the distortion of the solar image. The shape of the solar limb on the detector can be approximated by an ellipse with an eccentricity 100 times larger than the actual eccentricity of the sun. The difference beween the semi-major and the semi-minor axis of the MDI full-disk image is 0.50 ± 0.04 pixels, while the mean radius is 488.45 pixels. The orientation is such that the semi-major axis forms an angle of $34^{\rm o} \pm 1^{\rm o}$ with the equator in the clockwise direction. Although the changes in the MDI focus affect the solar image ellipticity, these variations are rather small, resulting in a distorted but relatively stable image.

Let us point out that the spherical harmonic decomposition of all the *Dynamics* data has been carried out assuming a circular solar limb, with no image distortion. The image radius used for this decomposition was computed using the value corresponding to the *initial* estimate of the MDI instrument plate scale and rescaled according to the distance to the sun given by the spacecraft orbit ephemeris. The variations introduced by the change of focus position and the effect of the front window were not all known or well characterized

and thus were not taken into account at the time the spatial decomposition was computed. Since the computation of 500,000 coefficients for some 468,000 images – each 1024×1024 pixels – is a rather intensive computing task, the spatial decomposition has not yet been recomputed to take into account the known image scale variations.

5.1. Effects of Plate Scale Error

Variations of the mean image radius relative to the initial plate scale, even at the 10^{-3} level (as illustrated in the lower panel of Figure 12) will somewhat affect the amplitude of the spatial leaks (see Equation 1) and must be taken into account in the leakage matrix calculation.

In Figure 13 we compare the computed limit spectrum (see Section 2.1) estimated for $n = 2$ and $\ell = 103$ for 1998 and 1999, in the upper panel. It clearly shows that the leakage asymmetry changes sign between both epochs ($A_{\ell-1} < A_{\ell+1}$ in 1998, while $A_{\ell-1} > A_{\ell+1}$ in 1999). The lower panel of Figure 13 shows simulated power spectra computed using a leakage matrix with and without a plate scale error of -0.1%. As expected[1], the plate scale error causes a change in the leakage asymmetry similar to the change observed between 1998 and 1999 observations.

The plate scale errors for the different *Dynamics* epochs are given in Table 3. Note also that it is the size of the equatorial radius that will dictate the amplitude of the leaks for the sectoral spectra. Since the shape of the solar image on the detector is nearly an ellipse, the radius at the equator is slightly larger ($\approx .02\%$) than the mean radius.

The effect of the plate scale error can be clearly seen in the observed ridge frequency offsets presented in Figure 14. The offsets between ridge and mode frequencies for 1996 and 1997 are very similar, while for 1998 and especially for 1999 they become substantial. The values of Δa_1 (*i.e.*, the first *ridge* splitting coefficient offset) also show some variation from year to year, although smaller.

We have modeled the effect of a plate scale error by computing the leakage matrix resulting from decomposing images using the wrong radius, and including the effect of the distortion of the eigenfunction by the differential rotation. These leaks were then used to generate synthetic power ridges that were fitted using the same ridge fitting procedure described earlier. Figure 15 shows the frequency offsets and rotational splittings first coefficient offsets for different plate scale errors. Such simulations reproduce rather well the variations observed in the data, including the changes between epochs. Note that at this point we have not yet included any image distortion.

The effect of a small plate scale error on the ridge frequency can be approximately modeled as a wavenumber scaling error in the spatial decomposition, namely $\ell_\epsilon = \ell(1-\epsilon)$, causing an apparent frequency shift of the ridge. Using a linear approximation, valid for small ϵ, this can be written as:

$$\Delta\nu = \nu(\ell_\epsilon) - \nu(\ell) = \frac{\partial\nu}{\partial\ell}\Delta\ell = -\frac{\partial\nu}{\partial\ell}\,\epsilon\,\ell \qquad (23)$$

In practice the observed frequency differences result from the combination of a plate scale error and some other terms. Thus, the variation of this frequency difference with epoch, if the only change is a plate scale error, can be measured, and corresponds to:

$$\zeta(P_1, P_2, P_3) \stackrel{\text{def}}{=} \frac{\Delta\nu(P_2) - \Delta\nu(P_1)}{\Delta\nu(P_3) - \Delta\nu(P_1)} \qquad (24)$$

$$= -\frac{\epsilon(P_2) - \epsilon(P_1)}{\epsilon(P_3) - \epsilon(P_1)} \qquad (25)$$

where $\epsilon(P_i)$ is the plate scale error for the epoch P_i.

Similarly, the variation of the rotational splittings first coefficient differences, Δa_1, due to a plate scale error will be proportional to first order to ϵ. Our simulations have shown a residual dependence on frequency and degree, namely:

$$\Delta a_1(P_2) - \Delta a_1(P_1) \cong \mathcal{A}\,(\epsilon(P_2) - \epsilon(P_1)) \qquad (26)$$

where

$$\mathcal{A} = \mathcal{A}_o + \mathcal{A}_\nu\,(\nu - \nu_o) + \mathcal{A}_\ell\,(\ell - \ell_o) \qquad (27)$$

and $\mathcal{A}_o = -580$ nHz, while $\mathcal{A}_\nu = -26$ nHz/mHz and $\mathcal{A}_\ell = 0.13$ nHz, for $\nu_o = 3.333$ mHz and $\ell_o = 150$, using our normalization of the Clebsh-Gordon coefficients.

[1] In this case, the leakage asymmetry is the result of two factors: the contribution of the velocity horizontal component that leaks more power at higher ℓ and a negative plate scale error that has the opposite effect.

Table 3: Mean Plate Scale Errors

Epoch	Plate scale error, ϵ
1996	$-0.0068 \pm 0.00013\%$
1997	$+0.0155 \pm 0.00005\%$
1998	$-0.0730 \pm 0.00018\%$
1999	$-0.2701 \pm 0.00022\%$

We have verified, using our simulations, that for plate scale errors of a fraction of a percent Equations 25 and 27 are satisfied. These simulations show that the plate scale induced frequency error scales with ϵ according to Equation 25 to better than 0.01% on average, with a scatter of 0.3%, for plate scale errors up to 0.12%. Simulations with $\epsilon = 0.16\%$ show a departure from Equation 25 at the 2% level for $\ell \geq 700$, while simulations for $\epsilon = 0.27\%$ show a departure from Equation 25 at the 5% level for $\ell \geq 450$, as illustrated in Fig. 16.

Figure 17 illustrates how well Equation 25 is satisfied for the observed frequency differences. It shows that for the modes whose frequency is above 1.9 mHz (*i.e.*, $n \geq 2$) the relation in Equation 25 is well satisfied, hence the change in frequency differences between epochs can be explained by the change in plate scale.

On the other hand our simulations show that Equation 27 is only satisfied to 2% on average, but the plate scale induced changes in a_1 are themselves much smaller than the corresponding changes in frequency. Our simulations show that the relation breaks down at large degree for large plate scale errors, as illustrated in Fig. 18. Finally, Figure 19 depicts the correlation of the change in a_1 with epoch, and shows that in practice the scatter in the data makes it hard to establish whether Equation 27 is actually satisfied by the measurements.

5.2. Effect of Image Distortion

So far we have ignored the distortion of the observed solar image. Further progress requires the inclusion of the image distortion and the instrument MTF, adding one more level of complexity, but an element that is expected to be somewhat stable with time.

A full ray tracing of the optical design of the MDI instrument, in the *Dynamics Program* configuration, predicts distortions (Scherrer, private communication) that can be modeled as:

$$\epsilon_r \equiv \frac{\Delta r}{r} = a_r((\frac{r}{r_{\rm m}})^2 - 1) \qquad (28)$$

where $a_r = 1.1 \times 10^{-3}$, r is the distance from the detector center, Δr the image distortion, and r_m is the observed image mean radius.

However, this expression does not account for the elliptical shape of the MDI image, an additional distortion that is also on the order of 0.1%. A possible explanation is that the CCD detector is tilted with respect to the focal plane. The shape of the solar image resulting from such a tilt is indeed elliptical, as shown in Appendix A, and a tilt of $\sim 2^{\rm o}$ can account for the observed 0.1% effect.

We have computed leakage matrices that include some image distortion. These were used to generate simulated power ridges that were then fitted as described earlier. In one set of leakage matrix computation we only included an image distortion as described in Equation 28 (hereafter Model 1). In the second set we included the elliptical distortion resulting from a tilt of the detector as well the radial distortion (hereafter Model 2). The resulting frequency differences, as well as the observed ones for 1996, are shown in Figure 20. The distortion of the eigenvalues by differential rotation was included in these calculations.

The effect of an image distortion on the frequency differences, although similar, is different from the effect of a plate scale error. Indeed, the relation expressed in Equation 25 is not satisfied for the simulations that include an image distortion, as shown in the lower panel of Figure 20.

The effect of an image distortion on the odd splitting coefficients is comparable in amplitude to the effect of a similar plate scale error, as illustrated in Figure 21. The effect on the even coefficients is negligible. The mean change in the splitting coefficient offsets is listed in Table 4.

Table 4: Mean Change in Splitting Coefficient Offsets Due to Image Distortion

	Model 1 − Reference	Model 2 − Reference
$\delta(\Delta a_1)$	-0.3457 ± 0.0686	-0.2162 ± 0.0459
$\delta(\Delta a_2)$	0.0017 ± 0.0019	0.0010 ± 0.0012
$\delta(\Delta a_3)$	0.0205 ± 0.0401	0.0127 ± 0.0290
$\delta(\Delta a_4)$	-0.0017 ± 0.0018	-0.0010 ± 0.0011
$\delta(\Delta a_5)$	0.0075 ± 0.0119	0.0051 ± 0.0107
$\delta(\Delta a_6)$	0.0001 ± 0.0005	0.0001 ± 0.0004

Model 1: radial term only
Model 2: radial term and tilt of CCD

5.3. Effect of the Instrumental Point Spread Function

Another point to consider in the leakage matrix calculation is the effect of the instrumental point spread function (PSF). Not only will the smearing of the image by the PSF affect the leakage matrix (especially at high degrees), but it will change with time as the focus changes.

To estimate the PSF of the MDI instrument and its variation with epoch, we ran the `HGEOM` procedure on MDI full-disk images. `HGEOM`, a procedure part of the GONG reduction and analysis software package (`GRASP`), returns an estimate of the azimuthally averaged modulation transfer function (MTF, *i.e.*, the Fourier transform of the PSF), following the methodology described in Toner & Jefferies (1993). This method reduces the 2D solar image to a radial profile (by computing the mean over concentric annuli) and computes the Hankel transform of this profile. By exploiting the zero-crossing properties of the Hankel transform one recovers the true image dimensions and estimates the MTF.

Figure 22 (top panel) shows the PSF for five different full-disk images taken by MDI on five consecutive years. Although their shapes are very similar, the width of the PSF is increasing with the amount of defocus, as expected (Figure 22, lower panel). While the PSF of MDI displays a substantial tail beyond 2 pixels, its core can be approximated by a Gaussian, with a half width at half maximum of 0.8 ± 0.1 pixels. The image sizes estimated by `HGEOM` are consistent with the the plate scale based on the MDI standard reduction pipe-line to within .04 pixels or .008%. This is, of course, to be expected, since the *level 1.8* MDI data processing uses the same algorithm for the limb definition as the GONG procedure.

Simulated ridge frequencies resulting from including the PSF in the computation of the leakage matrix were computed. We used a Gaussian PSF, a Lorentzian PSF as well as the PSF estimated by `HGEOM`. The resulting changes in the frequency offsets and splitting coefficient offsets are shown in Figure 23 as a function of frequency and degree. The changes in frequency offsets are on the order of 0.1 μHz (*i.e.*, a 5 % effect), while changes in Δa_1 are on the order of 0.1 nHz (or a 2% effect).

Variations of the width of the PSF will affect predominantly the amplitude of the leaks with a small effect on the leakage asymmetry (as shown in Rabello-Soares et al. 2001). The change of the limit power spectrum computed for 1996 and 1997 (as shown in Fig. 24 – top panel) is qualitatively similar to the variation of simulated power spectra synthesized using leakage matrix computations that includes the effect of the PSF for two different widths (Fig. 24 – lower panel). Our simulations seem to reproduce the observed changes in amplitude, but for a change in PSF width nearly 5 times larger than the change observed in the corresponding azimuthal averages. This might result from the fact that the true PSF is not azimuthally symmetric and that the azimuthal averages we used so far are in fact poor approximations.

Schou & Bogart (1998) also noticed that the power spectrum of MDI images varies with azimuth (see Figure 1 of their paper). Figure 25 shows power as a function of the azimuthal angle for horizontal wavenumber $k_h = 230$ pixel^{-1} for test images taken in 1999 at four focus settings. This figure shows not only that the power is a function of azimuth, but, as first noticed by

Duvall (private communication), the phase of this angular dependence changes with focus position, changing by nearly 90° between focus positions 4 and 5, corresponding to a change from positive to negative defocus (the best focus at disk center in 1999 was at ≈ 4.1, as shown in the upper panel of Figure 12). Such a change can be explained by the combination of an astigmatism with a positive or negative defocus. Such configuration would produce a PSF that is a function of the azimuthal angle (Bush, private communication).

Tarbell et al. (1997), using phase-diversity analysis, estimated the PSF of the MDI instrument in focus and in its high resolution configuration (*i.e.*, when the image is magnified by a factor 3.2). This PSF shows a clear angular dependence, with a secondary peak with an amplitude of 0.15, attributed to the residual optical aberrations of the instrument components.

Finally, we should also point out that the best focus changes across the CCD by nearly one focus step. This is caused by some residual field curvature and will produce a radial variation of the PSF. The optical characteristics of the MDI instrument are such that the instrumental PSF has to be a function of both radius and azimuth.

5.4. Effects of Image Orientation, P and B_o Angles

The spherical harmonic decomposition is *in principle* computed with respect to an orientation aligned with the solar rotation axis. The location of this axis is determined by two angles, the position angle, P, and the heliographic latitude of the central point of the disk, B_o. The roll angle of the spacecraft is maintained to keep MDI $P_{\rm eff}$ to be zero (where $P_{\rm eff}$ is the position angle of the northern extremity of the rotation axis with respect to MDI CCD detector column orientation). However, Cliff Toner (private communication) estimated the value of $P_{\rm eff}$ by inter-comparing MDI and GONG images, drift scans, and observations taken during the November 1999 transit of Mercury in front of the Sun. He found that $P_{\rm eff} = 0.19^{\rm o} \pm 0.04^{\rm o}$ using May 2000 observation and $P_{\rm eff} = 0.20^{\rm o} \pm 0.05^{\rm o}$ based on the transit of Mercury.

The precision to which B_o is known is directly related to the precision of the Carrington elements, i_C and Ω_C (*i.e.*, the inclination of the solar equator to the ecliptic and the longitude of the ascending node of the solar equator on the ecliptic plane respectively). Giles (1999) showed that these are not perfect and that $\Delta i_C = -0.091^{\rm o} \pm 0.012^{\rm o}$ and $\Delta\Omega_C = -0.1^{\rm o} \pm 0.1^{\rm o}$. The error on B_o is therefore no larger than $0.1^{\rm o}$.

To assess the effect of an error in the image orientation used for the spherical harmonic decomposition, we computed simulated frequency differences by fitting simulated ridges based on a leakage matrix computed with either an error in $P_{\rm eff}$ or $B_{\rm o}$ of $0.25^{\rm o}$. Figure 26 compares the observed frequency differences for 1996 to the theoretical differences resulting from including such orientation error. The effect of a quarter of a degree error is unnoticeable for the frequency differences (less than 1% of relative change of the offsets, for either angle), while an error in $P_{\rm eff}$ affects noticeably the odd splitting coefficients. This should not come as a surprise: an error in the orientation of the image with respect to the rotation axis will affect the relative mode power as a functions of m/ℓ – in a way conceptually similar to the distortion of the eigenfunctions by the differential rotation, see Section 3.2 – and will therefore affect the ridge rotational splittings. The smooth dependence of Δa_i with ℓ for a conservative $0.25^{\rm o}$ error in $P_{\rm eff}$ seen in Figure 26 is not readily seen in the MDI measurements. But this effect is small and is most likely masked by the random scatter and other systematics present in the measurements.

6. Results

6.1. Error Budget

Table 5 compares the range of uncertainties resulting from ridge fitting, *i.e.* the formal error bars of the ridge fitting, to the magnitude of the ridge to mode corrections, for both the frequency and the rotational splitting coefficients. While the uncertainties resulting from the fitting scale with the ridge width, Table 5 shows that the required corrections are about an order of magnitude larger than the uncertainties. On the other hand, to produce useful high-degree mode parameters we need to be able to compute these corrections with a precision substantially smaller than the uncertainties.

Table 6 presents an error budget for the ridge to mode correction, breaking it up as a function of the different elements used to compute the cor-

Table 5: Comparison between Uncertainty and Ridge to Mode Correction

	frequency [μHz]	frequency splittings [nHz]		
		a_1	a_3	a_5
uncertainty$^{(a)}$	0.1 – 0.6	0.3 – 1.0	0.2 – 0.8	0.15 – 0.7
largest correction$^{(b)}$	4.0	10.0	5.0	2.0

$^{(a)}$ given range corresponds to a ridge width range of 10 – 60 μHz
$^{(b)}$ for the $100 \leq \ell \leq 900$ range

rection. The listed typical values are based on our best estimates of these different elements resulting from the current analysis.

Now that these effects are better understood and that we better understand the MDI instrument imaging imperfections, we can – and will in the near future – reprocess the *Dynamics* data, and include the correct image scale and the known image distortion in the spatial decomposition. Table 7 presents an error budget projected for the best achievable values of these elements. The sobering conclusion of this exercise is that our estimate of the achievable precision of the frequency and splitting coefficients corrections are still comparable to the fitting uncertainties.

For the frequency corrections, the dominant contributions come from the plate scale error and the image distortion. If both could be known to an accuracy of 10^{-5}, the precision of the correction would be further reduced to 0.06 μHz, a *useful* value since it would then become substantially smaller than the uncertainties.

The precision of the fit of an ellipse to the limb of the image is likely to be 10^{-5} (*i.e.*, fitting 5 parameters to some 3000 limb positions). But it would be presumptuous to assert that the algorithmic definition of the limb can be accurate to that level. Characterizing the instrument image distortion to the 10^{-5} level is also very challenging. The image distortion in the MDI instrument is only at the 10^{-3} level (corresponding to displacements smaller than 0.95 pixels). We thus need to know the distortion with a relative precision of 1% (*i.e.*, 1/100 of a pixel) to reach the 10^{-5} level.

For the splitting coefficient a_1 corrections, the dominant contributions come from the P angle, and might prove to be a fundamental limitation for the use of high degree rotational splittings. If we could reduce the error in the position angle by an additional order of magnitude (*i.e.*, to 0.005°), the precision of the correction in a_1 would be further reduced to less than 0.1 nHz, a value now smaller than the fitting uncertainties. At that level, contributions from the precision of the plate scale, differential rotation and image distortion to this correction are comparable to that from the image orientation.

The determination of the shape of the differential rotation just below the surface can be improved by including high degree splittings, but that shape must be known to correct these splittings, as they are the result of ridge fitting. It is likely that a bootstrapping method — or some other optimized methodology — can be devised to disentangle this problem. This still leaves the uncertainty of the image orientation as a substantial contribution.

On the other hand, if we focus on the precision of relative changes, *i.e.* differences between epochs, we can be more optimistic. Indeed, the residual systematic errors introduced by the imperfect corrections are likely to be nearly constant with time.

6.2. Changes with Solar Cycle

The four *Dynamics* data epochs analyzed for this study were taken during the rising part of solar cycle 23. The first set, observed in 1996 corresponds to a period when the sun's magnetic activity was nearly at its minimum, while for the forth data set, taken in 1999, the sun was near maximum activity. The average relative sunspot index for the four epochs is shown in Table 8, *i.e.* the ratio of the sunspot number to the maximum value of cycle 23, reached in 2000. We can thus study the changes of high-degree p-mode parame-

Table 6: Error Budget for the Ridge to Mode Correction

parameter	typical values	corresponding change in frequency [μHz]	corresponding change in a_1 [nHz]
plate scale	0.01 – 0.27 %	0.2 – 6.0	0.06 – 1.6
differential rotation	4.4 – 6.2 %	0.01 – 0.8	0.4 – 0.7
image distortion	0.1%	1.0 – 1.5	0.2 – 0.4
instrument PSF	(*)	0.05 – 0.15	0.05 – 0.1
image orientation, $P_{\rm eff}$	0.25°	0.03	0.01 – 2.0
image orientation, $B_{\rm o}$	0.1°	0.004	0.012

(*) Changes resulting from using a Gaussian versus a Lorentzian PSF
Note also that the values tabulated are unsigned magnitude

Table 7: Optimal Error Budget for the Ridge to Mode Correction

parameter	achievable values	change in frequency [μHz]	change in a_1 [nHz]
plate scale	0.01 %	0.220	0.06
differential rotation (*)	0.03 %	0.054	0.045
image distortion	0.01 %	0.150	0.04
instrument PSF	(†)	0.015	0.01
image orientation, $P_{\rm eff}$	0.05°	0.006	0.40
image orientation, $B_{\rm o}$	0.02°	0.001	0.002
correction estimated precision		0.272	0.409
fitting uncertainties		0.1 – 0.6	0.3 – 1.0

(*) values scaled from our worst case, see discussion in text
(†) 1/10th of corresponding values in table 6

ters with the solar cycle by comparing results from our four data sets

6.2.1. Frequency

To estimate high-degree mode frequency changes with the solar cycle, we have corrected the ridge frequencies for the plate scale error (as described in Section 5.1, Eq. 23). We thus assume that all other instrumental effects are either constant with time or that the impact of their variation is small, effects such as the image distortion, the instrumental PSF, and the error in the P and $B_{\rm o}$ angles.

Figure 27 shows frequency changes with respect to 1996, as a function of frequency and degree. These plots show that these differences increase with frequency, degree and sunspot number. To compare these changes to other investigators measurements, we show in Figure 28 mean frequency changes around 3 mHz (*i.e.*, the frequency change averaged over the 2.6 to 3.4 mHz frequency range), with respect to 1996 values, as a function of degree. These are compared to estimates based on intermediate-degree observations ($\ell \leq 150$) taken during the raising part of cycle 22 by Libbrecht & Woodard (1990), a period that corresponds to a change in the sunspot number index of 85, and the raising part of cycle 23 by Howe, Komm & Hill (1999), a period that corresponds to a change in the sunspot number index of 56. A linear extrapolation with respect to degree of the shifts based on intermediate-degree observations agrees rather well up to $\ell = 600$. This confirms that these shifts scale with the inverse of the mode mass, indicating that the source of the perturbation responsible for these shifts is located very close to the surface. There are also claims of a sharp drop of the fre-

Table 8: Relative Average Sunspot Index

Year	Relative Index	Sunspot number change with respect to 1996
1996	7 %	
1997	16 %	11
1998	46 %	47
1999	72 %	79

quency shift at high frequencies. In Libbrecht & Woodard (1990), the drop is seen around 4 mHz, while in our measurements it seems to occur at higher frequency (*i.e.*, around 4.5 mHz; see top panel of Figure 27). One also notices that besides a linear increase of the frequency shift with degree, there is a *bump* centered on ℓ=700.

We have checked our assumption that all other instrumental effects can be neglected for our estimate of the frequency shifts shown in Figure 27. Figure 29 presents residual frequency offsets with respect to 1996, namely the the quantity $\Delta\nu(P_i) - \Delta\nu(1996)$, where $\Delta\nu = \tilde{\nu}' - \nu$, $\tilde{\nu}'$ is the ridge frequency corrected for the plate scale error, and ν the mode frequency computed from resolved modes at low and intermediate degrees. This figure shows that while there remains a residual discrepancy, there are no systematic changes with epoch, except for the values at low frequencies ($\nu < 1.9$ mHz). We can thus be confident that the variations seen Figure 27 are dominated by solar cycle effects, except for the increase in the frequency shift at low frequency, that is most likely an artifact resulting from some residual systematic errors.

6.2.2. Splitting Coefficients

The splitting coefficients were corrected for the plate scale error and their change with solar cycle estimated. Figure 30 shows the changes of the odd coefficients (a_1 and a_3) with respect to 1996, for different epochs as a function of frequency and degree. The plots show that the changes of the a_1 coefficient increase with frequency, while displaying only a weak dependence on degree. Although the shift increases with activity, it is larger in 1998 than in 1999. The changes for a_3 are very small, and the scatter large enough to be consistent with zero.

To check if instrumental effects, other than the plate scale error, can be neglected and are not causing the changes seen in a_1, we again computed the residual a_1 offsets with respect to 1996, namely the the quantity $\Delta a_1(P_i) - \Delta a_1(1996)$, where $\Delta a_1 = \tilde{a}_1' - a_1$, $\tilde{a}_1'$ is the ridge fitting value corrected for the plate scale error, and a_1 the mode fitting value. While there remains a residual discrepancy, there appears to be no systematic variations with frequency, degree, or epoch.

Similarly we have looked at the changes in the even splitting coefficients and in the residual offsets with respect to 1996, also as a function of frequency and degree. The changes in a_2 appear systematic with frequency, degree and epoch, while the scatter in the residual a_2 offsets are large and inconclusive.

In Figure 31, the mean splitting coefficient change and the mean residual offset, corresponding to the average over all available modes, are plotted as a function of epoch. Since the mean splitting coefficient changes track the mean residual offsets (except for a_6), we must conclude that the changes with epoch result from residual systematic errors, and are not an indication of changes due to solar activity.

6.2.3. Asymmetry Parameter

Unlike the other mode parameters, the estimate of the asymmetry parameter is not much affected by the fact that we observe and fit ridges instead of individual modes. Korzennik (1999) pointed out that the asymmetry of the ridge seems to be the same as the asymmetry of the modes that are blended into that ridge. We found from our simulations that these differences are smaller than 10% up to $\ell = 700$ when including the various instrumental effects described in Section 5, as illustrated in Figure 32.

Figure 33 shows the measured asymmetry coefficients for the 1996 *Dynamics* observations. The asymmetry is mainly a function of frequency, except for the low order modes ($n = 0$ and $n = 1$) whose asymmetry is larger. In Figure 34 we compare our determinations of the mode asymmetry[2] with values obtained for low-degrees ($\ell < 3$) using GOLF data (Thiery et al. 2000) and for intermediate degrees using GONG observations (Basu & Antia 2000). Our measurements agree very well with the GONG determinations in the 2.4 to 3.8 mHz range.

In Figure 35 we compare the asymmetry for different epochs, shown as a function of frequency and degree. Except for the f-mode, there seems to be no change with epoch, while the asymmetry of the f-mode appears to have changed systematically, suggestive of a solar activity effect.

6.2.4. Linewidth

Measurements of the mode linewidths provide clues to the damping mechanisms of the solar oscillations and are directly related to the lifetimes of the modes. Previous measurements have shown that the linewidths increase both with frequency and degree (Hill et al. 1996).

Korzennik (1990) proposed a simple formula to estimate the mode linewidth from the the ridge linewidth, namely:

$$\Gamma^2_{\rm ridge} = \Gamma^2_{\rm mode} + \Gamma^2_{\rm WF} + (s\,\frac{d\nu}{d\ell})^2 \qquad (29)$$

where $\Gamma_{\rm WF}$ is the width of the window function, $s\,d\nu/d\ell$ corresponds to the effective leakage matrix width in frequency space, where the empirical coefficient $s \approx 0.5$.

Figure 36 shows the estimated mode linewidth for the 1996 *Dynamics* observations, as well as linewidths estimated for low and intermediate degrees ($0 < \ell < 250$) based on 360-day long time-series of MDI *Structure Program* (Schou 1999). Preliminary estimates of linewidths for high-ℓ modes ($700 < \ell < 1800$) based on high-resolution MDI observations (Duvall et al. 1998) are also included. Note that modes whose corrected linewidth are smaller than the width of the window function are not shown in Figure 36, since the correction scheme of Eq. 29 is not valid.

Our simple minded linewidth correction scheme connects reasonably well the MDI *Structure* linewidths (*i.e.*, low and intermediate mode fitting) with the corrected MDI *Dynamics* linewidths, but we could not reconcile the Duvall et al. (1998) determinations based on high-resolution MDI observations. We do see in our measurements the trend seen in Duvall et al. (1998) at higher degrees, namely that the linewidth of the f-modes increases with degree faster than the linewidth of the p_1 modes. Our measurements suggest a cross over around $\ell = 1000$, while the Duvall et al. (1998) estimates imply a cross over below $\ell = 700$.

Figure 37 shows the relative change of the corrected linewidths with epoch – using 1996 as reference – as a function of frequency. The magnitude of these changes – on the order of 5 to 10% – do not correlate with solar activity, nor do they scale with the plate scale error. The fact that the linewidths of all three later epochs have changed in a systematically similar way with respect to 1996 is intriguing and suggestive of residual systematic errors at the 5 to 10% level.

7. Conclusion

We believe that we have shown that one can construct a physically motivated model (rather than some *ad hoc* correction scheme) of the ridge power distribution that results in a methodology that can produce an unbiased determination of high-degree modes, once the instrumental characteristics are well understood and precisely measured.

We have gained substantial insight in the understanding and modeling of the instrumental effects of the Michelson Doppler Imager, including plate scale error, image distortion, point spread function and image orientation. Now that we better understand the MDI instrument imaging imperfections, we can – and will in the near future – reprocess the *Dynamics* data, and include the correct image scale and the known image distortion in the spatial decomposition.

We have produced an error budget for the characterization of high degree mode parameters. Beyond MDI *Dynamics* observations, this has direct applications on the characterization of the

[2] we plotted the asymmetry parameter B, as defined in Nigam & Kosovichev (1998), where $B = \frac{\alpha/2}{(1-\alpha^2/2)}$

GONG+ instruments and the reduction of the GONG+ observations as well as on the characteristics of the Helioseismic/Magnetic Imager (HMI) instrument planned for the Solar Dynamics Observatory (SDO) mission, if one wishes to make effective use of the high degree modes accessible to these experiments.

Last but not least, we also see changes with solar activity in the high degree frequencies and the asymmetry of the f-mode. Our attempt to see changes in splitting coefficients and mode linewidths remained inconclusive.

Acknowledgments

We wish to thank Rock Bush providing us with the MDI best focus estimates, Phil Scherrer for the MDI image distortion model, Jørgen Christensen-Dalsgaard for estimates of the horizontal-to-vertical displacement ratio from his solar model, Ted Tarbell for the PSF of MDI in high resolution mode, and Cliff Toner for his estimates of MDI roll angle. Sunspot index data provided by the SIDC, RWC Belgium, World Data Center for the Sunspot Index, Royal Observatory of Belgium.

The Solar Oscillations Investigation - Michelson Doppler Imager project on SOHO is supported by NASA grant NAG5–8878 and NAG5–10483 at Stanford University. SOHO is a project of international cooperation between ESA and NASA. SGK was supported by Stanford contract PR–6333 and NASA grant NAG5–9819.

A. Elliptical Image Distortion

The observed elliptical shape of the solar image is likely to be the result of an unwanted tilt of the detector plane with respect to the focal plane. This appendix shows how the combination of the distortion resulting from this tilt with the optical package distortion (or cubic distortion) can be estimated. First the cubic distortion is applied to the undistorted image (x_0, y_0)

$$x = x_0 + \epsilon_r x_0 \tag{A1}$$
$$y = y_0 + \epsilon_r y_0 \tag{A2}$$

where $\epsilon_r = \epsilon_r(r_0)$ is given by Equation 28 and $r_0 = \sqrt{x_0^2 + y_0^2}$, while (x, y) are the reference coordinates in the focal plane that would correspond to the coordinates for a perfectly aligned detector.

To model the image distortion due to a tilt of the CCD, the reference coordinate system (x, y) is first rotated around the optical axis (the z-axis) by an angle β, which defines the direction around which the detector is tilted (the x'-axis):

$$x' = x\cos\beta + y\sin\beta \tag{A3}$$
$$y' = -x\sin\beta + y\cos\beta. \tag{A4}$$

The effect of a tilt by an angle α around the x'-axis is then computed using a simple pinhole camera model. It is easy to show that such a model leads to the following equations:

$$x'' = x'(1 + \frac{y'}{f}\,\alpha) - x'\frac{\alpha^2}{4} \tag{A5}$$
$$y'' = y'(1 + \frac{\alpha^2}{2} + \frac{y'}{f}\,\alpha) - y'\frac{\alpha^2}{4} - \frac{r_{\rm m}^2}{f}\,\alpha \tag{A6}$$

where f is the effective focal length and $r_{\rm m}$ the observed image mean radius, both of which are measured in the same units as x' and y'. Note that the second term in both equations assures that the distorted and undistorted images have the same mean radius, while the third term in the second equation keeps the center of both images unchanged.

Finally, the coordinate system is rotated back, around the z-axis, to be co-aligned with the original reference coordinates system:

$$x''' = x''\cos\beta - y''\sin\beta \tag{A7}$$
$$y''' = x''\sin\beta + y''\cos\beta \tag{A8}$$

and the image distortion is given by:

$$\delta_x = x''' - x_0 \tag{A9}$$
$$\delta_y = y''' - y_0 \tag{A10}$$

where (x''', y''') are the observed (*i.e.* actual) coordinates and (x_0, y_0) are the undistorted ones.

Due to the tele-photo nature of the MDI optical package (Scherrer et al. 1995), the effective focal length f defined in Equations A5 and A6 is not the one that reproduces the image size. A complete ray trace of the MDI optical system (Scherrer, private communication) produces an estimate for f of 13000 pixels.

Various observational methods have been used to determine the parameters of the distortion, some of which are described below. Results are summarized in Table 9. With $\beta = 56^{\rm o}$ and $\alpha = 2.59^{\rm o}$, the model reproduces rather well the nearly elliptical images of MDI. The resulting shape of the limb matches an ellipse to 10^{-6} (to be compared to the 0.1% departure from a circle), and the resulting image distortion pattern is shown in Figure 38.

An extensive series of ground tests were completed prior to launch to verify the performance of the MDI instrument (Zayer et al. 1993). In one of them, a grid target was imaged to evaluate, amongst other things, the image distortion. The distortion was determined by measuring the change in shape of the grid target as it was imaged onto different positions within the field of view. This distortion was fitted to the parameterized representation expressed by Equations A9 and A10, leaving α, f and a_r to be freely adjustable parameters. The fit lead to a_r some 11% higher and α some 5% lower than expected. This fit also lead to a value of f some 50% higher than predicted. The higher effective focal length is surprising since ray tracing is expected to produce a reliable value for this parameter. While these are pre-flight measurements, and thus cannot account for changes that could have occurred during deployment of the satellite, the nature of the manufacturing and assembly of the optical package make such post-launch changes highly improbable. On the other hand it is possible that some subtle aspect of the ground test has not been accounted for.

In flight off-center continuum intensity images were acquired in February 2001 — with MDI operating in focus position 3 — to further study the image distortion. When the solar images are centered in different parts of the detector, the distortion will affect them in a different way and the shape of the limb will change with each image position. Using again the image distortion parameterized by Equations A9 and A10, the predicted shape of the limb can be computed as a function of image position, and compared to the observed limb profiles. The best match between predicted and observed limb shapes was achieved for $\alpha = 2.6^{\rm o}$, $\beta = 56^{\rm o}$ and $f = 12940$.

Finally, images obtained during rolling maneuvers of the spacecraft in March 1997 and November 2001 were also used to characterize the distortion. These images were averaged for each roll angle and rotated back to $P_{\rm eff} = 0$. The resulting images, which are dominated by the supergranulation, are then used to estimate the differential distortion by correlating each image with an image in the center of the time range. In this case f was kept fixed while the same distortion model was again fitted to the data. Two estimates were made using these images. The first (hereafter *method 1*) is made using the offset of the center of the images, while the other (hereafter *method 2*) is made using the stretching of the images. The results are inconsistent as summarized in Table 9. In particular *method 2* always produces higher values of α than *method 2*. Again, a larger value of f would be required to reconcile results from both methods.

Table 9: Summary of the Characterization of the Model of MDI Image Distortion

Method	α	β	f	a_r
Match limb shape	$2.59^{\rm o}$	$56^{\rm o}$	Fixed	Fixed
Pre-flight target grid	$2.45^{\rm o}$		19604.4	1.2×10^{-3}
Image offset	$2.6^{\rm o}$	$56^{\rm o}$	12940.0	Fixed
1997 roll, method 1	$1.80^{\rm o}$	$52^{\rm o}$	Fixed	Fixed
1997 roll, method 2	$1.97^{\rm o}$	$59^{\rm o}$	Fixed	Fixed
2001 roll, method 1	$1.71^{\rm o}$	$53^{\rm o}$	Fixed	Fixed
2001 roll, method 2	$2.43^{\rm o}$	$50^{\rm o}$	Fixed	Fixed

Although the parameters resulting from the different methods used to characterize the image distortion of MDI do not agree as well expected, the distortion pattern resulting from a tilt of the detector is a rather good model of the observed distortion. The fact that the model parameters are so different when using different methods might be attributed to the complicated instrumental PSF of the MDI optical package that is not fully known and therefore cannot be taken into account. In particular the different observational methods described above use features of the image at different spatial scales (or spatial wavenumbers) to estimate the image distortion. The PSF may also explain why the ellipticity of the images changes significantly when the images are strongly defocused. Another possible explanation may, of course, be that other types of distortions, such as non square pixels, are present.

REFERENCES

Bachmann, K.T., Duvall, T.L.Jr., Harvey, J.W., and Hill, F. 1995, ApJ, 443, 837

Basu, S., and Antia, H.M. 2000, ApJ, 531, 1088

Bush, R. I., Chu, K., & Kuhn, J. R. 2001, American Geophysical Union, Fall Meeting 2001, abstract #SH11B-0715, 715

Christensen-Dalsgaard J., 1997, Lecture Notes, Aarhus Universitet, Denmark

Christensen-Dalsgaard J., et al., 1996, Science 272, 1286

Duvall, T.L., Kosovichev, A.G., Murawski, K. 1998, ApJ, 505, L55

Giles, P, 1999, Ph.D. Dissertation, Stanford University.

Gough, D.O., 1980, in *Nonradial and Nonlinear Stellar Pulsation*, ed. H.A. Hill and W.A. Dziembowski (Springer-Verlag, Berlin), p. 273

Hill, F. et al. 1996, Science, 272, 1292

Howe, R., Komm, R. and Hill, F. 1999, ApJ, 524, 1084

Korzennik S.G., 1999, ESA SP 418: Structure and Dynamics of the Interior of the Sun and Sun-like Stars, eds. S.G. Korzennik, A. Wilson, ESA Publications Division, Noordwijk, The Netherlands, p. 933

Korzennik S.G., 1990, Ph.D. thesis, Univ. of California, Los Angeles

Libbrecht, K.G, and Woodard, M.F. 1990, Nature, 345, 779

Libbrecht, K.G., and Kaufman, J.M. 1988, ApJ, 324, 1172

Nigam, R. & Kosovichev, A. G. 1998, ApJ, 505, L51

Rabello-Soares, M. C., Basu, S., Christensen-Dalsgaard, J., & Di Mauro, M. P. 2000, Sol. Phys., 193, 345

Rabello-Soares, M. C., Korzennik, S. G., & Schou, J. 2001, Proceedings of the SOHO 10/GONG 2000 Workshop: Helio- and asteroseismology at the dawn of the millennium, 2-6 October 2000, Santa Cruz de Tenerife, Tenerife, Spain. Edited by A. Wilson, Scientific coordination by P. L. Pallé. ESA SP-464, Noordwijk: ESA Publications Division, ISBN 92-9092-697-X, 2001, p. 129 - 136, 464, 129

Rhodes, E. J., Reiter, J., Schou, J., Kosovichev, A. G., & Scherrer, P. H. 2001, ApJ, 561, 1127

Rhodes E.J., Reiter J., Kosovichev A.G., et al., 1999, ESA SP 418: Structure and Dynamics of the Interior of the Sun and Sun-like Stars, eds. S.G. Korzennik, A. Wilson, ESA Publications Division, Noordwijk, The Netherlands, p. 73

Ritzwoller, M. H. & Lavely, E. M. 1991, ApJ, 369, 557

Scherrer P.H., Bogart R.S., Bush R.I., et al., 1995, Sol. Phys.. 162, 129

Schou, J. 1999, ApJ, 523, L181

Schou et al., 1998, ApJ, 505, 390

Schou J., Bogart R.S., 1998, ApJ, 504, L131

Schmidt, W., Stix, M., & Wöhl, H. 1999, A&A, 346, 633

Snodgrass, H. B. & Ulrich, R. K. 1990, ApJ, 351, 309

Tarbell T.D., Acton D.S., Frank Z.A., 1997, Adaptive Optics 96, OSA Technical Digests Vol. 13

Thiery, S., Boumier, P., Gabriel, A.H., et al. 2000, A&A, 355, 743

Toner, C. G. & Jefferies, S. M. 1993, ApJ, 415, 852

Woodard, M. F. 2000, Sol. Phys., 197, 11

Woodard, M. F. 1989, ApJ, 347, 1176

Zayer, I., Bogart, R. S., Hoeksema, J. T., & Tarbell, T. 1993, AAS/Solar Physics Division Meeting, 25, 1192

This 2-column preprint was prepared with the AAS LaTeX macros v5.0.

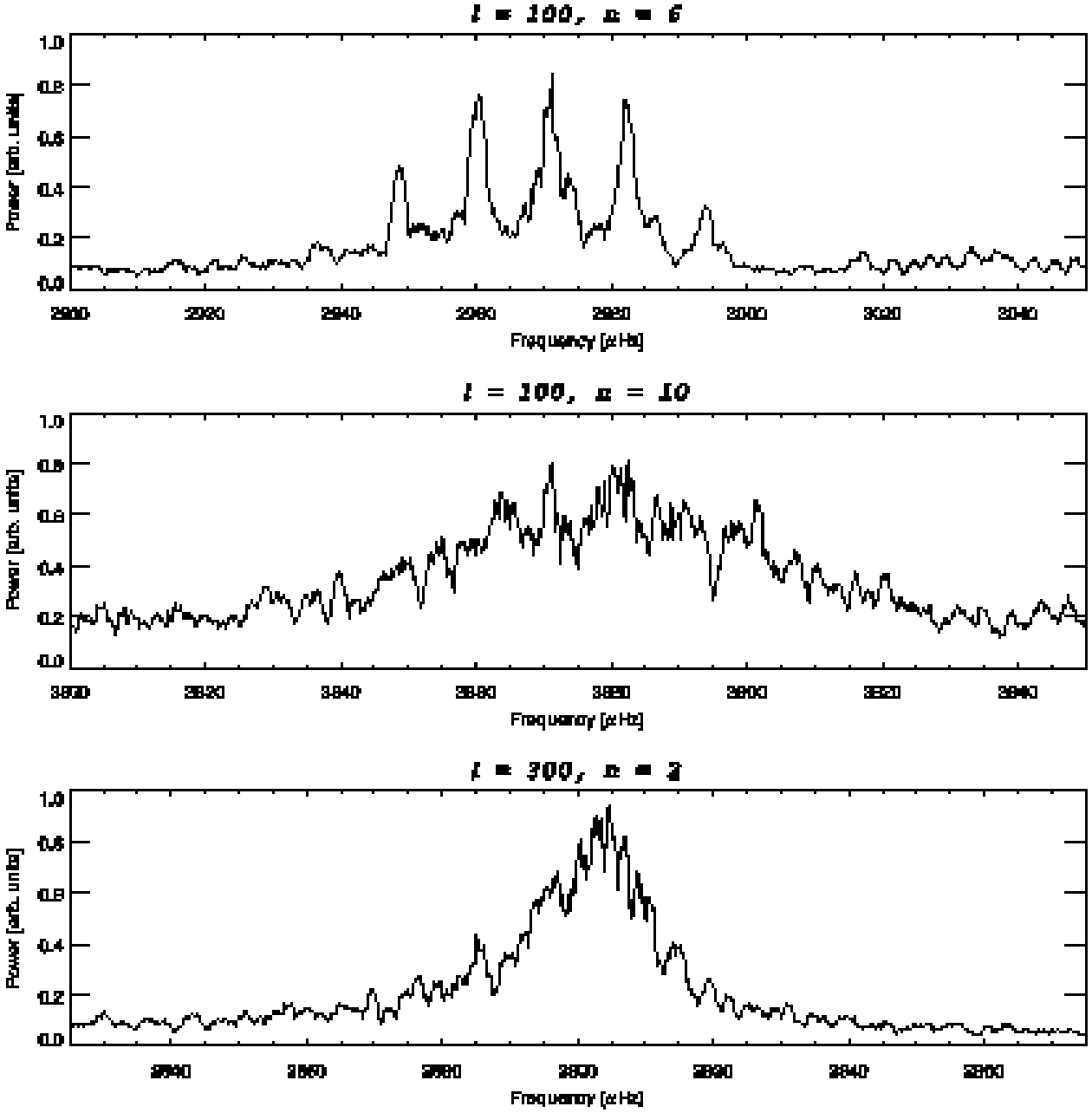

Fig. 1.— MDI sectoral power spectra, for *Dynamics* 1999 and for $(\ell, n) = (100, 6), (100, 10)$ and $(300, 2)$, computed using a 9th order sine multi-taper. At low degree and low order (top panel) individual modes are well resolved: the isolated peak at 2970 μHz is the target mode while the others are the spatial leaks. Otherwise the peaks are blended: the middle panel shows the spectrum for the same degree but at higher order where mode blending results from larger mode widths due to shorter life times. The bottom panel shows the spectrum at roughly the same frequency as in the top panel but at a higher degree, where mode blending results from a smaller mode spacing ($d\nu/d\ell$) as well as shorter life time.

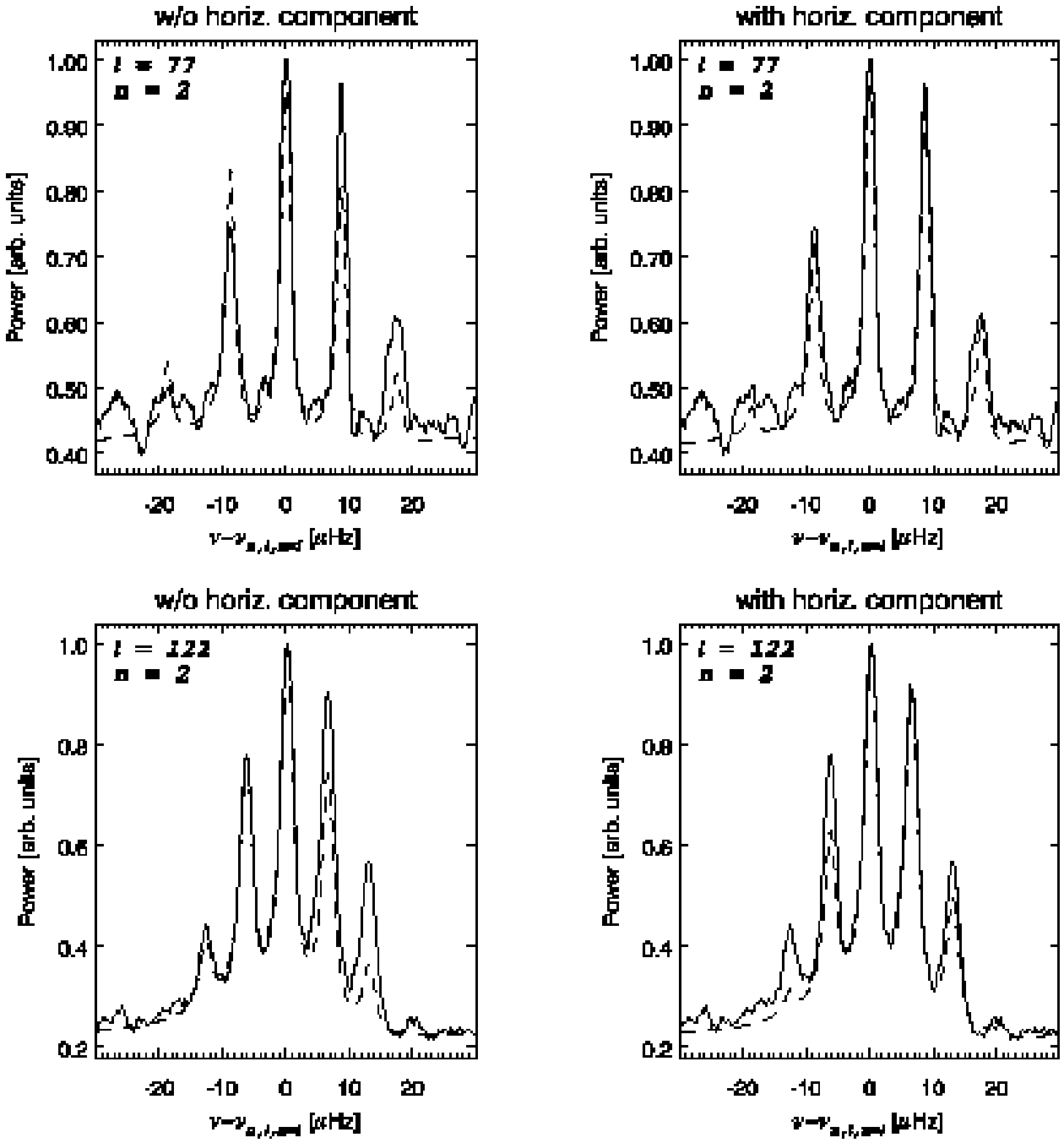

Fig. 2.— Synthetic (dashed line) and observed (continuous line) sectoral limit spectra, *Dynamics* 1996, for $n = 2$ and $\ell = 77$ and $\ell = 122$ in the top and bottom rows respectively. Synthetic spectra computed using leakage matrices without and with the inclusion of the horizontal component are plotted in the left and right columns respectively.

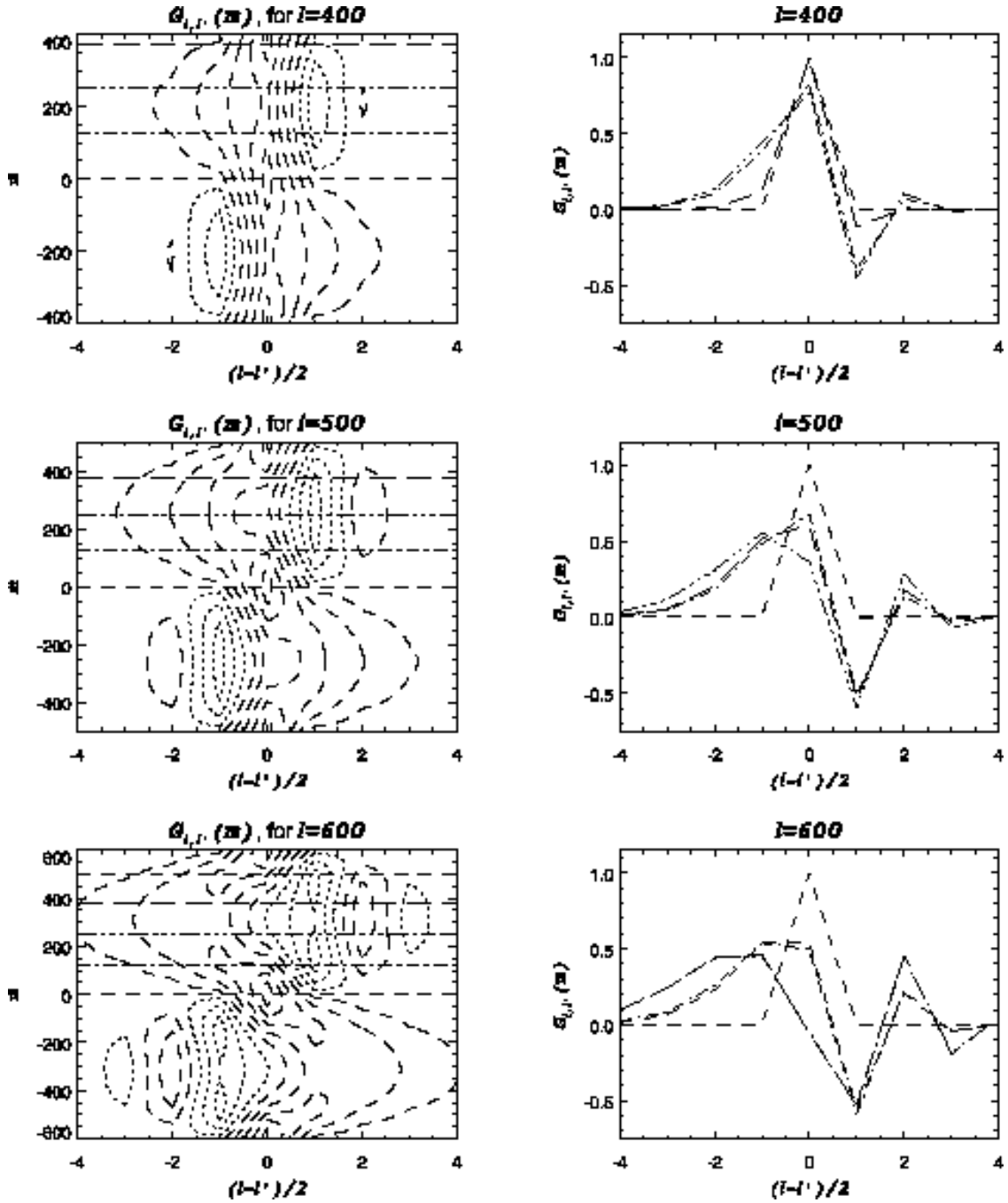

Fig. 3.— Perturbation of the leakage matrix by the solar differential rotation: $G_{\ell,\ell'}(m)$, for $\ell = 400, 500$ and 600, at $n = 3$, see definition in the text. The panels on the left show the $G_{\ell,\ell'}$ coefficients as a function of $p = (\ell - \ell')/2$ and m (dash lines and dotted lines correspond to positive and negative contour levels respectively), while the panels on the right show profiles at fixed m, for the m values indicated by the horizontal lines on the corresponding left panel.

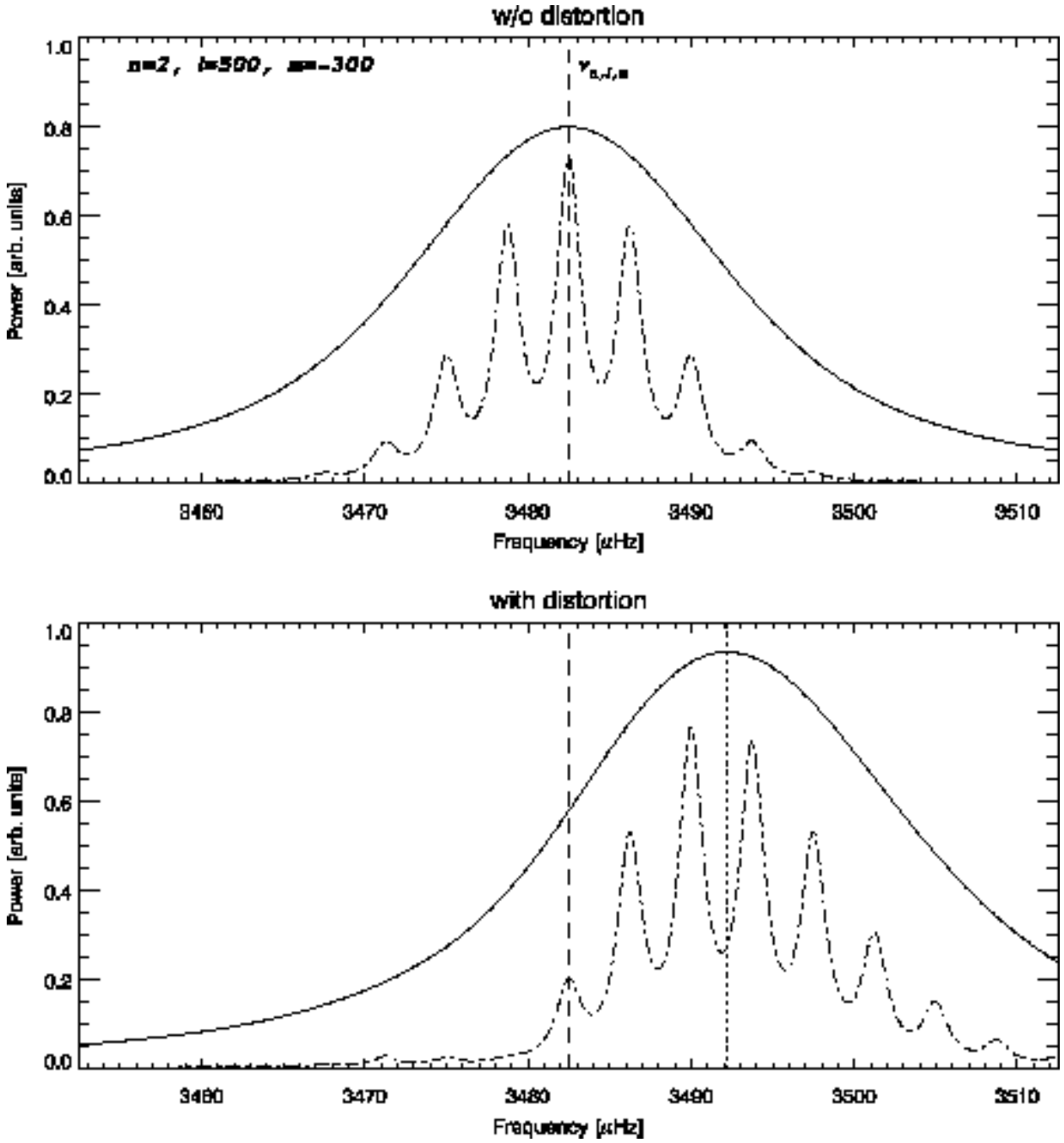

Fig. 4.— Synthetic power spectrum computed for the $n = 2$, $\ell = 500$, $m = -300$ mode without and with the inclusion of the effect of the distortion of the eigenfunctions by the differential rotation (top and bottom panel respectively), and neglecting the horizontal component of the leakage matrix. The dot-dashed lines show the power spectra that would be observed if the mode linewidth was one tenth of the observed value. The vertical dash and dot lines indicate the mode frequency and the peak of the ridge respectively — displaced in this case by some 9.7 μHz.

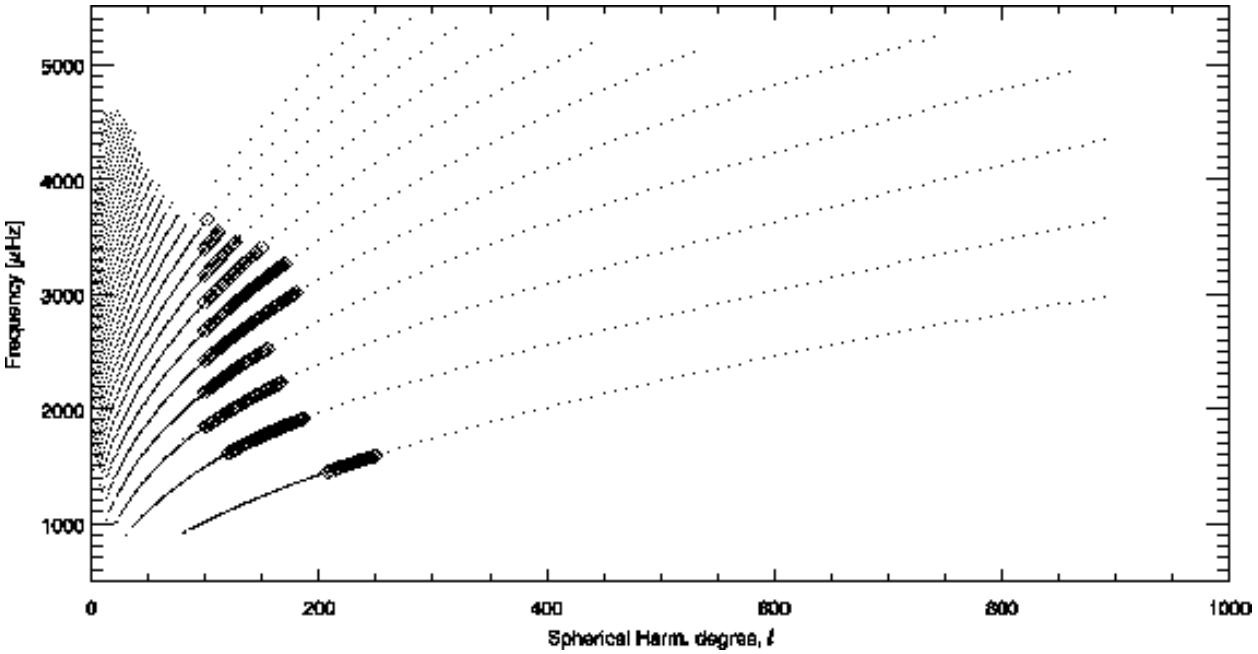

Fig. 5.— This ℓ–ν diagram illustrates the region of overlap between mode fitting and ridge fitting. The overlapping modes are marked as diamonds.

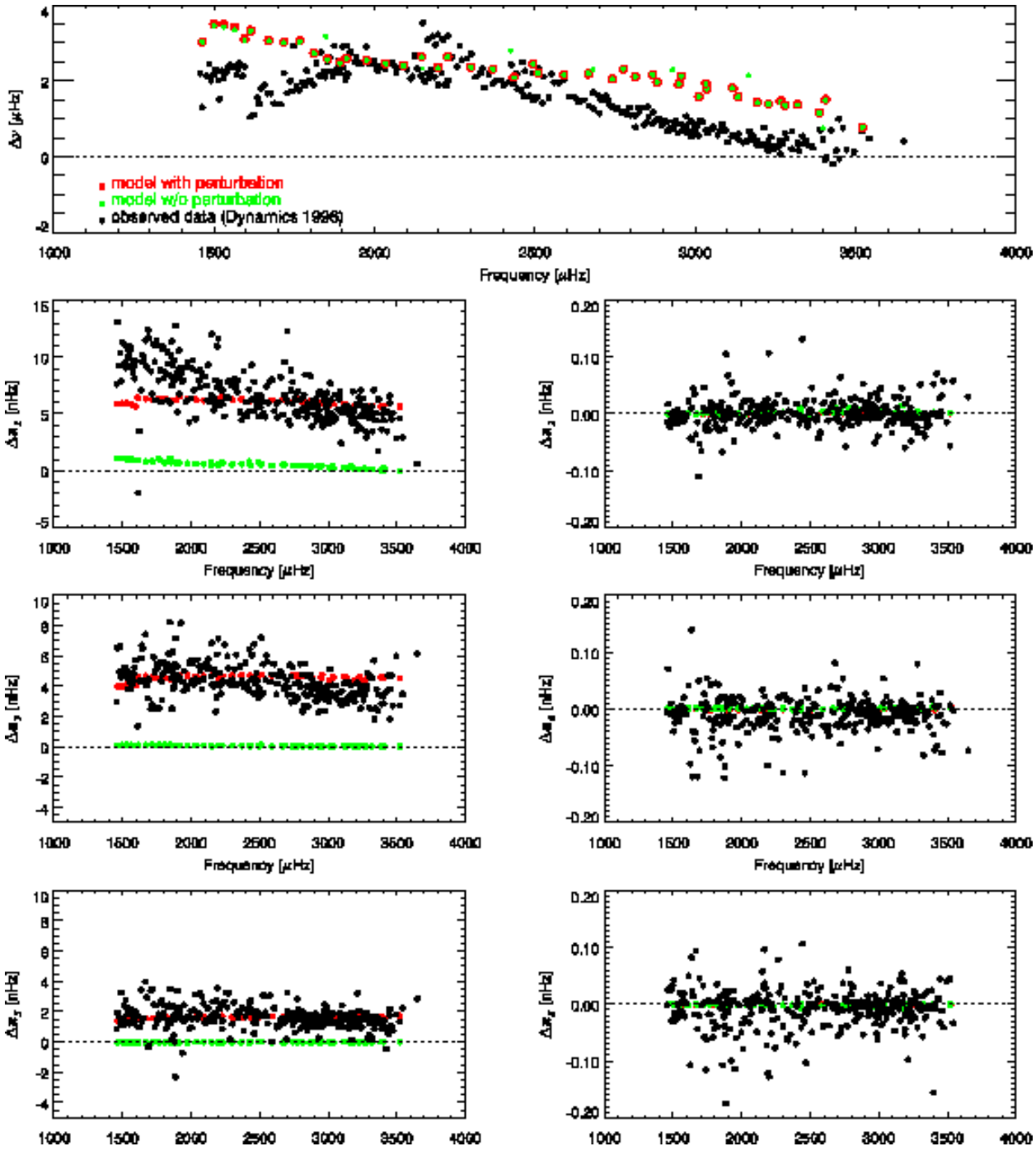

Fig. 6.— Differences between ridge and mode frequencies, and ridge and mode splitting coefficients, as a function of frequency, for the *Dynamics* 1996 data (black points). These differences are compared to theoretical differences (for the same set of modes) computed from simulated power spectra without and with the inclusion of the effect of the distortion of the eigenfunctions by the differential rotation (green and red points respectively).

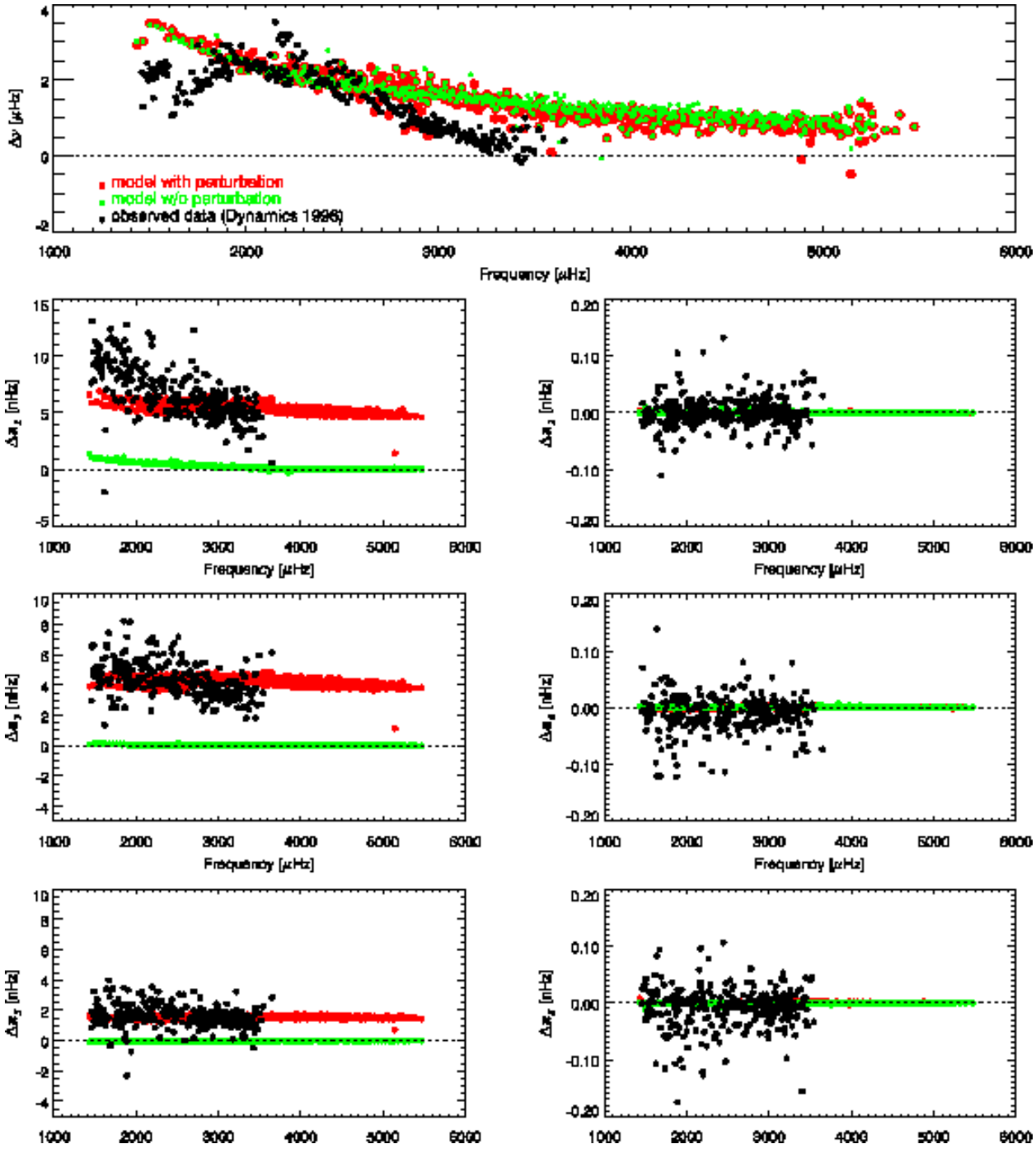

Fig. 7.— Plot similar to Fig. 6: differences between ridge and mode frequencies, but with theoretical differences extending to spherical harmonic degrees up to $\ell = 900$.

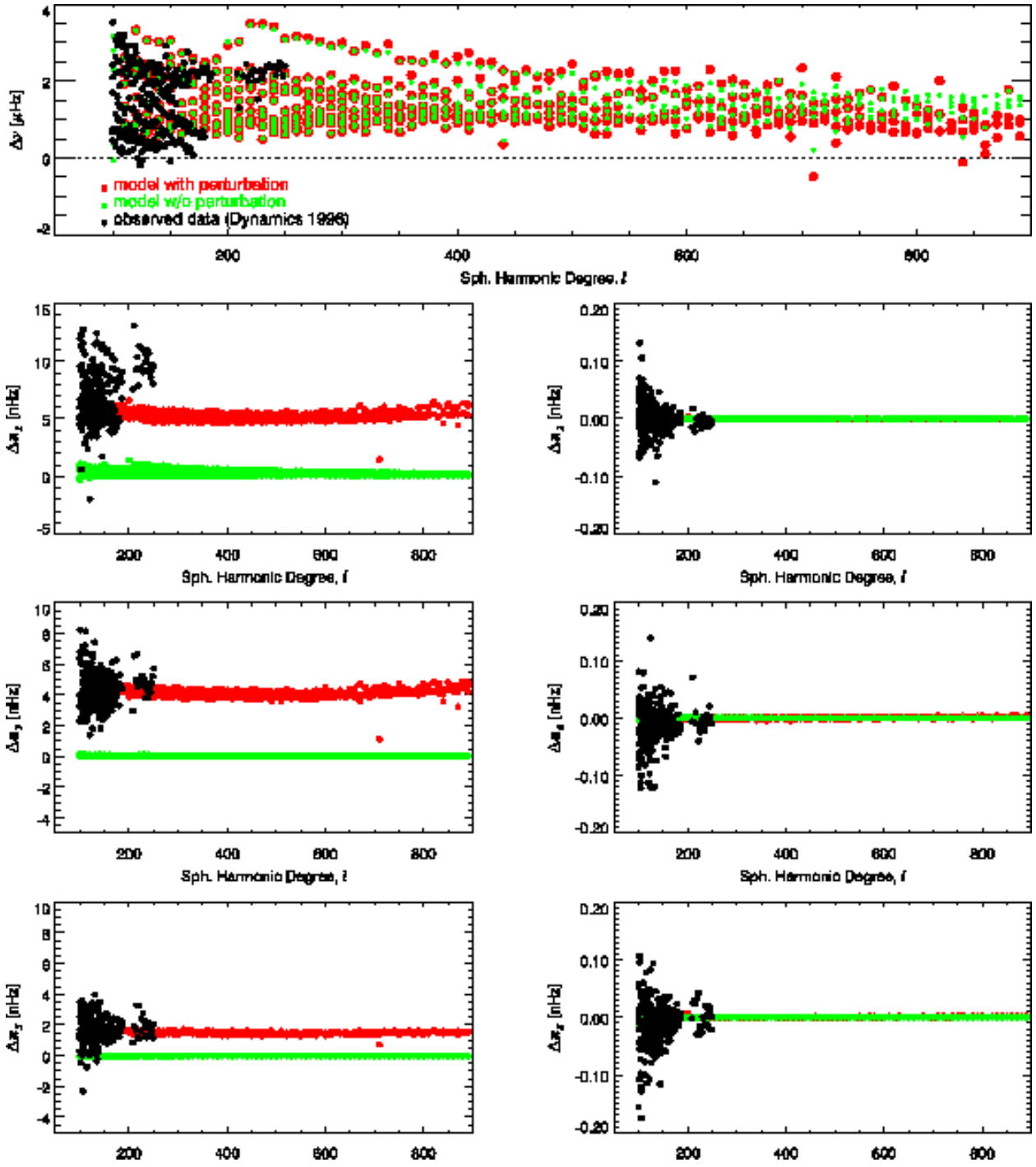

Fig. 8.— Plot similar to Fig. 7: differences between ridge and mode frequencies, but shown as a function of spherical harmonic degree, ℓ.

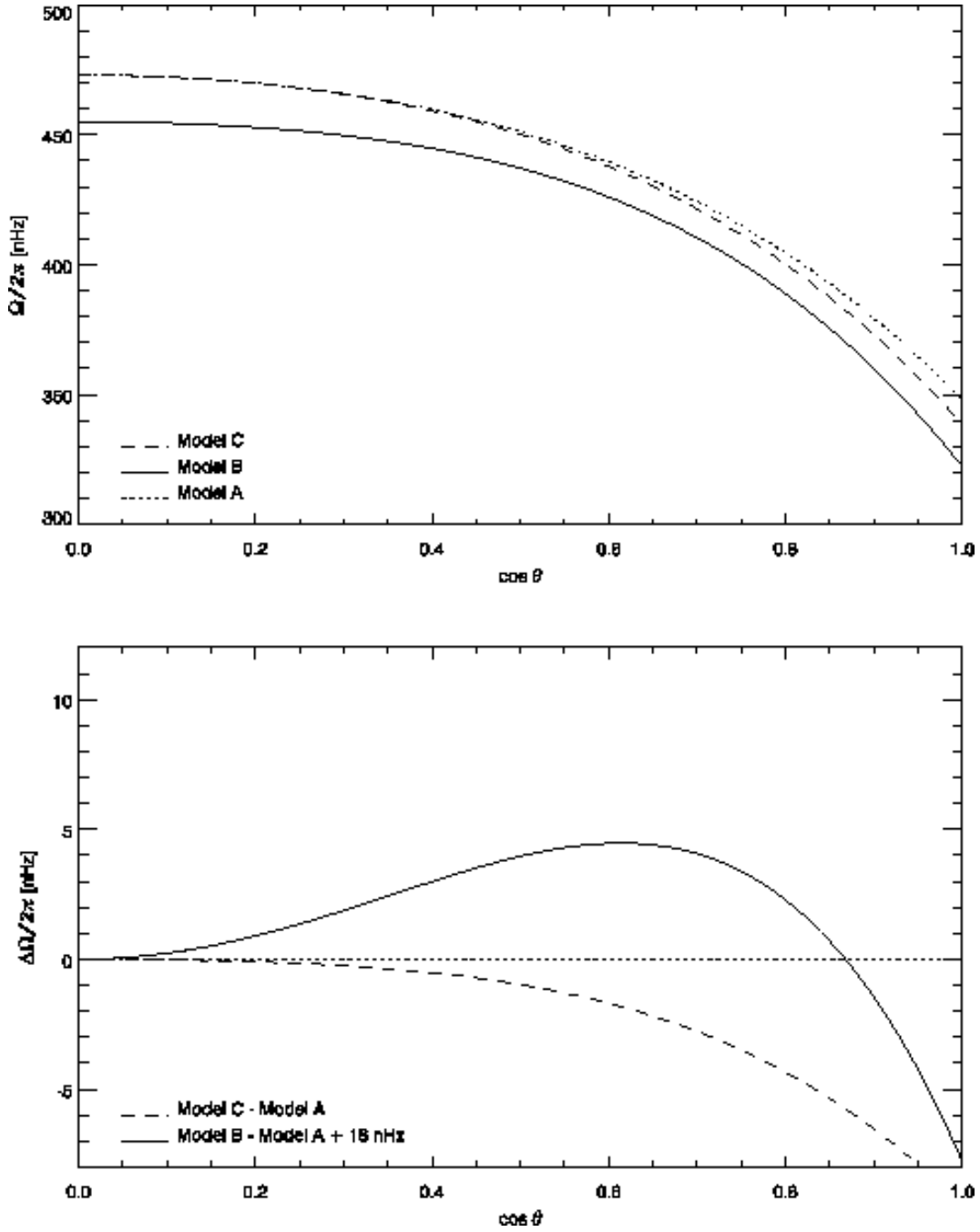

Fig. 9.— Comparison of the latitudinal dependence of three different rotation profiles at the solar surface, used to estimate the effect of the differential rotation on the distortion of the eigenfunctions. Model A corresponds to somewhat arbitrary values ($B_2 = -75$ nHz, $B_4 = -50$ nHz); Model B to values derived from Schou et al. (1998) ($B_2 = -51$ nHz, $B_4 = -81$ nHz); model C to values derived from Snodgrass & Ulrich (1990) ($B_2 = -77$ nHz, $B_4 = -57$ nHz).

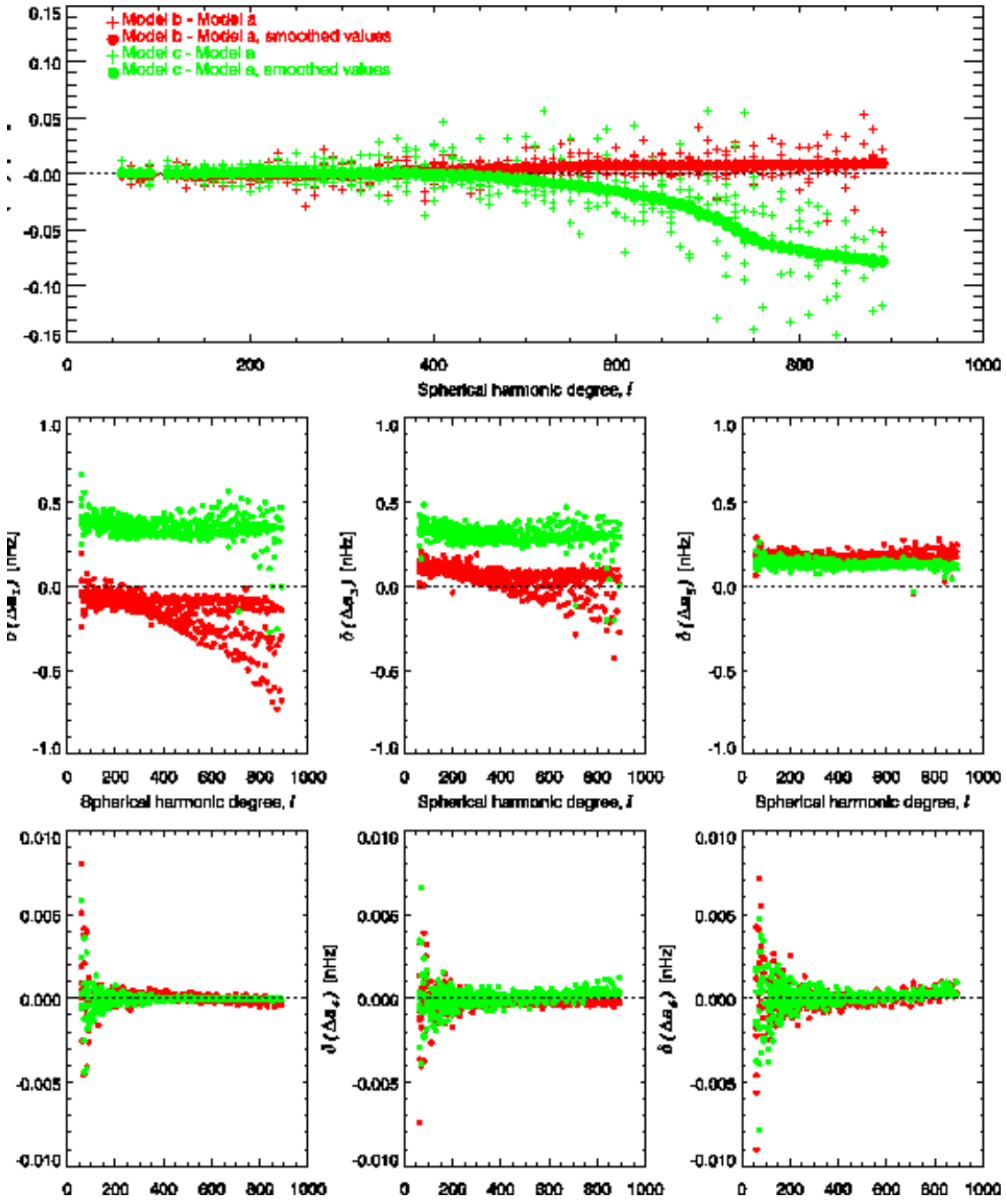

Fig. 10.— Changes in the ridge to mode frequency and splittings coefficients offsets caused by the distortion of the eigenfunctions by differential rotation, corresponding to the different rotation profiles illustrated in Figure 9.

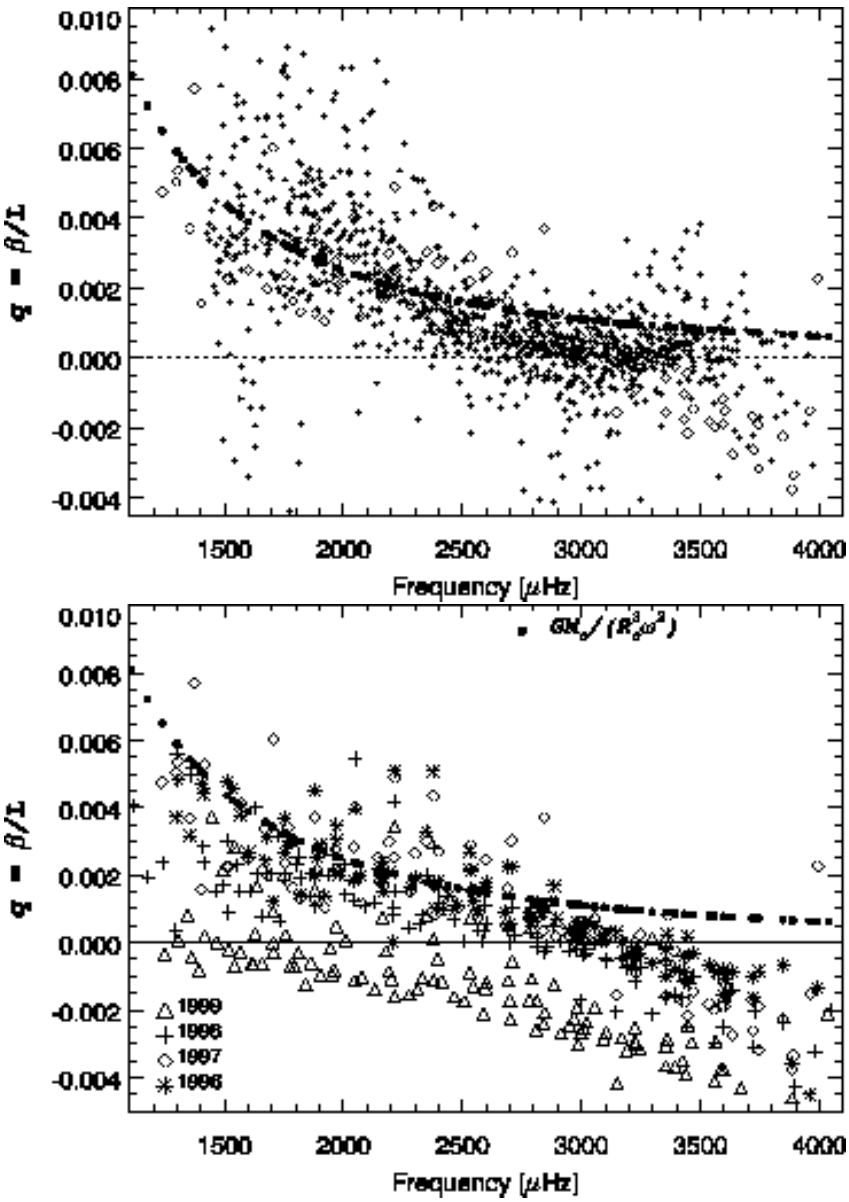

Fig. 11.— Top panel: observed $q = \tilde{\beta}/L$ estimated using the *Dynamics* 1997 data set using S_x (diamonds) or using the observed ridge frequency (crosses), see text for detailed explanations. Bottom panel: observed q for all four *Dynamics* data sets – estimated using S_x. The theoretical value of $q = G\, M_\odot/R_\odot^3\, \omega^2$ is also shown for comparison (filled dots).

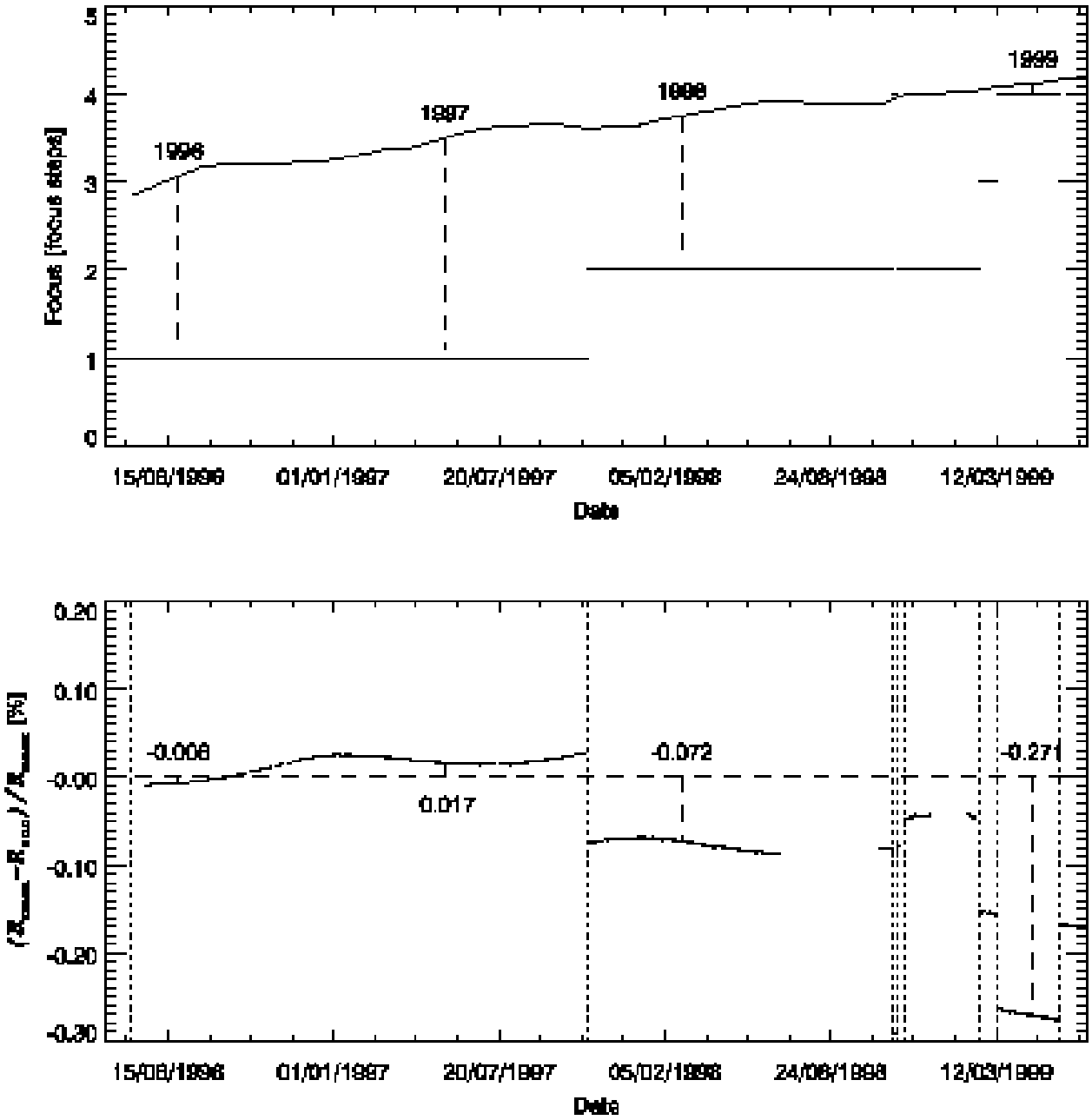

Fig. 12.— Top panel: variation of the MDI mean focus as a function of time, as computed by Bush, Chu, & Kuhn (2001). The horizontal lines indicate the focus position of the instrument at the time, and therefore the difference between the measured focus and the instrument focus position gives the amount of defocus for each *Dynamics* data set (vertical dashed lines). Bottom panel: resulting plate scale error, *i.e.*, relative difference between the observed mean solar image radius ($R_{\rm mean}$), calculated from each image using `HGEOM`, and the radius determined using the initial plate scale ($R_{\rm sun}$, see text for a more detailed description).

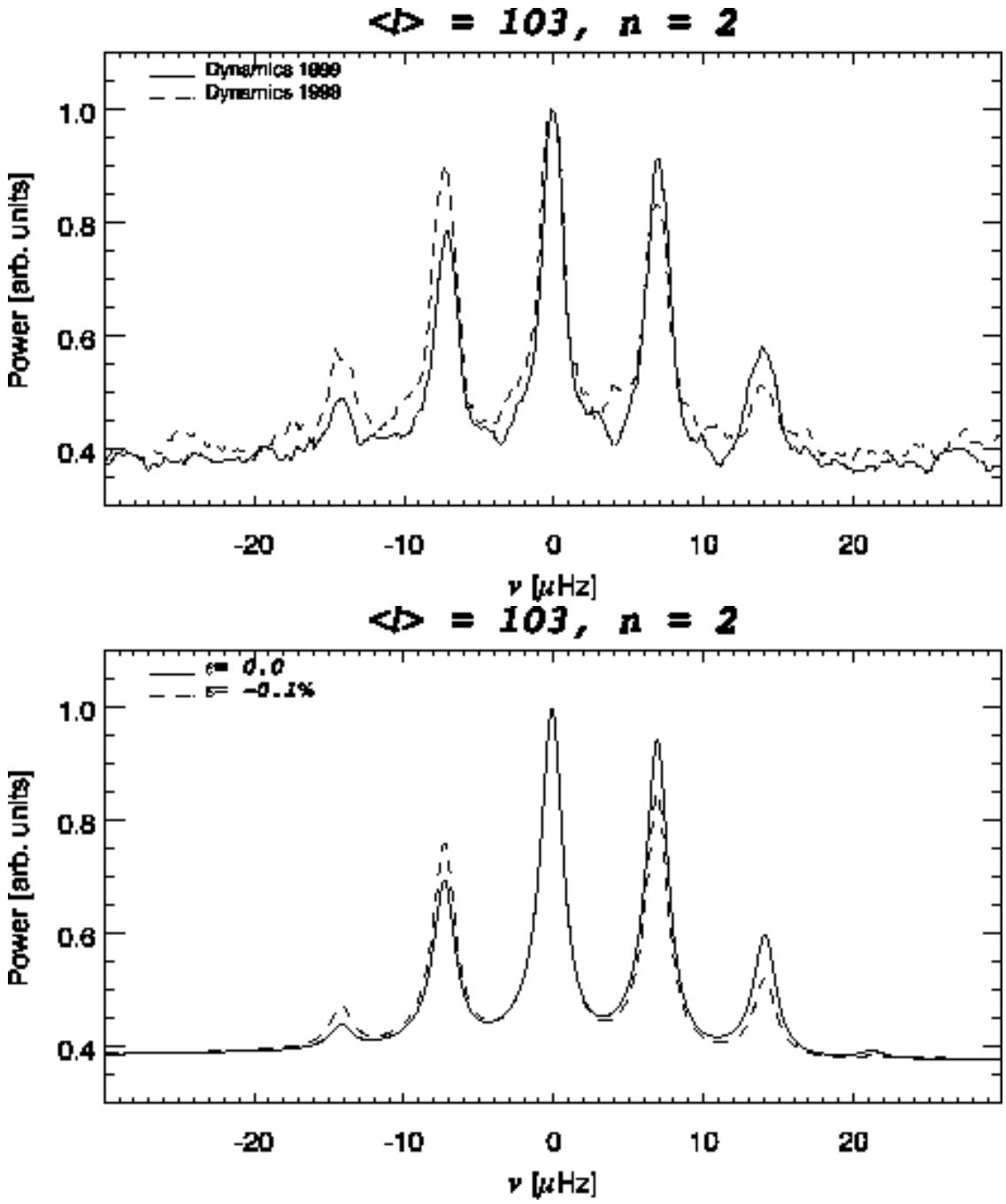

Fig. 13.— Comparison of observed and simulated sectoral limit power spectra (top and bottom panels respectively). The top panel compares *Dynamics* 1998 to 1999 spectra while the bottom panel compares synthetic spectra computed using leakage matrix without and with the inclusion of a plate scale error of -0.1% (*i.e.*, solar image radius is 0.1% larger than the one assumed in the spatial decomposition).

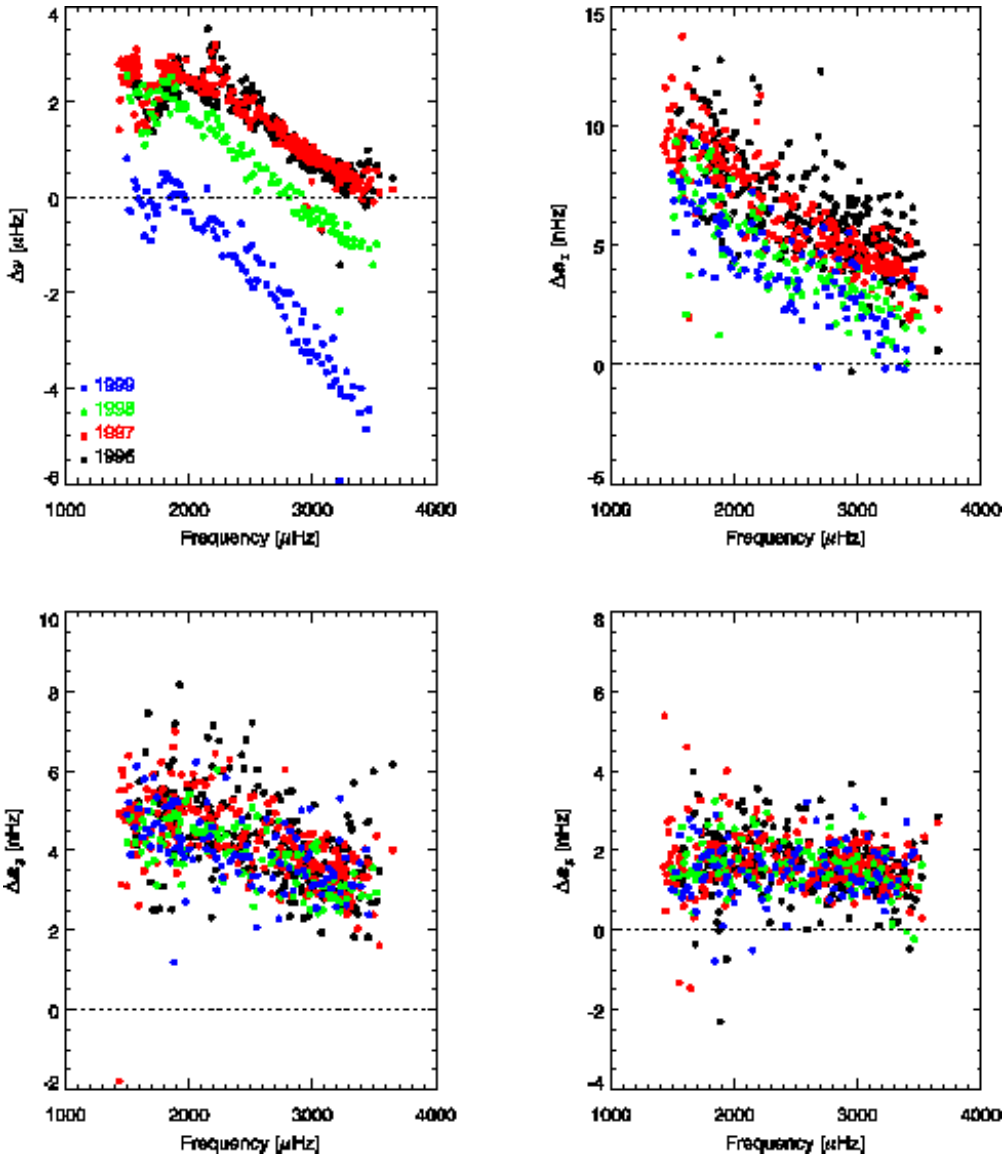

Fig. 14.— Comparison of the differences between ridge and mode frequencies, and differences between ridge and mode odd splitting coefficients, as a function of frequency, for all the *Dynamics* data sets.

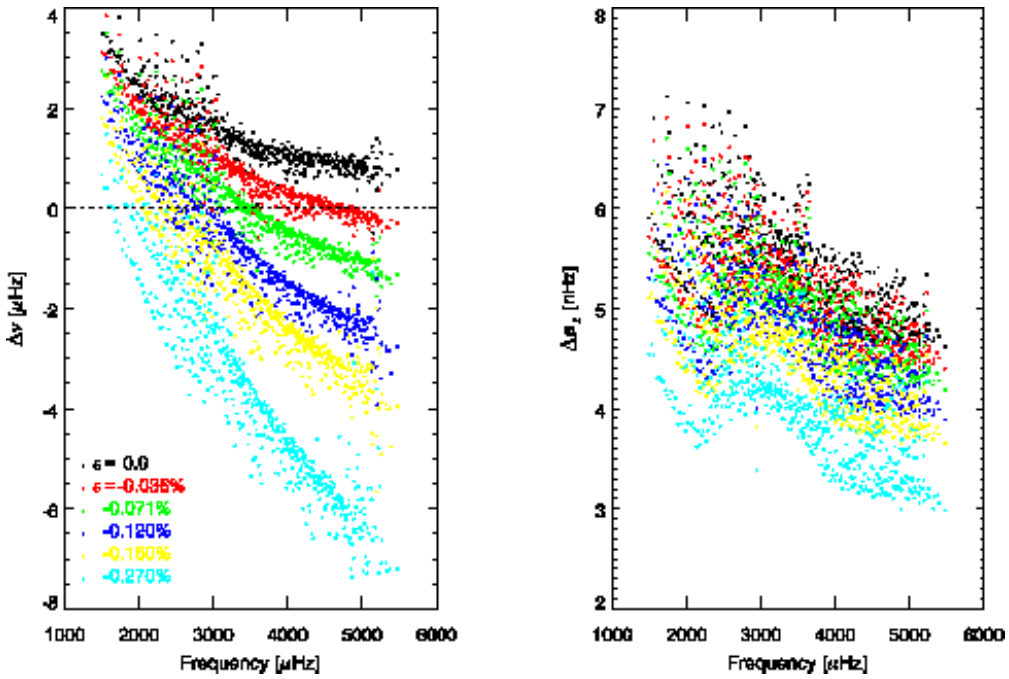

Fig. 15.— Theoretical differences between ridge and mode frequencies (left panel) and between ridge and mode a_1 splitting coefficients (right panel), shown as a function of frequency, resulting from fitting synthetic spectra computed with leakage matrices with various plate scale errors ($\epsilon = 0, 0.036, 0.071, 0.120, 0.160$ and 0.270%).

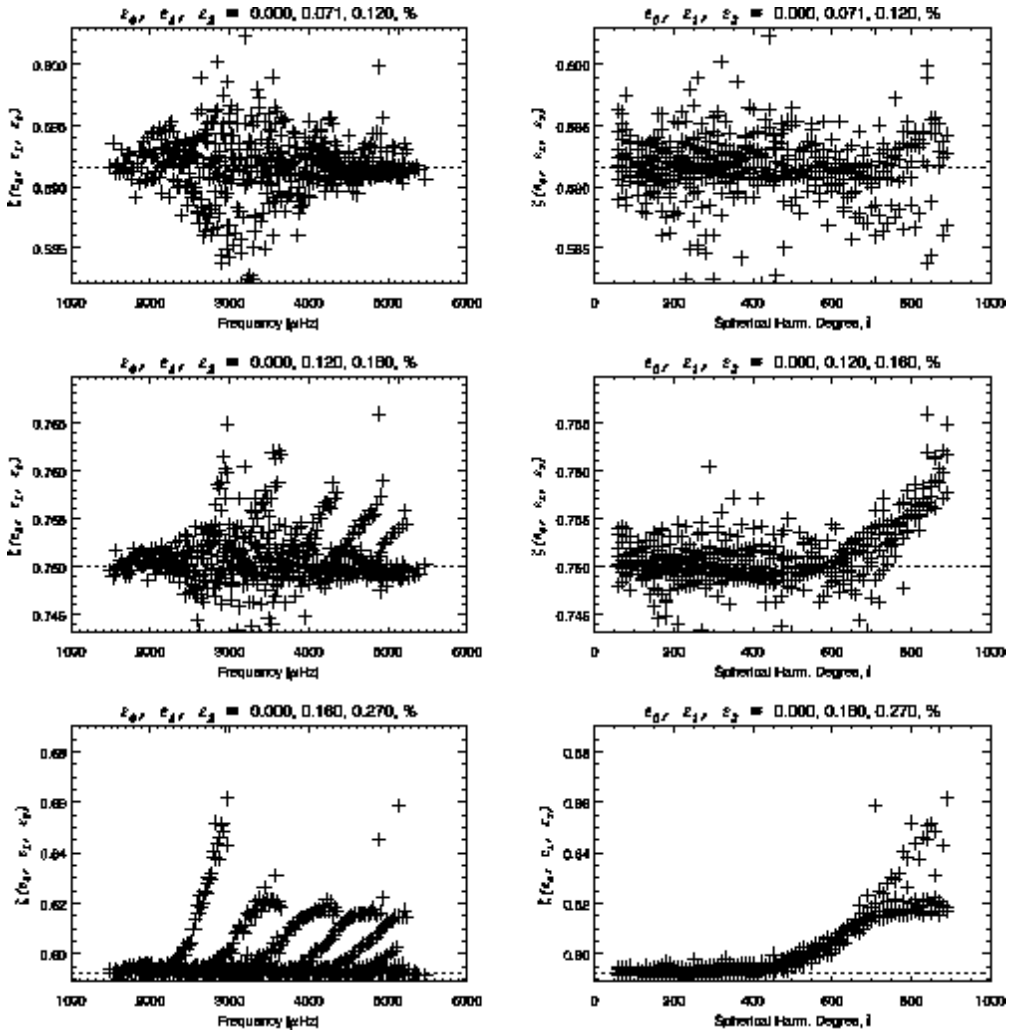

Fig. 16.— Relation $\zeta(\epsilon_1, \epsilon_2, \epsilon_3)$ (see Eq. 25) that accounts for changes in the theoretical differences between ridge and mode frequencies resulting from different plate scale errors. The dotted lines indicate the value corresponding to the combination of plate scale errors given in Eq. 25. This relation is illustrated with three combination of plate scale errors to show that it breaks at large degrees for large plate scale error.

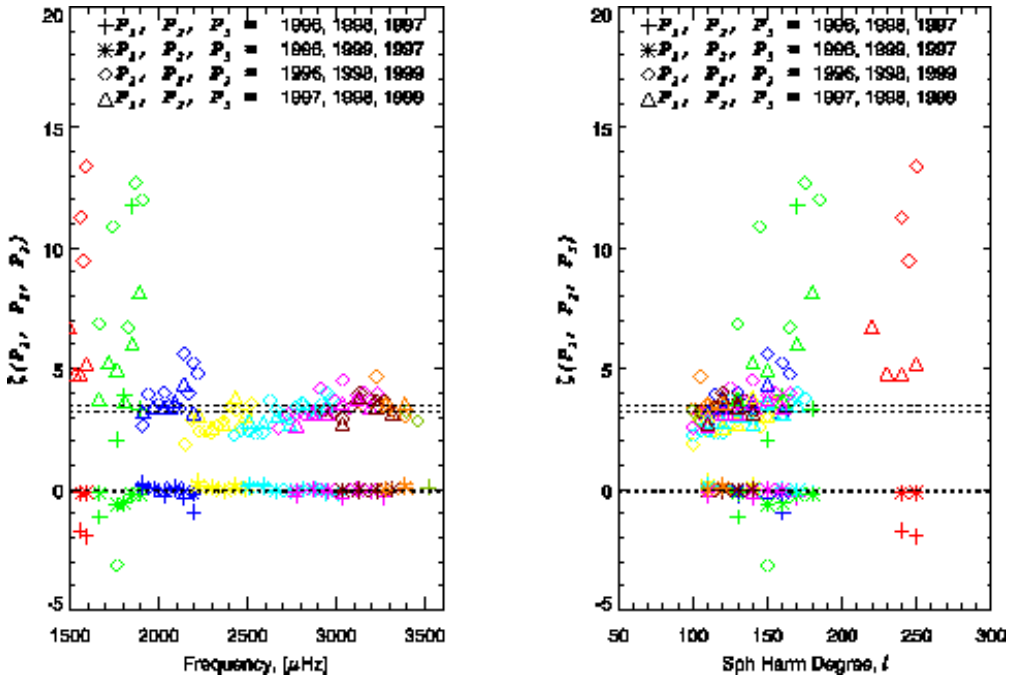

Fig. 17.— Relation $\zeta(P_1, P_2, P_3)$ (Eq. 25) for the four possible combination of *Dynamics* observations, as a function of frequency (left panel) and degree (right panel). The horizontal dash lines correspond to the expected values (see right-hand-side of Eq. 25). This confirms that the changes seen in Fig. 14 are primarily due to the change in the plate scale error.

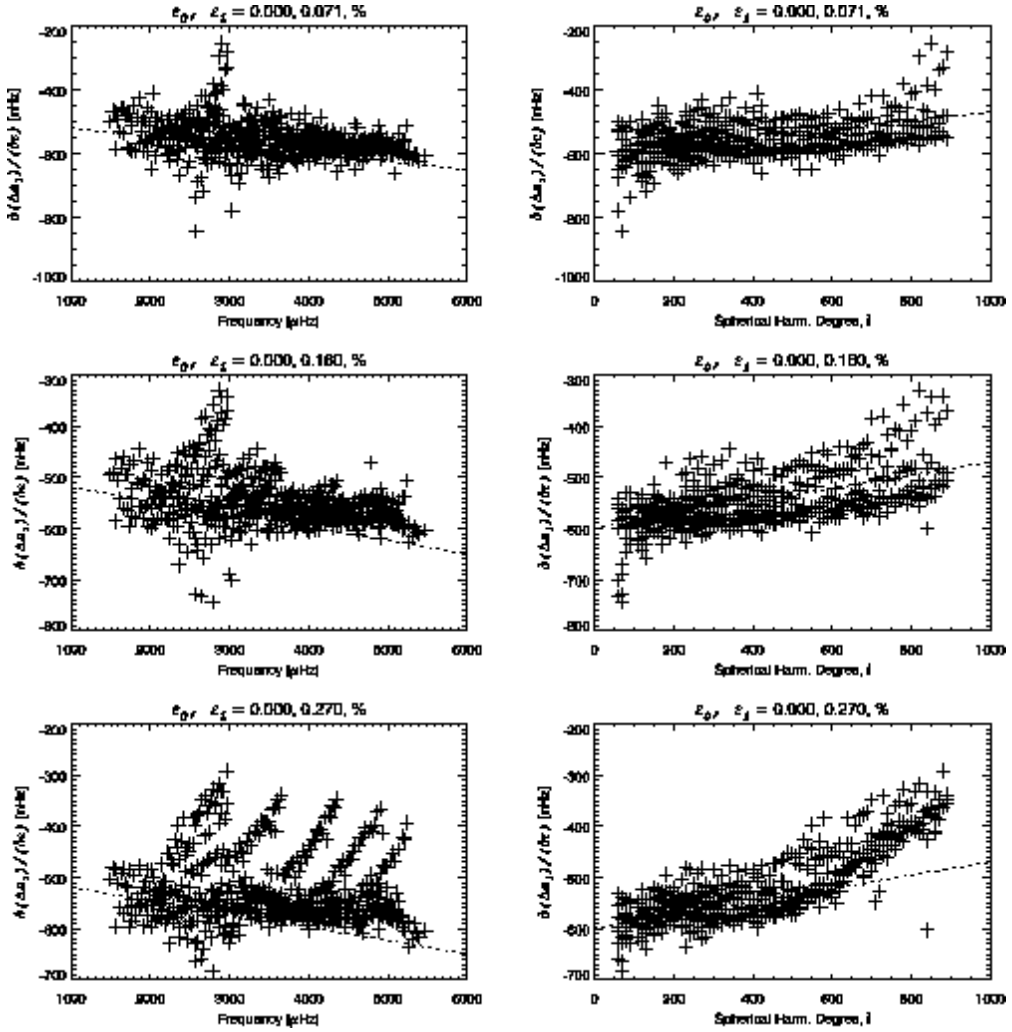

Fig. 18.— Relation between Δa_1 and ϵ_1, ϵ_2 (see Eq. 26) that expresses the changes in the theoretical differences between ridge and mode a_1 splitting coefficients resulting from different plate scale errors. The dotted lines correspond to the value predicted by Eq. 27. This relation is illustrated with three combination of plate scale errors to show that it breaks at large degrees for large plate scale error.

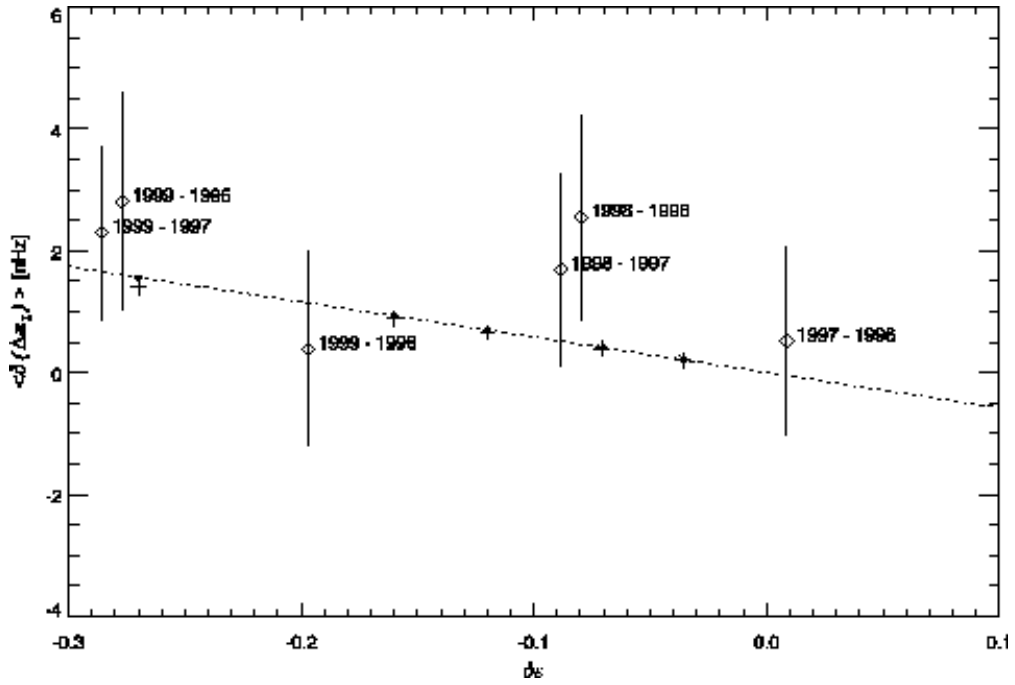

Fig. 19.— Average change in the observed differences between ridge and mode a_1 splitting coefficients (diamonds) as a function of change in plate scale errors, for all possible *Dynamics* observation combinations. The error bars correspond to the standard deviation about the mean. The crosses and stars symbols correspond to our simulations (all the modes or only the modes with degree up to 250 respectively) and the dotted line illustrates the relation expressed by Eqs 26 and 27.

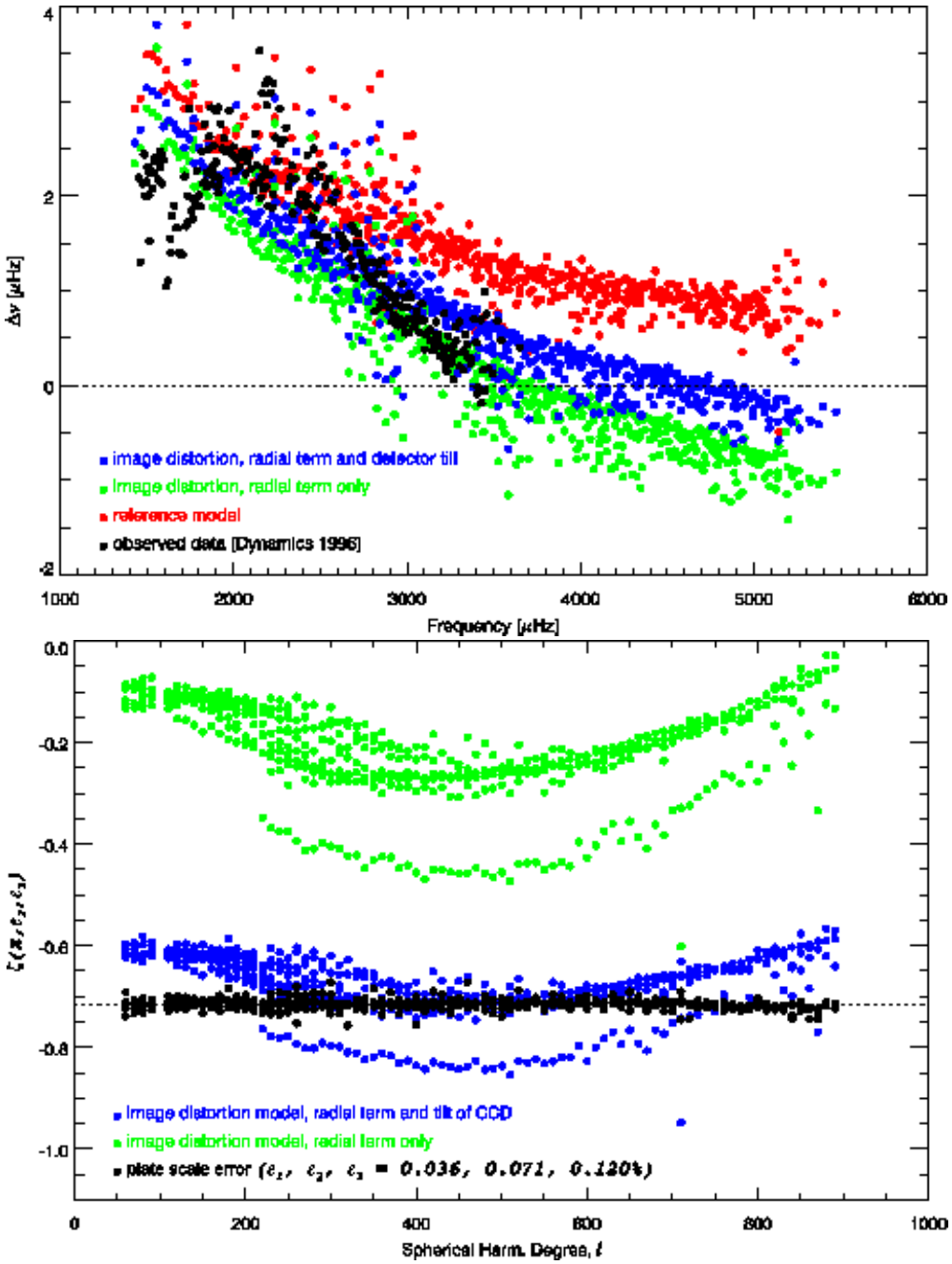

Fig. 20.— Top panel: Comparison of observed and theoretical differences between ridge and mode frequencies. The effect of including an image distortion (in green and blue) in the leakage matrix is compared to our reference model (in red) and to the observations (in black). The bottom panel shows that the effect of the image distortion is different from an image scale error: the relation expressed by Eq 25 is not satisfied.

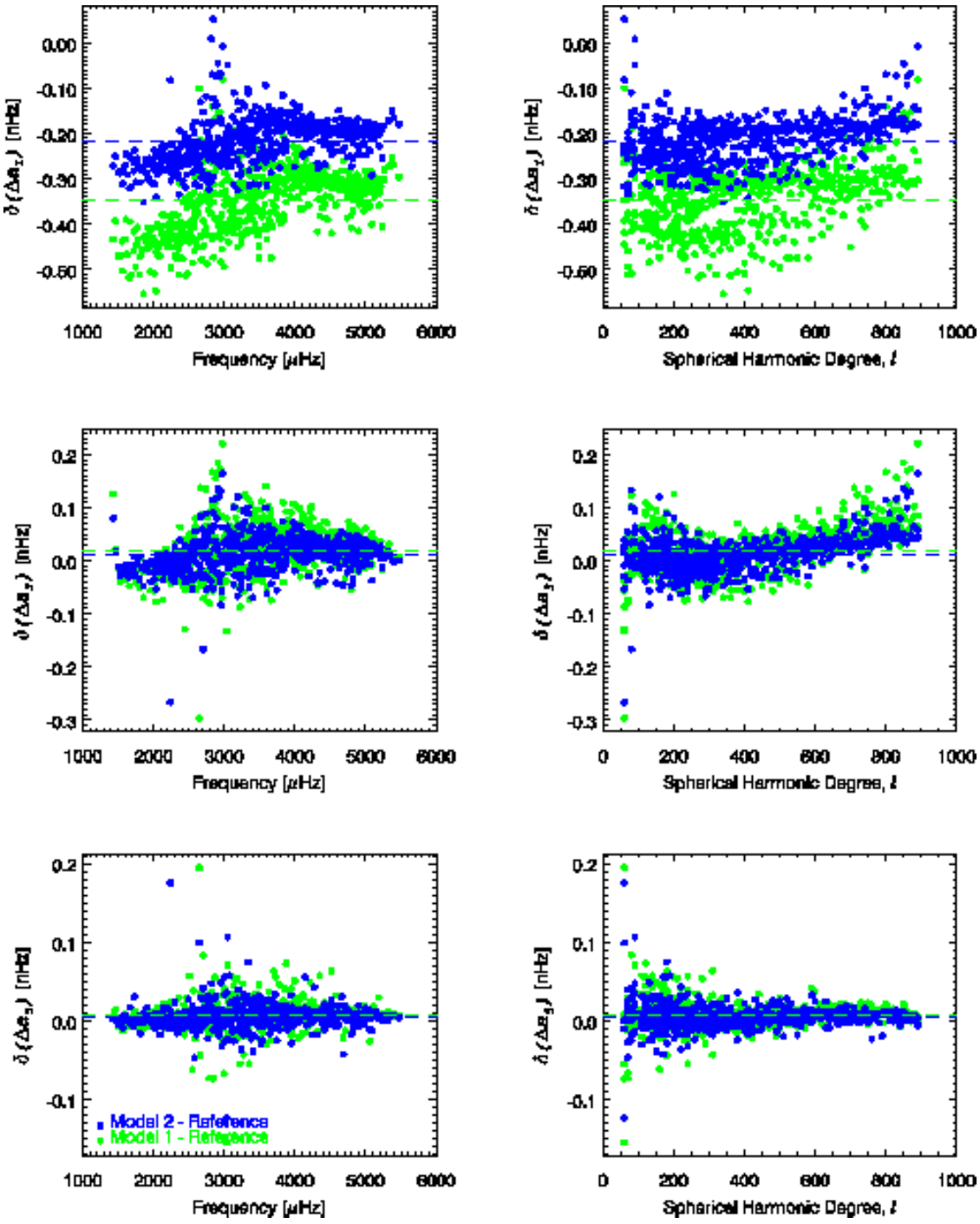

Fig. 21.— Changes in odd splitting coefficients offsets for two image distortion models with respect to our reference model. Model 1 includes only a radial image distortion (green points), Model 2 includes both the radial term and the tilt of the CCD (blue points). Horizontal lines are the respective means.

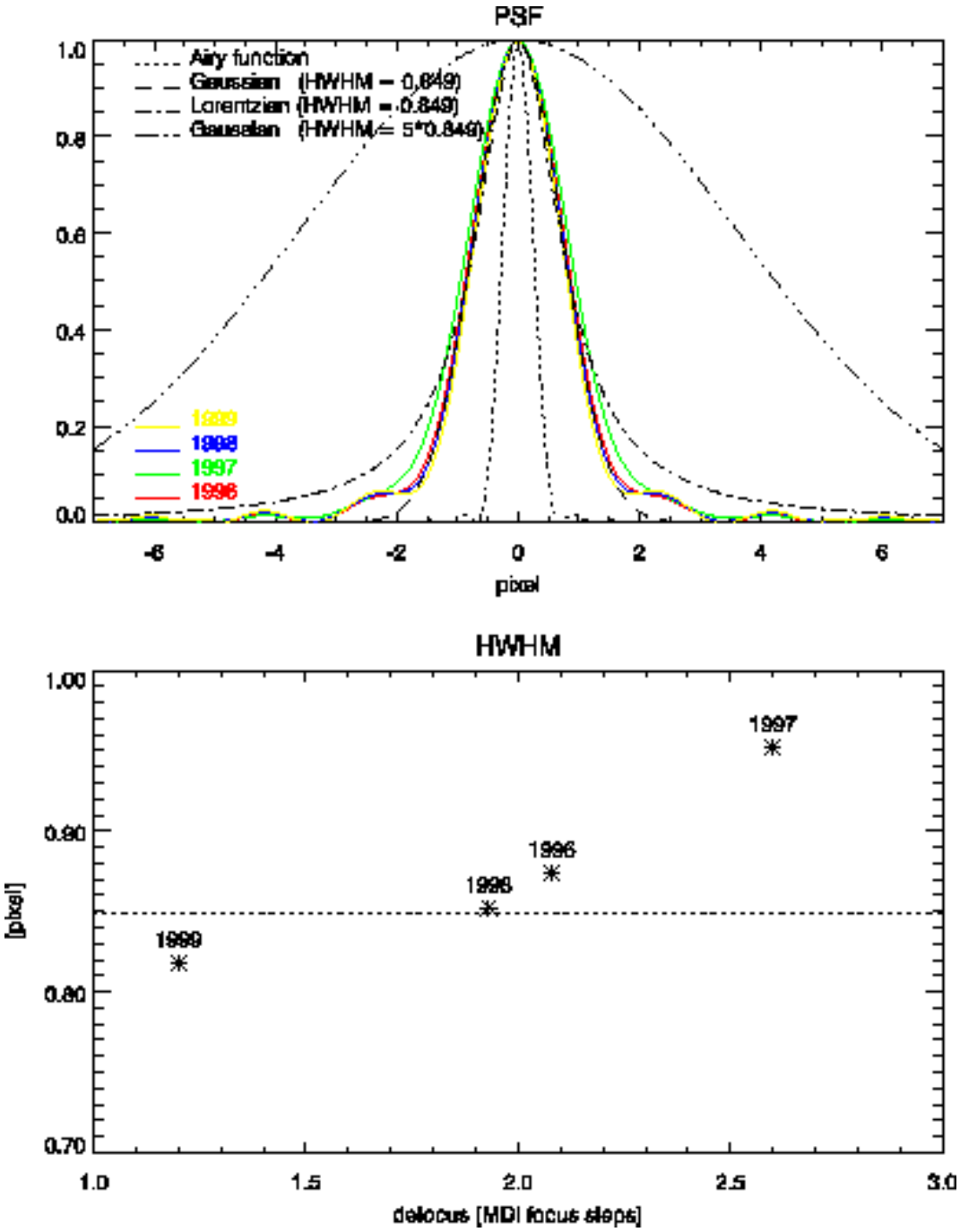

Fig. 22.— Top panel: estimates of MDI azimuthally averaged point spread function (PSF), computed from four images corresponding to each consecutive year of the *Dynamics* program. These are compared to the Airy function corresponding to the instrument aperture diffraction limit and to a Gaussian and a Lorentzian with a matching half width at half maximum (HWHM). Bottom panel: HWHM of the azimuthally averaged point spread functions as a function of image defocus.

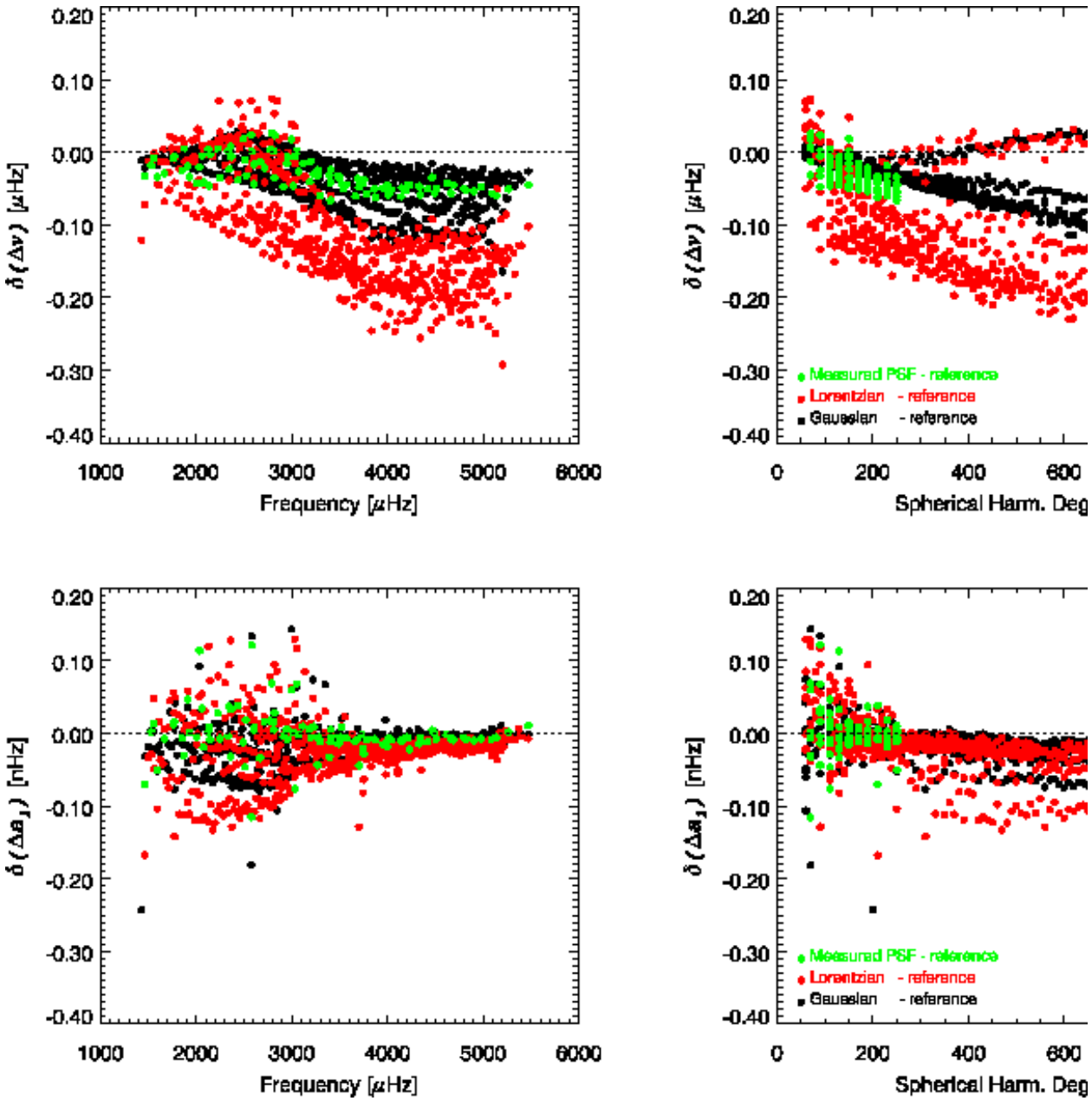

Fig. 23.— Change in the theoretical differences between ridge and mode frequency (top panels) and and between ridge and mode a_1 splitting coefficient (bottom panels), with respect to a reference case, as a function of frequency (left panels) or degree (right panels). The reference case uses a leakage matrix computation that does not include the effect of the instrumental PSF. This is compared to the cases where the leakage matrix computation includes a) a Gaussian PSF (HWHM = 0.71 pixel, black points), b) a Lorentzian PSF (HWHM = 1.0 pixel, red points), or c) the PSF estimated by `HGEOM` using a *Dynamics* 1996 image (green points). These changes are on the order of 10% for the frequency differences and 2% for the a_1 coefficient differences.

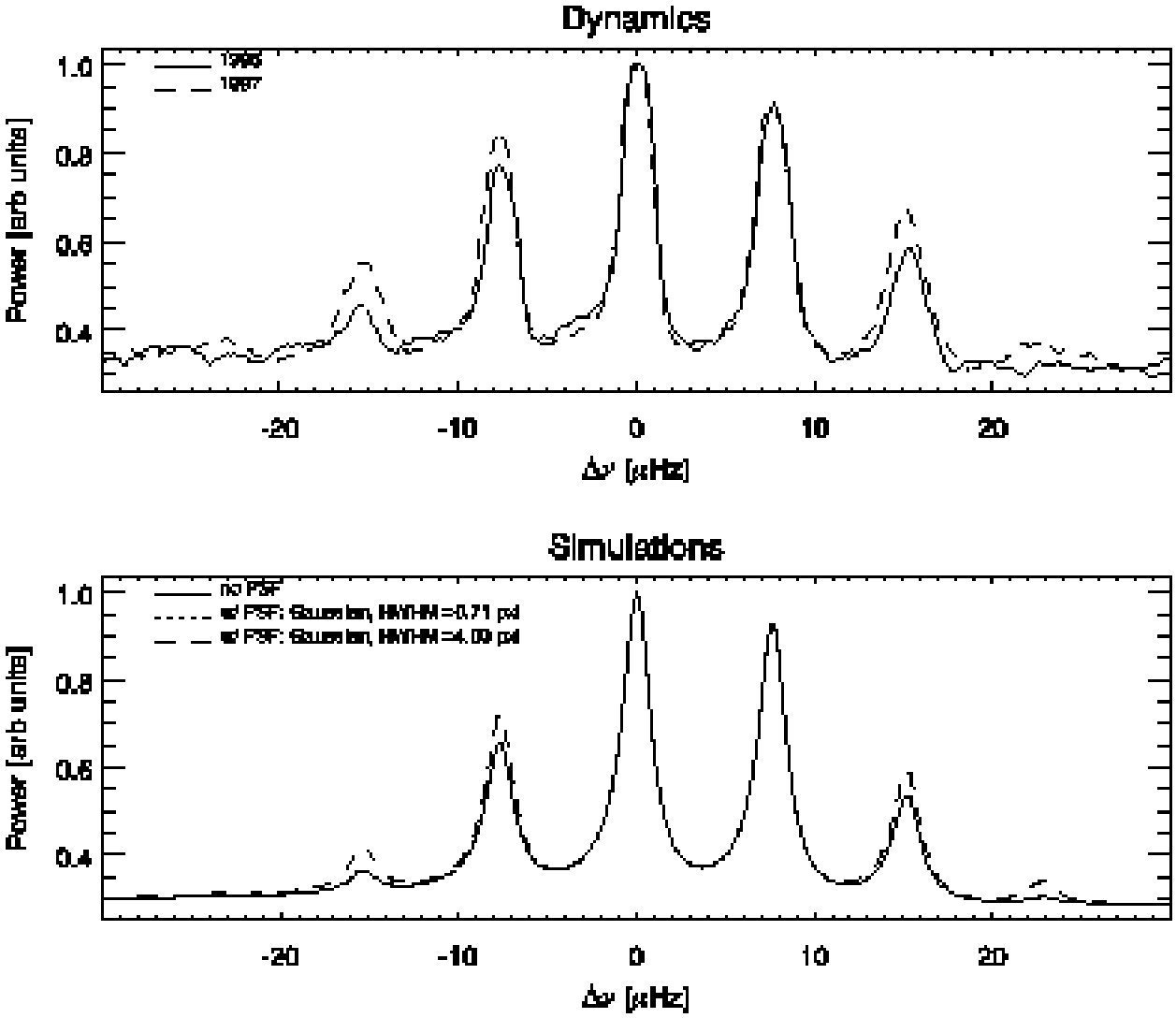

Fig. 24.— Observed (top panel) and synthetic (middle panel) sectoral limit power spectra for $n = 2$ and $\ell = 92$. The observed spectra correspond to the two consecutive years with the largest change in PSF width (see Fig 22), that might account for the observed change in leaks amplitude. The three synthetic spectra correspond to leakage matrices computed using no PSF, a Gaussian PSF with a HWHM of 0.71 pixel (a good approximation of the measured azimuthally averaged PSF) and a Gaussian PSF with a HWHM of 4.0 pixel (a substantially wider PSF). Only when very wide PSF is included does our simulations produce a noticeable change in the amplitude of the leaks.

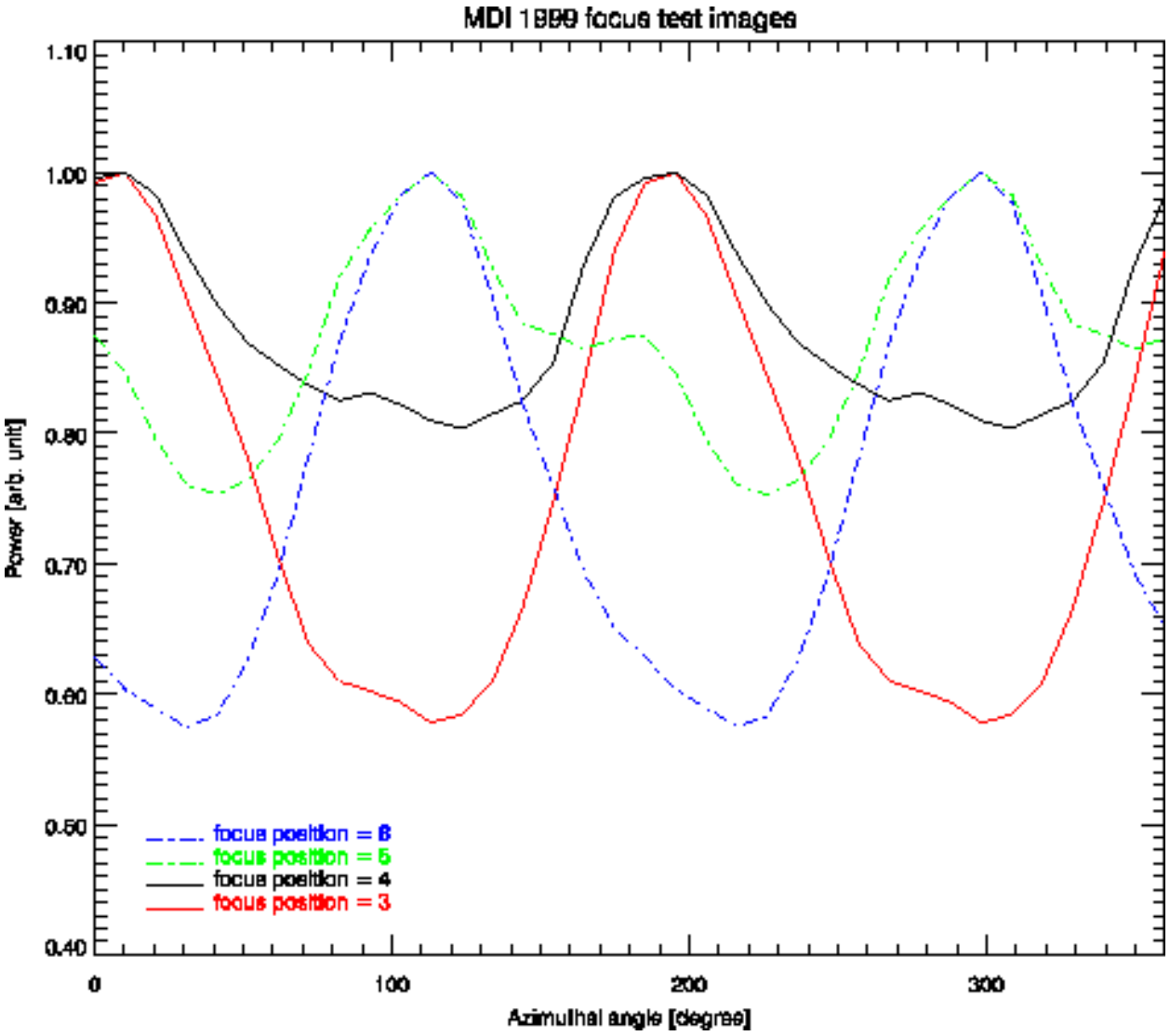

Fig. 25.— Observed power spectra as a function of azimuthal angle for a horizontal wave number, k_h, of 230 pixel^{-1}, computed from 1999 MDI images taken at four different focus positions, *i.e.* focus steps 3, 4, 5 and 6. The best focus position at the time was determined to be at focus step 4.1 (see Fig 12). The angular dependence of these power spectra indicates that the instrumental PSF is not uniform with respect to the azimuthal orientation on the detector. Note how the non-uniformity increases with increasing defocus and the phase shift of the azimuthal dependence between either side of the best focus position.

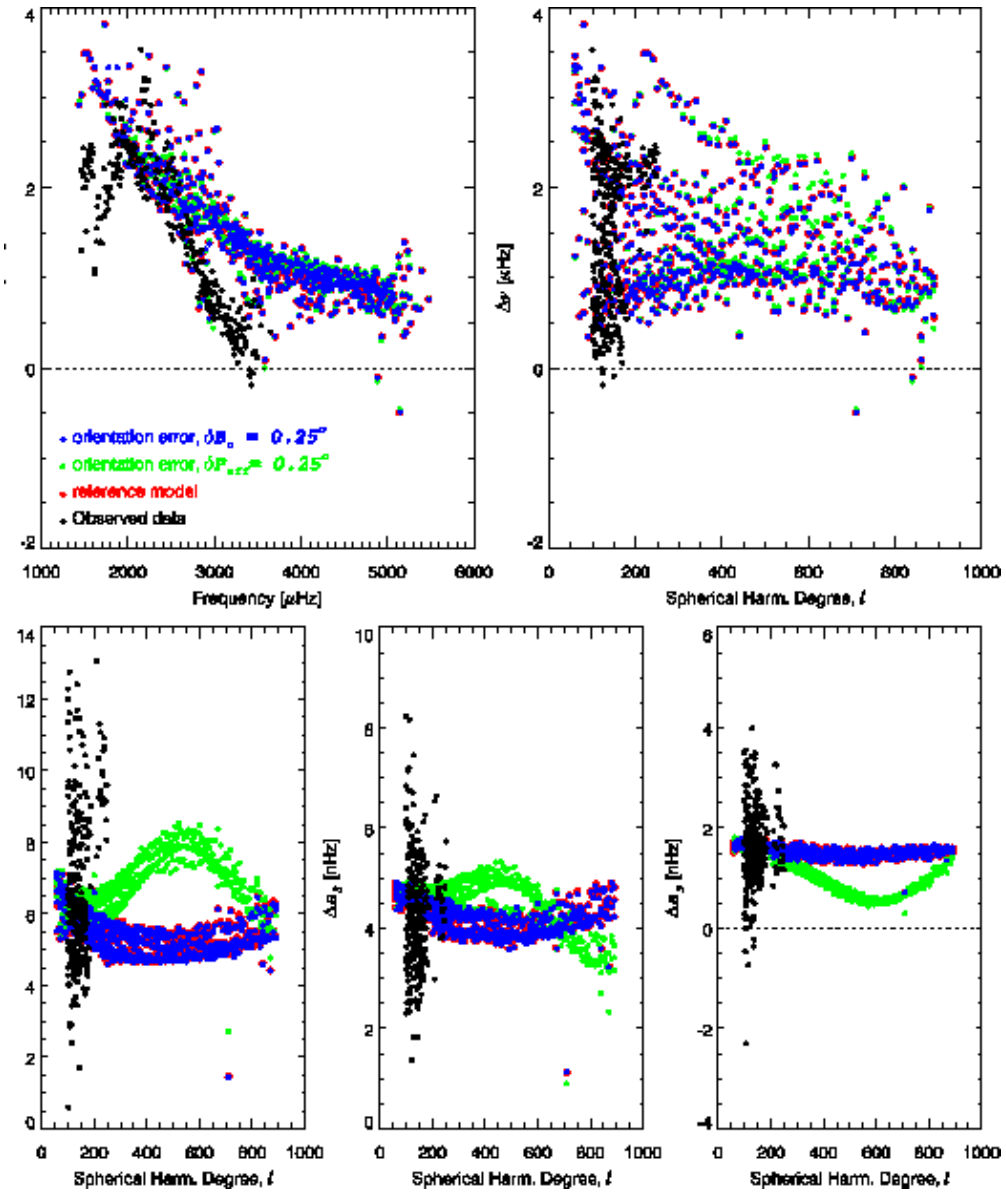

Fig. 26.— Comparison of observed and theoretical differences between ridge and mode frequencies and between ridge and mode odd splitting coefficients. The effect of including an error in the solar rotation axis orientation in the computation of the leakage matrix ($\delta P_{\rm eff} = 0.25°$, in green, and $\delta B_{\rm o} = 0.25°$, in blue) is compared to our reference model (in red) and to the observations (*Dynamics* 1996, in black).

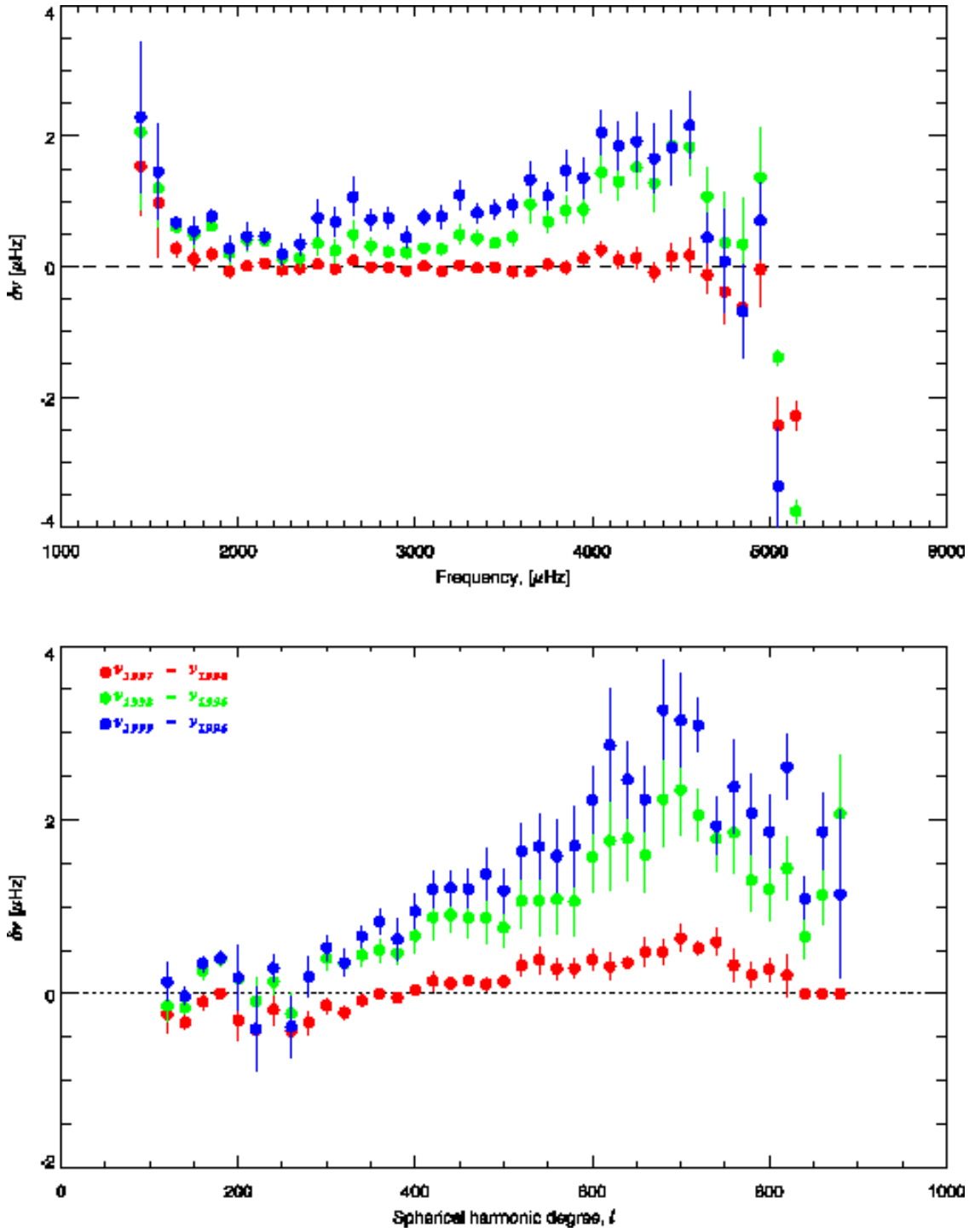

Fig. 27.— Binned frequency changes with respect to values for 1996, after correction for respective plate scale errors. The differences were averaged over bins 100 μHz wide in frequency (top panel) and 20 degree wide (bottom panel); the error bars represent the standard deviation of the mean.

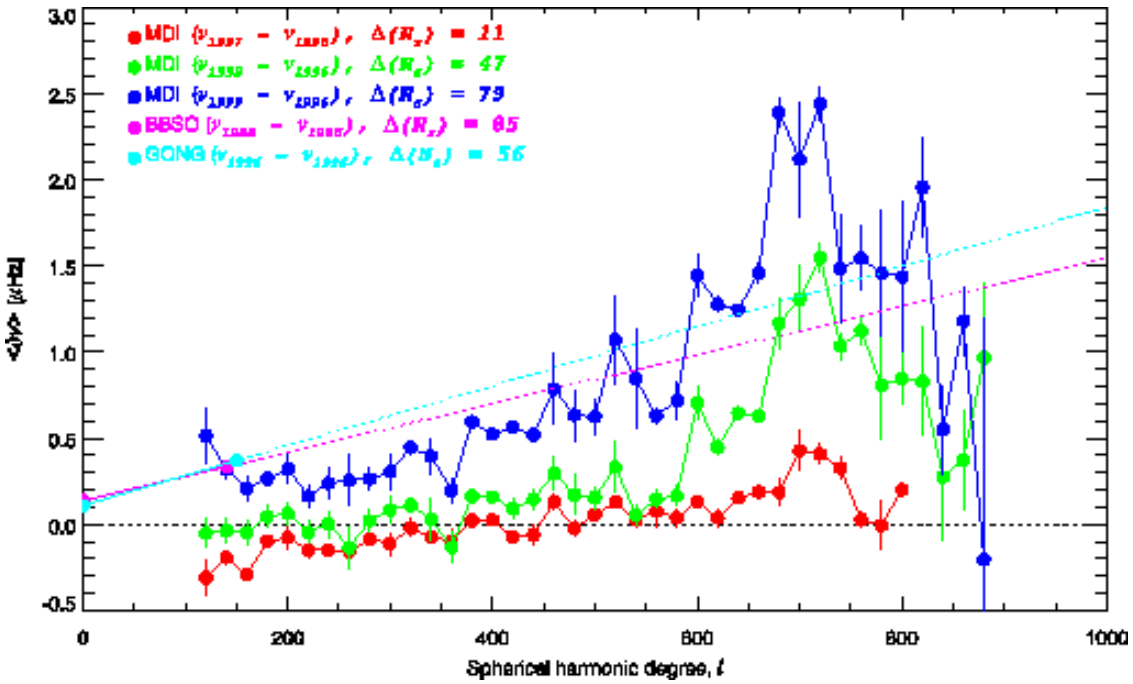

Fig. 28.— Mean frequency changes around 3 mHz (*i.e.*, the frequency change averaged over the 2.6 to 3.4 mHz frequency range) – with respect to 1996 values – as a function of degree. These values are compared to linear extrapolations of comparable determinations based on Big Bear Solar Observatory observations taken between 1986 and 1988 (Libbrecht & Woodard 1990) and on GONG observations taken between March 1996 and July 1998 (Howe, Komm & Hill 1999).

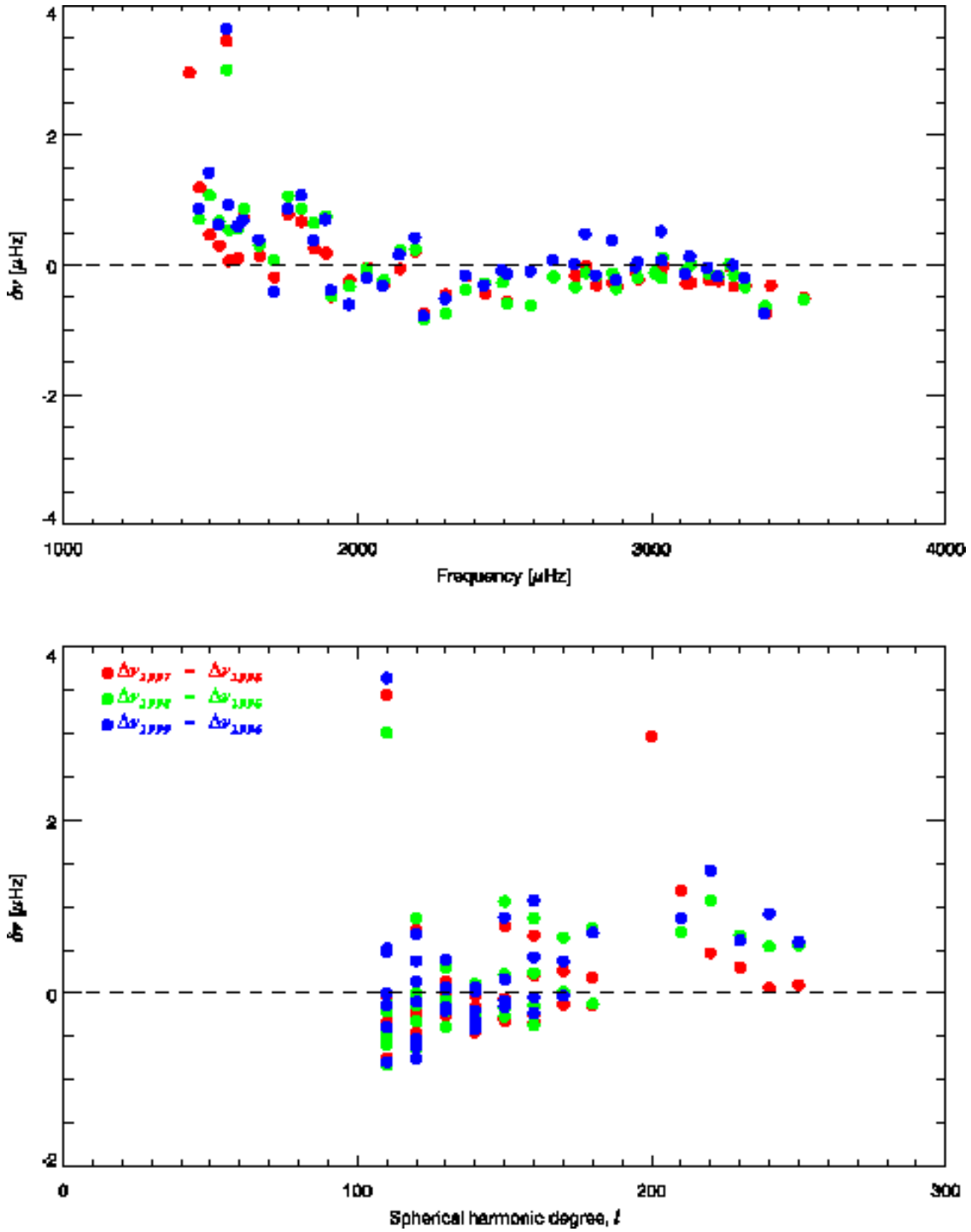

Fig. 29.— Residual frequency offsets with respect to values for 1996, as a function of frequency and degree.

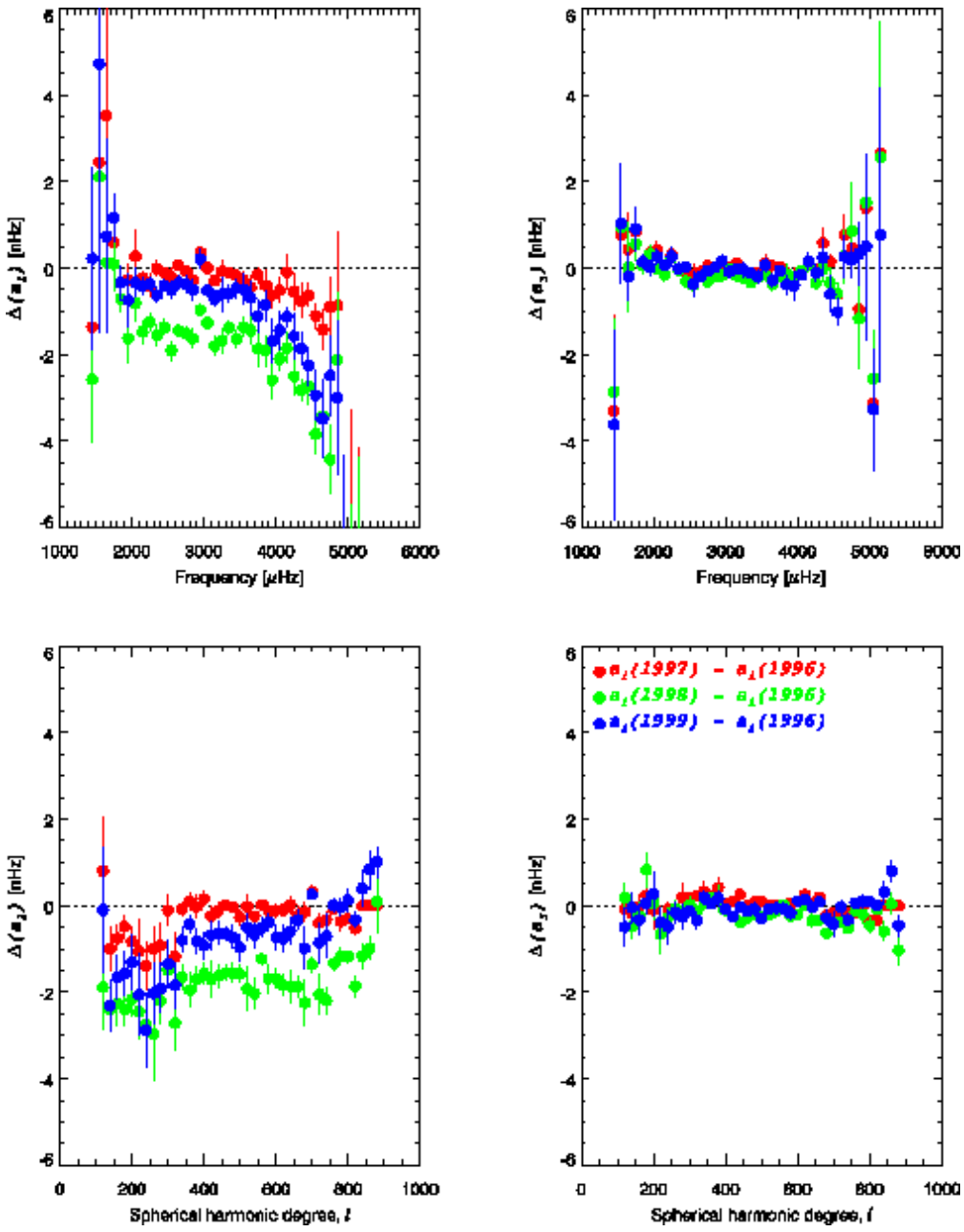

Fig. 30.— Changes in a_1 and a_3 splitting coefficients – relative to values for 1996 – for different epochs, as a function of frequency and degree, after correction for respective plate scale errors. The changes were averaged over bins 100 μHz wide in frequency (top panel) and 20 degree wide (bottom panel); the error bars represent the standard deviation of the mean.

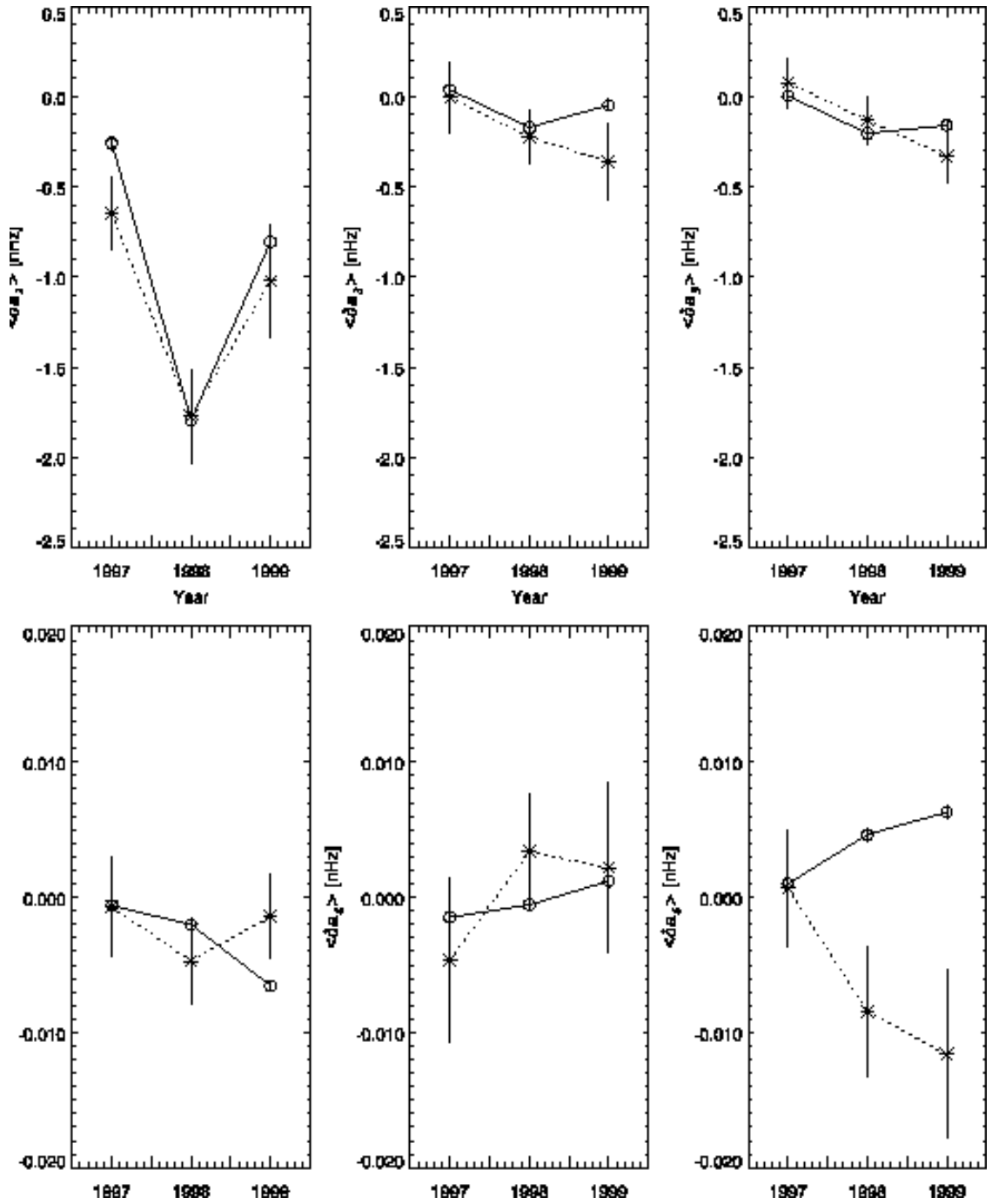

Fig. 31.— Mean changes in odd and even splitting coefficients with epoch (circles) compared to mean changes in residual offsets (stars, see text). Since both sets track each other (except for a_6), we are led to conclude that the changes are due to systematic errors.

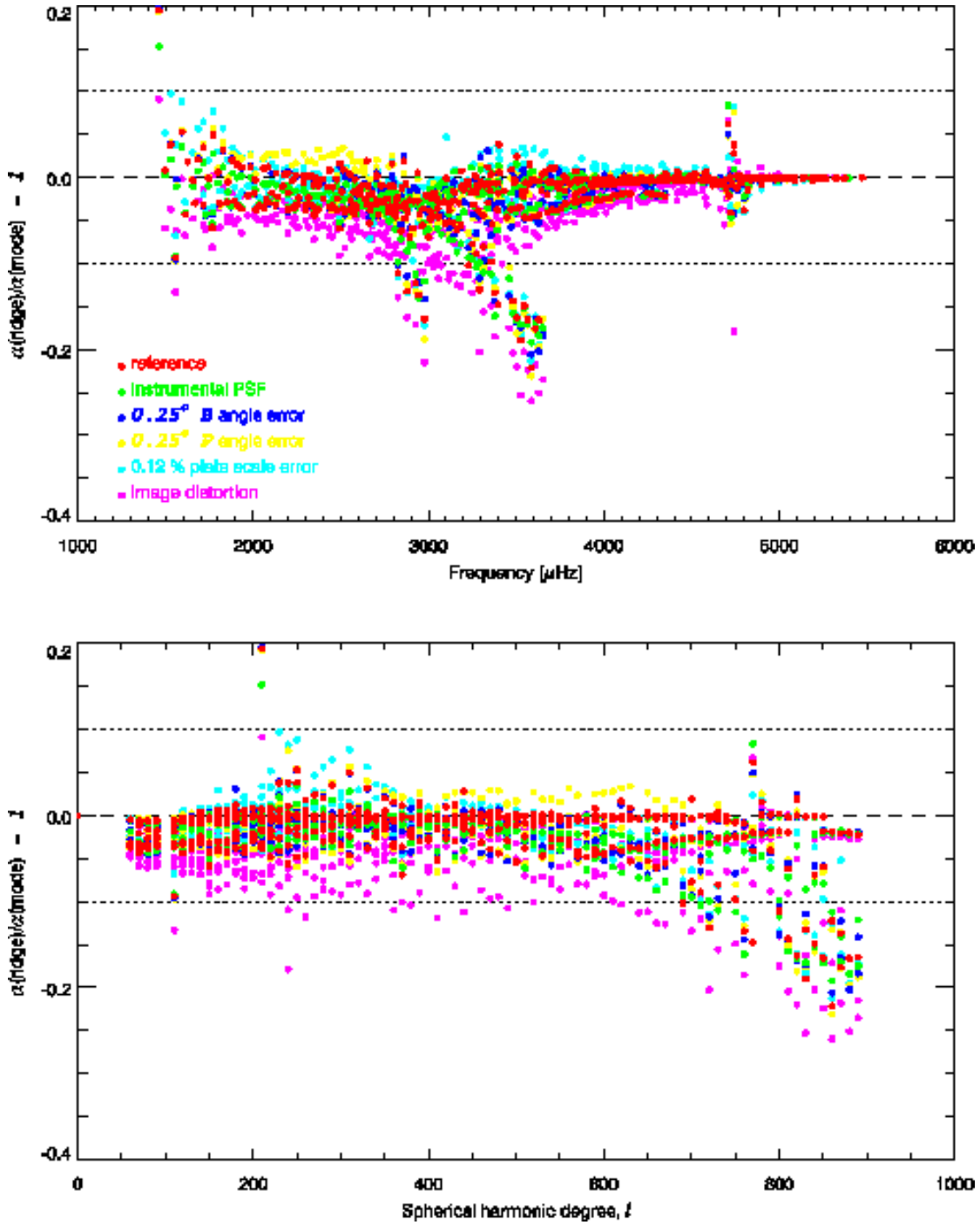

Fig. 32.— Comparison of the ridge asymmetry resulting from fitting synthesized ridges with the mode asymmetry used as input. The different colors represent results for different simulations. Up to $\ell = 700$ the ridge asymmetry is within 10% of the mode value. The large excursions are for low order modes (*i.e.*, for $n = 0$ and 1). Also, the feature at $\nu = 4.7$ mHz occurs where the asymmetry goes through zero.

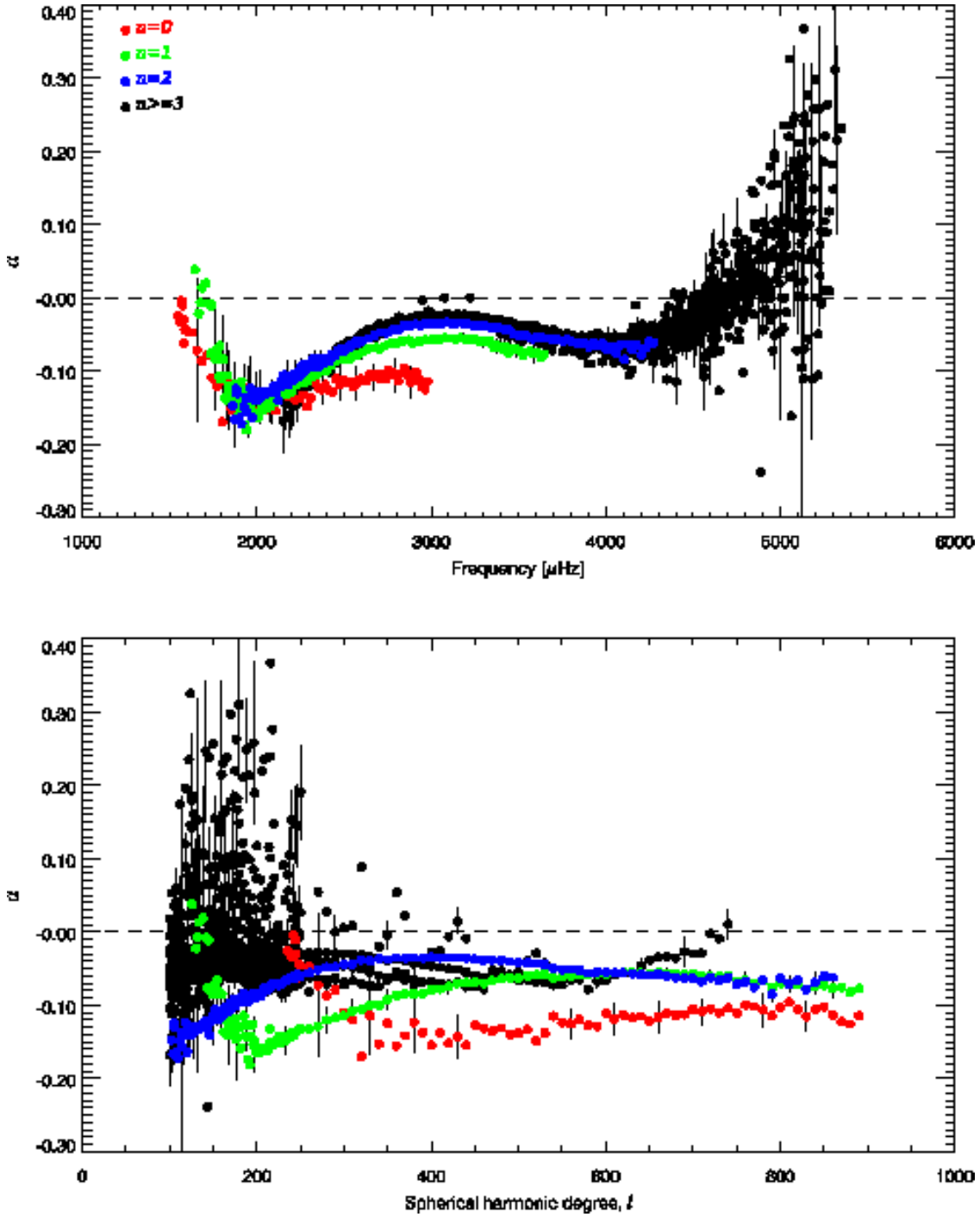

Fig. 33.— Ridge asymmetry for the 1996 *Dynamics* epoch, as a function of frequency and degree. Error bars are shown only for every 5th data point, the low order modes are color coded.

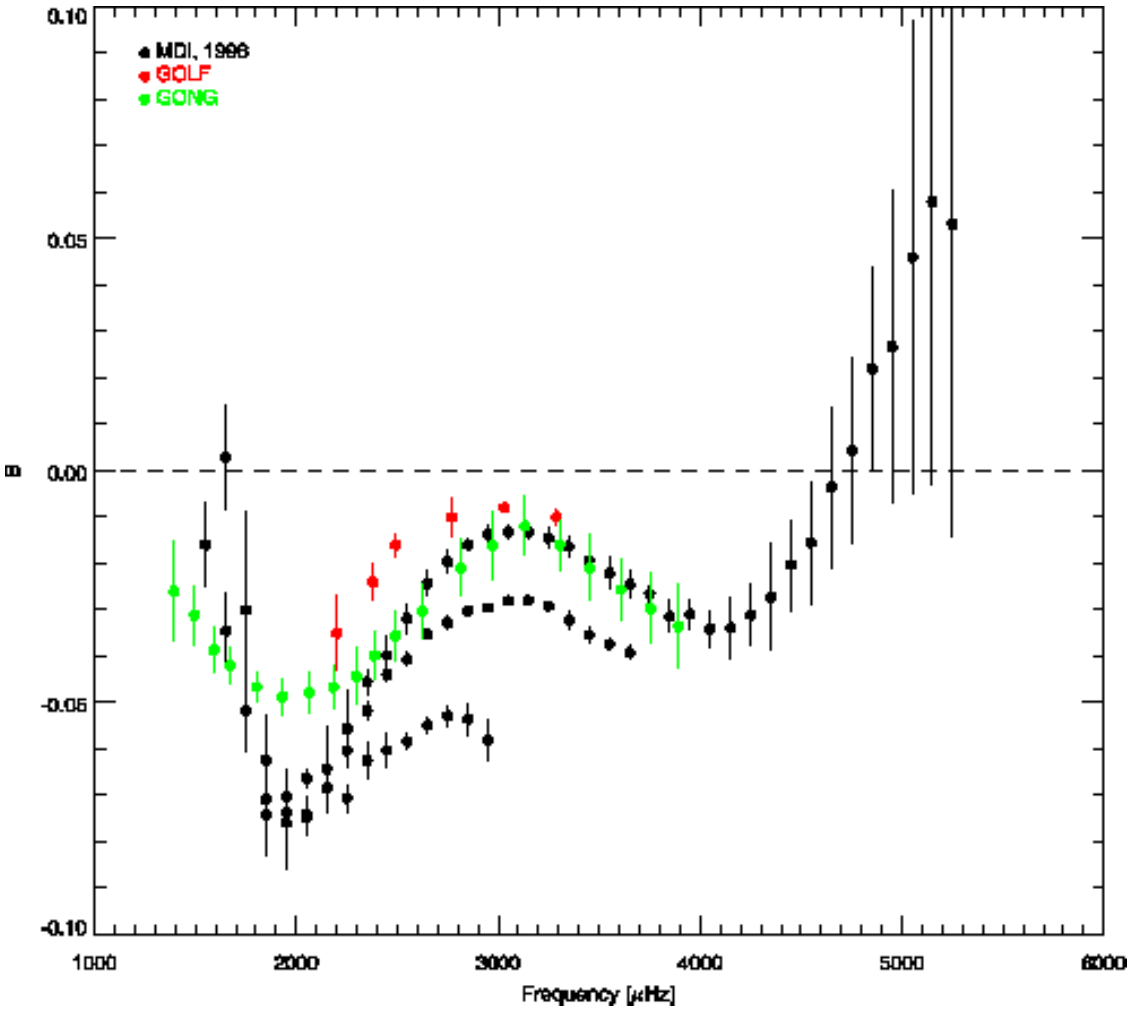

Fig. 34.— Comparison of the profile asymmetry estimates from 1996 MDI *Dynamics* data (this work) with published values from GOLF and GONG observations. The MDI data were binned in frequency for $n = 0, 1$ and $n \geq 2$ separately. The error bars for the MDI and GONG values represent the scatter of the data.

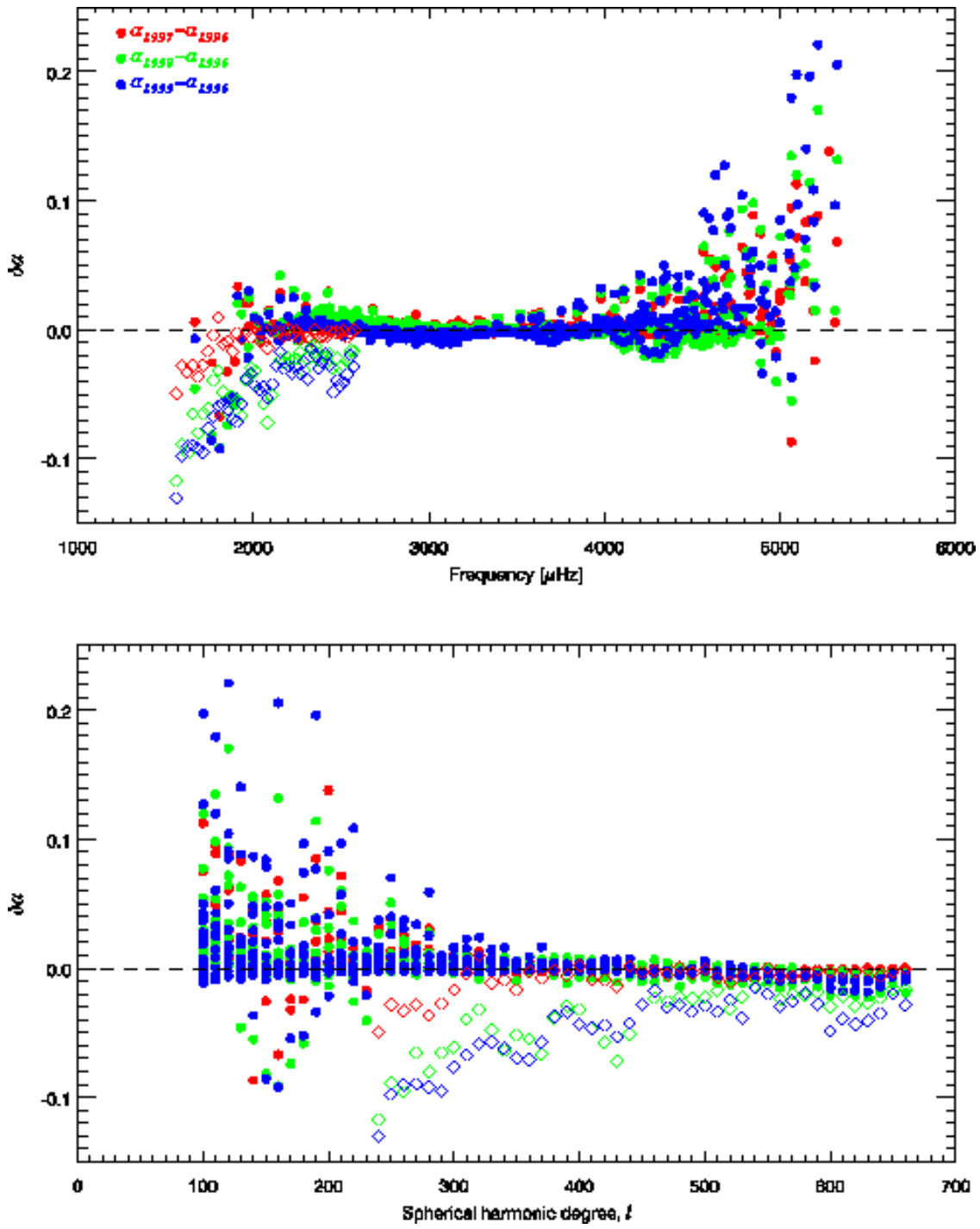

Fig. 35.— Changes of the asymmetry parameter – with respect to 1996 – for different epochs, as a function of frequency and degree. Changes for the f-modes are indicated by diamonds.

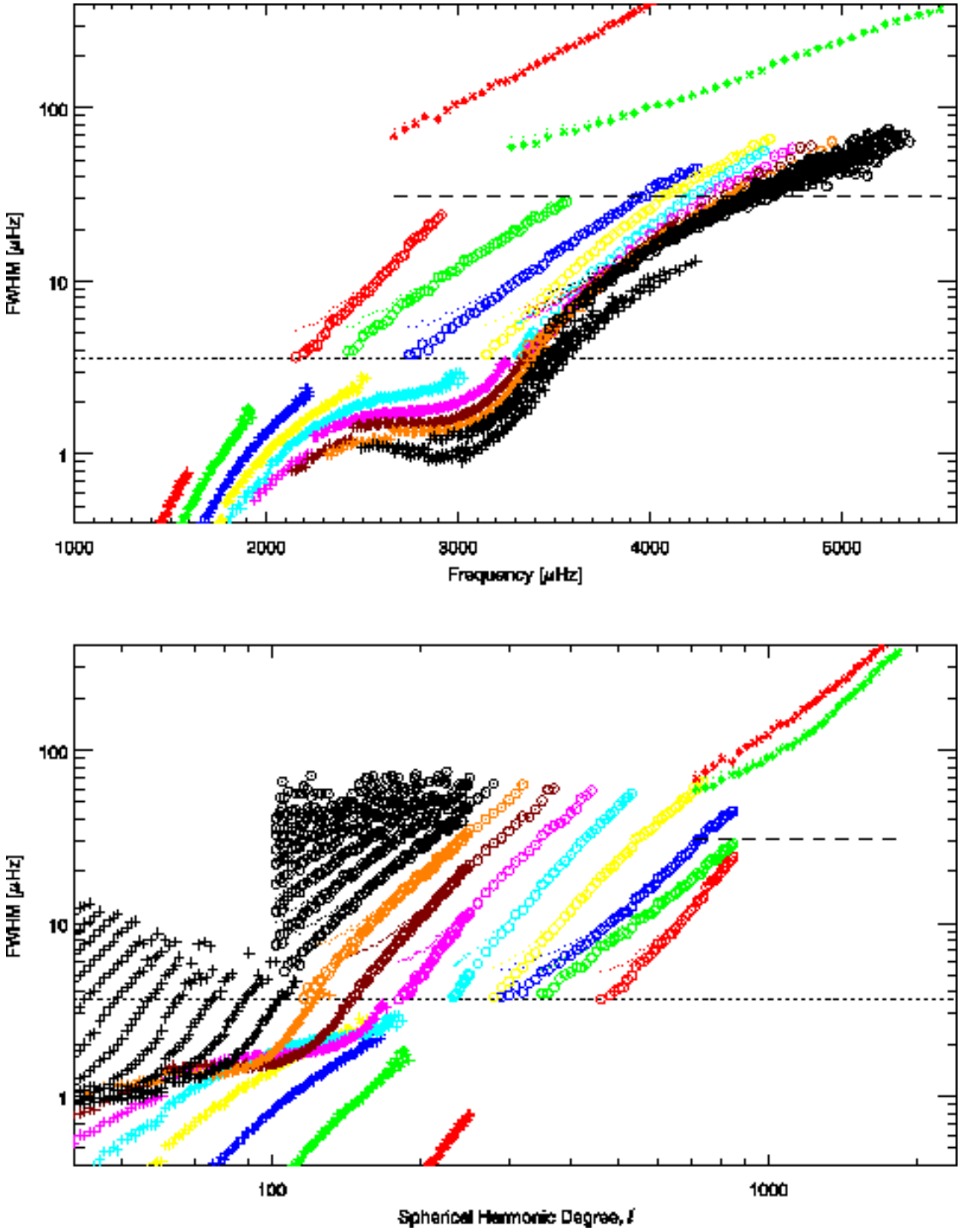

Fig. 36.— Corrected MDI linewidths (circles, this work) compared to MDI low and intermediate degree values derived from 360-day-long *Structure* data (crosses) and to very high degree corrected linewidth estimates from MDI in high-resolution mode (stars) as published by Duvall et al. (1998). Uncorrected linewidths are shown as dots. The horizontal lines correspond to the FWHM of the window functions for the MDI observations.

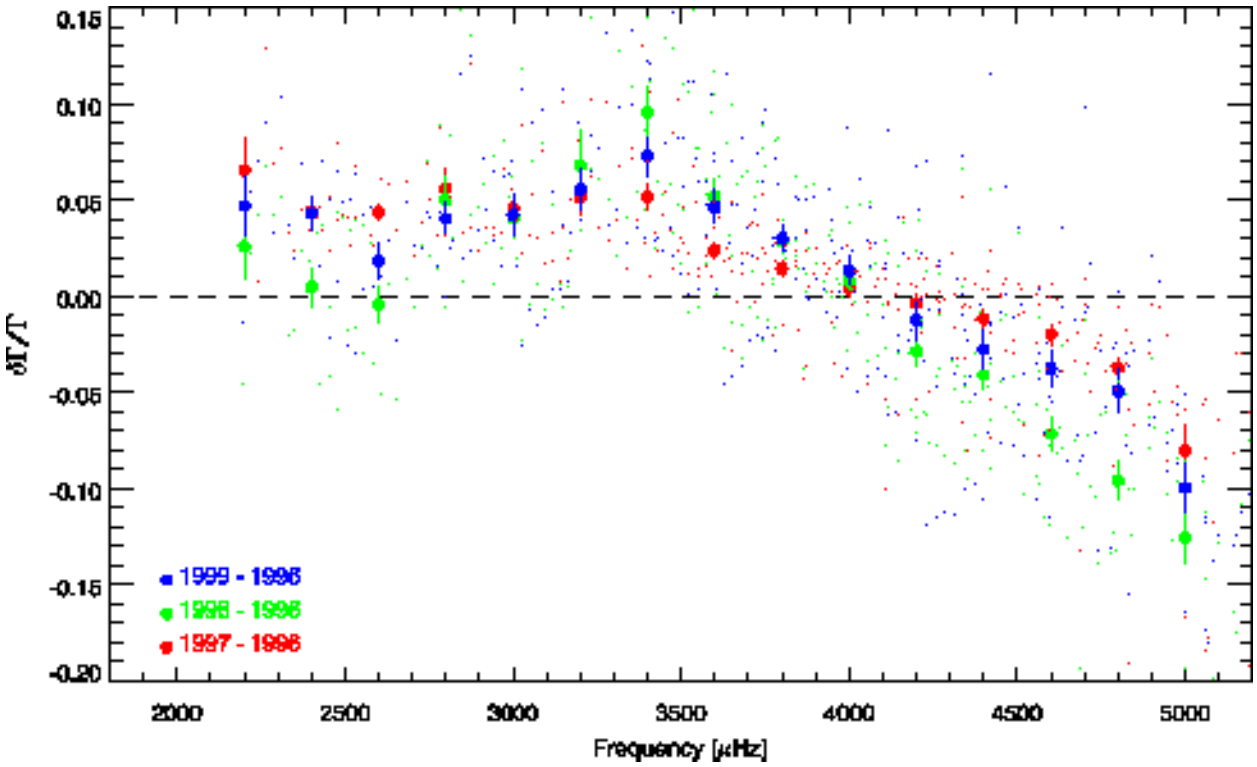

Fig. 37.— Raw and binned linewidth relative changes (dots and circles respectively), with respect to 1996, as a function of frequency, and restricted to modes common to all epochs. The ridge linewidths were first corrected according to Equation 29.

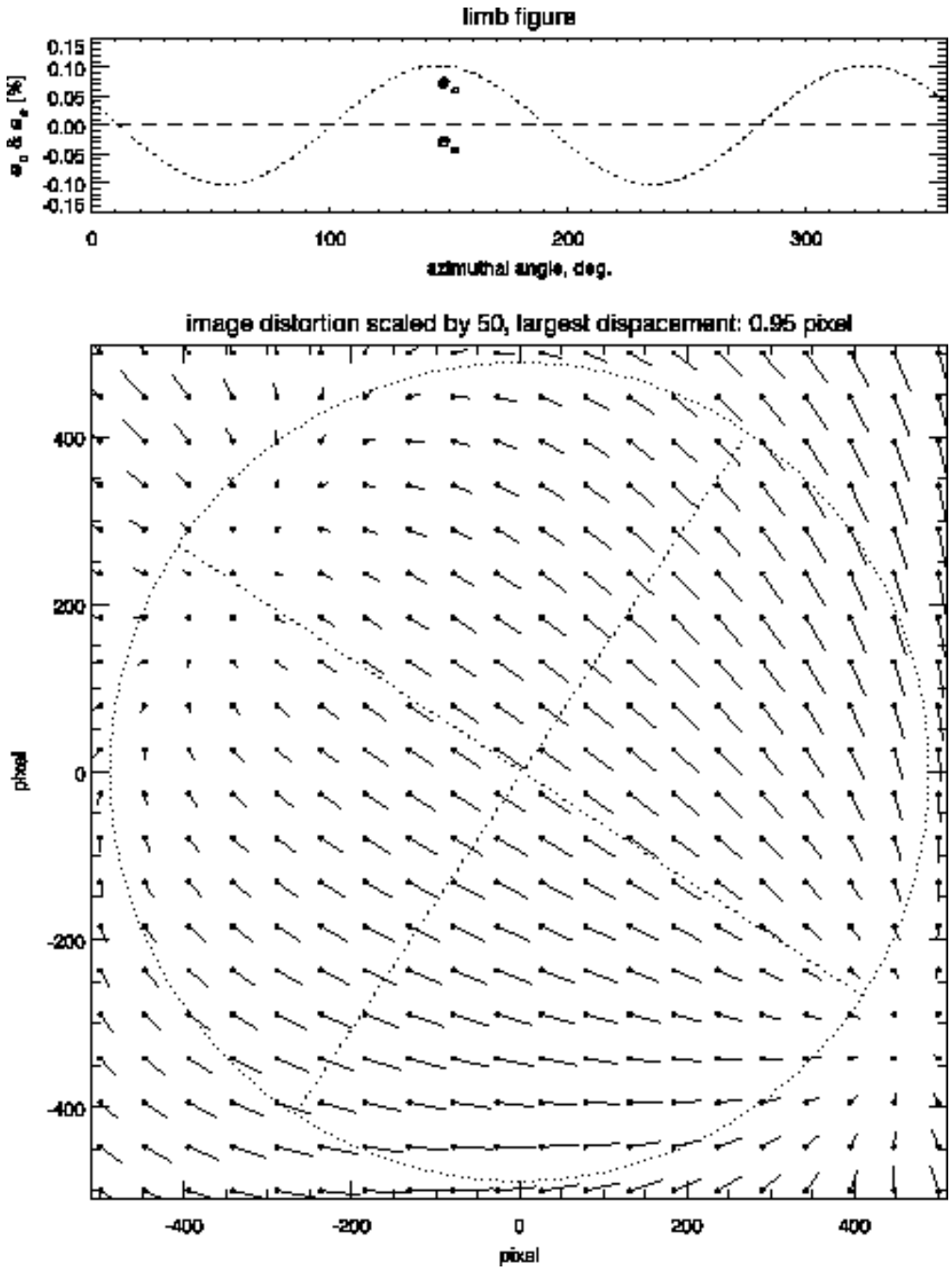

Fig. 38.— Map of the image distortion in the plane of the CCD. The distortion has been multiplied by a factor 50 to make it visible. The largest displacement inside the solar limb is 0.95 pixel. The top panel illustrates how the distorted departs from a circle (*i.e.*, $e_c = (x/r)^2 + (y/r)^2 - 1$) and how well it fits an ellipse (*i.e.*, $e_e = (x/a)^2 + (y/b)^2 - 1$).